

DISSERTATION

NANOMETER-THICK YTTRIUM IRON GARNET FILM DEVELOPMENT AND  
SPINTRONICS-RELATED STUDY

Submitted by

Houchen Chang

Department of Physics

In partial fulfillment of the requirements

For the Degree of Doctor of Philosophy

Colorado State University

Fort Collins, Colorado

Fall 2017

Doctoral Committee:

Advisor: Mingzhong Wu

Zbigniew Celinski

Stuart Field

Mario Marconi

Carl Patton

Copyright by Houchen Chang 2017

All Rights Reserved

## ABSTRACT

### NANOMETER-THICK YTTRIUM IRON GARNET FILM DEVELOPMENT AND SPINTRONICS-RELATED STUDY

In the last decade, there has been a considerable interest in using yttrium iron garnet ( $\text{Y}_3\text{Fe}_5\text{O}_{12}$ , YIG) materials for magnetic insulator-based spintronics studies. This interest derives from the fact that YIG materials have very low intrinsic damping. The development of YIG-based spintronics demands YIG films that have a thickness in the nanometer (nm) range and at the same time exhibit low damping similar to single-crystal YIG bulk materials.

This dissertation reports comprehensive experimental studies on nm-thick YIG films by magnetron sputtering techniques. Optimization of sputtering control parameters and post-deposition annealing processes are discussed in detail. The feasibility of low-damping YIG nm-thick film growth via sputtering is demonstrated. A 22.3-nm-thick YIG film, for example, shows a Gilbert damping constant of less than  $1.0 \times 10^{-4}$ . The demonstration is of great technological significance because sputtering is a thin film growth technique most widely used in industry.

The spin Seebeck effect (SSE) refers to the generation of spin voltage in a ferromagnet (FM) due to a temperature gradient. The spin voltage can produce a pure spin current into a normal metal (NM) that is in contact with the FM. Various theoretical models have been proposed to interpret the SSE, although a complete understanding of the effect has not been realized yet. In this dissertation the study of the role of damping on the SSE in YIG thin films is conducted for the first time. With the thin film development method mentioned in the last paragraph, a series of

YIG thin films showing very similar structural and static magnetic properties but rather different Gilbert damping values were prepared. A Pt capping layer was grown on each YIG film to probe the strength of the SSE. The experimental data show that the YIG films with a smaller intrinsic Gilbert damping shows a stronger SSE.

The majority of the previous studies on YIG spintronics utilized YIG films that were grown on single-crystal  $\text{Gd}_3\text{Ga}_5\text{O}_{12}$  (GGG) substrates first and then capped with either a thin NM layer or a thin topological insulator (TI) layer. The use of the GGG substrates is crucial in terms of realizing high-quality YIG films, because GGG not only has a crystalline structure almost perfectly matching that of YIG but is also extremely stable at high temperature in oxygen that is the condition needed for YIG crystallization. The feasibility of growing high-quality YIG thin films on Pt thin films is explored in this dissertation. This work is of great significance because it enables the fabrication of sandwich-like NM/YIG/NM or NM/YIG/TI structures. Such tri-layered structures will facilitate various interesting fundamental studies as well as device developments. The demonstration of a magnon-mediated electric current drag phenomenon is presented as an example for such tri-layered structures.

## ACKNOWLEDGEMENTS

I would like to thank my advisor Professor Mingzhong Wu for detailed advices, encouragement, and guidance throughout my Ph.D. program. Professor Wu spent much time on detailed discussions with me on my research work. During the most difficult time when I worked on the sputtering growth of YIG films on metals, he gave me moral support, sufficient time, and confidence. This dissertation would not have been possible without his guidance and help.

I would like to thank Professor Boris Kalinikos for spending much time discussing on microwave and spin wave theories. I am very grateful to Professor Carl Patton for his sincere help and knowledge on microwave and magnetism. In addition, I want to thank Professor Richard Eykholt for providing me with invaluable insights in physics through the excellent thermodynamic course. My appreciation also extends to Robert Adame for his generous help at the machine shop. I wish to acknowledge the members of my dissertation committee for offering their time, support, guidance throughout my research and review of this document.

I want to express my gratitude to my colleagues: Dr. Tao Liu, who taught me a lot on research and conducting experiments, Dr. Yiyang Sun, who taught me much on thin film development and ferromagnetic resonance measurements, Dr. Lei Lu, who taught me AFM and VNA-FMR, Dr. Praveen Janantha, who taught me much knowledge on microwave and gave me sincere suggestions, Dr. Peng Li for generous help and discussions, as well as Mike Kabatek, David Ellsworth, William Schneider, and Daniel Richardson. I am also very grateful to Dr. Wei Li and Dr. Tao Song who encouraged me a lot. Lastly, I would owe my deepest thanks to my wife Yang Liu and my parents Zhongzhu Chang and Xiaoqiu Dong for their unconditional love and support. I would not have completed my Ph.D. program without their support.

## TABLE OF CONTENTS

ABSTRACT.....	ii
ACKNOWLEDGEMENTS.....	iv
CHAPTER 1 OVERVIEW .....	1
1.1 Background and motivations .....	1
1.2 Dissertation organization .....	4
CHAPTER 2 INTRODUCTION .....	6
2.1 Structure and magnetic properties of YIG .....	6
2.2 Magnetron sputtering techniques.....	9
2.2.1 Plasma ignition and sputtering process.....	10
2.2.2 Deposition process, film formation, and ion etching process.....	17
2.3 Measurement techniques.....	22
2.3.1 X-ray diffraction .....	22
2.3.2 Atomic force microscopy.....	23
2.3.3 Vibrating sample magnetometry .....	25
2.3.4 Ferromagnetic resonance measurements .....	26
CHAPTER 3 INTRODUCTION TO SPIN WAVE THEORY AND RELAXATION.....	28
3.1 Equations of motion and boundary conditions for magnetic moments in materials .....	28
3.2 Dispersion relations for dipole-exchange spin waves.....	36
3.3 Ferromagnetic resonance uniform modes .....	42
3.4 Damping caused linewidth broadening in FMR measurements .....	45
3.5 Summary .....	50

CHAPTER 4 DEVELOPING YIG NANO FILMS BY SPUTTERING TECHNIQUES .....	51
4.1 Optimization of fabrication parameters for uniform YIG nano films.....	52
4.2 Dependence of YIG film properties on sputtering processes .....	60
4.3 High-quality YIG nano films developed by sputtering techniques.....	65
4.4 Summary .....	69
CHAPTER 5 ROLE OF DAMPING IN SPIN SEEBECK EFFECT IN YTTRIUM IRON GARENT THIN FILIMS .....	70
5.1 Introduction – the spin Seebeck effect and theoretical models.....	70
5.2 Properties of the YIG and YIG/Pt samples .....	73
5.2.1 Crystalline and structural properties .....	75
5.2.2 Magnetic properties .....	78
5.3 Spin Seebeck measurements .....	86
5.4 Role of damping on the SSE.....	89
5.5 Summary .....	92
CHAPTER 6 SPUTTERING GROWTH OF $Y_3Fe_5O_{12}$ ON PLATINUM LAYERS AND SPIN TRANSFER AT $Y_3Fe_5O_{12}/Pt$ INTERFACES .....	93
6.1 Motivation.....	93
6.2 Samples fabrication and characterization .....	95
6.2.1 High-quality YIG/Pt/GGG thin film samples by optimized development process	95
6.2.2 Discussion of the two-step Pt deposition and two-step annealing processes.....	103
6.3 Spin pumping at YIG/Pt interfaces .....	105
6.4 Magnon-mediated current drag.....	109
6.5 Summary .....	114

CHAPTER 7 SUMMARY AND OUTLOOK .....	115
APPENDIX.....	116
A. Derivation of Paschen's law.....	116
B. Derivation of one-dimensional model for atom deposition and dissociation.....	120
C. One dimensional collision model programs for data analysis and graph depiction.....	127
D. Derivation of the Green's function tensor of the dipole field .....	142
E. The mathematical form of the internal field.....	144
F. Linearized precession equation.....	145
G. Solutions for the Sturm-Liouville problem.....	147
H. The amplitude of the eigenfunctions.....	148
I. Tensor of Green's functions for dipole fields in xy plane .....	149
J. Simplification of the equation for spinwave amplitude .....	150
K. Explicit analytical form of operators P and Q.....	153

# CHAPTER 1

## OVERVIEW

### 1.1 Background and motivations

There has been a considerable interest in using yttrium iron garnet ( $\text{Y}_3\text{Fe}_5\text{O}_{12}$ , YIG) materials for spintronics in the last decade.<sup>1,2,3,4,5,6,7,8</sup> This interest derives from the fact that YIG materials have very low intrinsic damping<sup>9</sup> and is an electric insulator. The development of YIG-based spintronics demands YIG films that have a thickness in the nanometer (nm) range and at the same time exhibit low damping similar with single-crystal YIG bulk materials. Previous work demonstrated pulsed laser deposition (PLD) of YIG thin films with relatively low damping. 20-nm-thick PLD films, for example, showed a Gilbert damping constant of  $\alpha = 0.00023$ .<sup>10</sup> However, obstacles of the PLD techniques applied to industry stand, like small wafer deposition, low repeatability, and instability of the system control. Magnetron sputtering, on the

---

<sup>1</sup> Y. Kajiwara, K. Harii, S. Takahashi, J. Ohe, K. Uchida, M. Mizuguchi, H. Umezawa, H. Kawai, K. Ando, K. Takanashi, S. Maekawa, and E. Saitoh, *Nature* **464**, 262 (2010).

<sup>2</sup> K. Uchida, J. Xiao, H. Adachi, J. Ohe, S. Takahashi, J. Ieda, T. Ota, Y. Kajiwara, H. Umezawa, H. Kawai, G. E. W. Bauer, S. Maekawa, and E. Saitoh, *Nat. Mater.* **9**, 894 (2010).

<sup>3</sup> J. Xiao, G. E. W. Bauer, K. Uchida, E. Saitoh, and S. Maekawa, *Phys. Rev. B* **81**, 214418 (2010).

<sup>4</sup> C. W. Sandweg, Y. Kajiwara, A. V. Chumak, A. A. Serga, V. I. Vasyuchka, M. B. Jungfleisch, E. Saitoh, and B. Hillebrands, *Phys. Rev. Lett.* **106**, 216601 (2011).

<sup>5</sup> B. Heinrich, C. Burrowes, E. Montoya, B. Kardasz, E. Girt, Y. -Y. Song, Y. Sun, and M. Wu, *Phys. Rev. Lett.* **107**, 066604 (2011).

<sup>6</sup> H. Kurebayashi, O. Dzyapko, V. E. Demidov, D. Fang, A. J. Ferguson, and S. O. Demokritov, *Nat. Mater.* **10**, 660 (2011).

<sup>7</sup> S. Y. Huang, X. Fan, D. Qu, Y. P. Chen, W. G. Wang, J. Wu, T. Y. Chen, J. Q. Xiao, and C. L. Chien, *Phys. Rev. Lett.* **109**, 107204 (2012).

<sup>8</sup> H. Nakayama, M. Althammer, Y. -T. Chen, K. Uchida, Y. Kajiwara, D. Kikuchi, T. Ohtani, S. Geprags, M. Opel, S. Takahashi, R. Gross, G. E. W. Bauer, S. T. B. Goennenwein, and E. Saitoh, *Phys. Rev. Lett.* **110**, 206601 (2013).

<sup>9</sup> Y. Sun and M. Wu, *Solid State Physics* **64**, 157 (2013).

<sup>10</sup> Y. Sun, Y. -Y. Song, H. Chang, M. Kabatek, M. Jantz, W. Schneider, M. Wu, H. Schultheiss, and A. Hoffmann, *Appl. Phys. Lett.* **101**, 152405 (2012).

other hand, is a thin film fabrication physical vapor deposition (PVD) technique most widely used in industry that allows for the production of large-size wafers with uniform properties. Other advantages of sputtering include convenient control, high repeatability, and fast production. In this dissertation, the demonstration of using magnetron sputtering to grow high-quality polycrystalline YIG nm-thick films on gadolinium gallium garnet ( $\text{Gd}_3\text{Ga}_5\text{O}_{12}$ , GGG) substrates is discussed in details, which is of great technological significance for industrialization as well as scientific research.<sup>11</sup> The damping constant of the YIG films is comparable or even smaller than that of the PLD films.<sup>12</sup> Such demonstration of high-quality nm-thick YIG films has made possible the nanoscale patterning of YIG films<sup>13</sup> and the future development of YIG-based nanoscale devices.

The spin Seebeck effect (SSE) refers to the generation of a spin voltage in a ferromagnet (FM) due to a temperature gradient. This spin voltage can produce a pure spin current in an adjacent normal metal (NM) that is in contact with the FM. The SSE was first discovered in ferromagnetic metals<sup>14,15,16</sup> and then was also observed in magnetic insulators<sup>2,17,18,19,20,21</sup> and

---

<sup>11</sup> T. Liu, H. Chang, V. Vlamincck, Y. Sun, M. Kabatek, A. Hoffmann, L. Deng, and M. Wu, *J. Appl. Phys.* **115**, 17A501 (2014).

<sup>12</sup> H. Chang, P. Li, W. Zhang, T. Liu, A. Hoffmann, L. Deng, and M. Wu, *IEEE Magn. Lett.* **5**, 6700104 (2014).

<sup>13</sup> N. Zhu, H. Chang, A. Franson, T. Liu, X. Zhang, E. J. Halperin, M. Wu, and H. Tang, *Appl. Phys. Lett.* **110**, 252401 (2017).

<sup>14</sup> K. Uchida, S. Takahashi, K. Harii, J. Ieda, W. Koshibae, K. Ando, S. Maekawa, and E. Saitoh, *Nature* **455**, 778 (2008).

<sup>15</sup> K. Uchida, T. Ota, K. Harii, S. Takahashi, S. Maekawa, Y. Fujikawa, and E. Saitoh, *Solid State Commun.* **150**, 524–528 (2010).

<sup>16</sup> K. Uchida, H. Adachi, T. An, T. Ota, M. Toda, B. Hillebrands, S. Maekawa, and E. Saitoh, *Nat. Mater.* **10**, 737–741 (2011).

<sup>17</sup> H. Adachi, K. Uchida, E. Saitoh, J. Ohe, S. Takahashi, and S. Maekawa, *Appl. Phys. Lett.* **97**, 252506 (2010).

<sup>18</sup> K. Uchida, T. Nonaka, T. Ota, and E. Saitoh, *Appl. Phys. Lett.* **97**, 262504 (2011).

<sup>19</sup> E. Padrón-Hernández, A. Azevedo, and S. M. Rezende, *Phys. Rev. Lett.* **107**, 197203 (2011).

<sup>20</sup> M. B. Jungfleisch, T. An, K. Ando, Y. Kajiwara, K. Uchida, V. I. Vasyuchka, A. V. Chumak, A. A. Serga, E. Saitoh, and B. Hillebrands, *Appl. Phys. Lett.* **102**, 062417 (2013).

<sup>21</sup> D. Qu, S. Y. Huang, J. Hu, R. Wu, and C. L. Chien, *Phys. Rev. Lett.* **110**, 067206 (2013).

semiconductors.<sup>22,23</sup> Although a complete understanding of the SSE effect has not been realized yet, various theoretical models have been proposed to interpret the effect<sup>2,3,16,17,23,24,25,26,27</sup>, among which the magnetic damping is engaged as a critical ingredient of the SSE, though in very different ways. In spite of these theoretical aspects, however, there has been no experiment on the effects of the damping on the SSE so far, to the best of our knowledge. With the use of the magnetron sputtering techniques with a systematic, repeatable fabrication method, YIG samples with different damping constants and identical other magnetic properties could be achieved, making such SSE experiments feasible.

For certain monolithic devices (like coupled-line and stripline-type devices) as well as potential applications in spintronic devices, one needs to grow FM films on metals. Generally speaking, it is technically challenging to grow high-quality YIG films on metallic films, and possible issues include the oxidation and peeling-off of the metallic layer, interfacial diffusion, and formation of pin-holes in the films during the growth or post-annealing process. Previous work<sup>28</sup> has demonstrated the feasibility of thick YIG film fabrication with PLD techniques on metallic layers. Realization of growing YIG films on metals by magnetron sputtering technique with a more convenient method, as illustrated in this dissertation, will provide significant implications for the future development of YIG-based spintronic devices in industry. As an

---

<sup>22</sup> C. M. Jaworski, J. Yang, S. Mack, D. D. Awschalom, J. P. Heremans, and R. C. Myers, *Nat. Mater.* **9**, 898 (2010).

<sup>23</sup> C. M. Jaworski, J. Yang, S. Mack, D. D. Awschalom, R. C. Myers, and J. P. Heremans, *Phys. Rev. Lett.* **106**, 186601 (2011).

<sup>24</sup> S. Hoffman, K. Sato, and Y. Tserkovnyak, *Phys. Rev. B* **88**, 064408 (2013).

<sup>25</sup> S. M. Rezende, R. L. Rodríguez-Suárez, R. O. Cunha, A. R. Rodrigues, F. L. A. Machado, G. A. Fonseca Guerra, J. C. Lopez Ortiz, and A. Azevedo, *Phys. Rev. B* **89**, 014416 (2014).

<sup>26</sup> U. Ritzmann, D. Hinzke, and U. Nowak, *Phys. Rev. B* **89**, 024409 (2014).

<sup>27</sup> A. Kehlberger, U. Ritzmann, D. Hinzke, E.-J. Guo, J. Cramer, G. Jakob, M. C. Onbasli, D. Kim, C. A. Ross, M. B. Jungfleisch, B. Hillebrands, U. Nowak, and M. Kläui, *Phys. Rev. Lett.* **115**, 096602 (2015).

<sup>28</sup> Yttrium iron garnet nano films: Epitaxial growth, damping, spin pumping, and magnetic proximity effect by Sun, Yiyang, Ph. D., Colorado State University, 2014, 82 pages; AAT 3624377

example of facilitating interesting fundamental studies in spintronics, the demonstration of a magnon-mediated electric current drag phenomenon is discussed.

## **1.2 Dissertation organization**

This dissertation presents comprehensive studies on YIG thin film development by the magnetron sputtering techniques, including control parameter optimization, thin film characterization, and development of YIG films on metallic layers. Demonstration of spintronics-related experiments and research on some fundamental topics in spintronics, like the spin Seebeck effect and the magnon-mediated electric current drag phenomenon are also discussed.

Chapter 2 introduces the basic structural and magnetic properties of YIG materials as well as the basics of magnetron sputtering techniques, including the mechanisms of plasma generation, sputtering process, thin film formation, and argon ion etching process. Some measurement techniques that are frequently mentioned in the following chapters are also discussed briefly.

Chapter 3 presents conceptual and qualitative discussions of dispersion relations for ferromagnetic resonance (FMR) modes and spin wave modes in magnetic thin films. Only the uniform resonance mode will be touched in the following chapters. The damping mechanism and the linewidth broadening for the uniform resonance mode under the Gilbert model are discussed.

Chapter 4 presents the growth and magnetic properties of low-damping nm-thick polycrystalline YIG films by magnetron sputtering techniques. Details on the optimization process, the dependence of YIG film properties on critical control parameters, and the characterization and magnetic properties of YIG thin films are discussed in details.

Chapter 5 reports on the role of damping in the SSE in the Pt/YIG/GGG system. This is a continuous study following that presented in Chapter 4. A series of thin film samples with

identical magnetic properties but different damping values are made based on the thin film development study in Chapter 4. The study on the SSE in the Pt/YIG/GGG system indicates a stronger SSE strength for a lower damping value.

Chapter 6 presents the study of developing YIG thin films on metallic thin films. A unique thin film development method is created for successful fabrication of YIG thin films on Pt metallic layers. Spin pumping experiments show efficient spin transfer at the YIG/Pt interface. The magnon-mediated electric current drag phenomenon is studied as a demonstration of its application on fundamental studies in spintronics.

# CHAPTER 2

## INTRODUCTION

### 2.1 Structure and magnetic properties of YIG

Yttrium iron garnet ( $\text{Y}_3\text{Fe}_5\text{O}_{12}$ , YIG) was first discovered by Bertaut and Forrat in 1956.<sup>29</sup> YIG is a synthesized ferrimagnetic oxide insulator with nearly cubic symmetry. One cubic unit cell has a lattice constant of 12.376 Å and consists of eight chemical formula units, with 24  $\text{Y}^{3+}$  cations, 40  $\text{Fe}^{3+}$  cations, and 96  $\text{O}^{2-}$  anions.<sup>30,31</sup> Figure 2.1 shows schematic diagrams for the iron and yttrium cations surrounded by oxygen anions in YIG materials. Each  $\text{Y}^{3+}$  ion is located on a c-site, surrounded by eight nearest oxygen anions which form a dodecahedron. Among the 40  $\text{Fe}^{3+}$  cations, 40% are located on a-sites and 60% are located on d-sites. Six oxygen anions surround one a-site cation, forming an octahedron, while four anions are around one d-site cation and form a tetrahedron. Gadolinium gallium garnet ( $\text{Gd}_3\text{Ga}_5\text{O}_{12}$ , GGG) substrates are usually used for YIG thin film fabrication. The GGG single crystal has the identical crystal structure as that of the YIG crystal. The difference between the YIG and GGG lattice constants is as small as 0.0001 Å.

---

<sup>29</sup> F. Bertaut and F. Forrat, *Compt. Rend.* **242**, 382 (1956).

<sup>30</sup> M. A. Gilileo and S Geller, *Phys. Rev.* **110**, 73 (1958).

<sup>31</sup> G. Winkler, *Magnetic Garnets* (Friedr. Vieweg & Sohn Verlagsgesellschaft GmbH: Braunschweig, 1981).

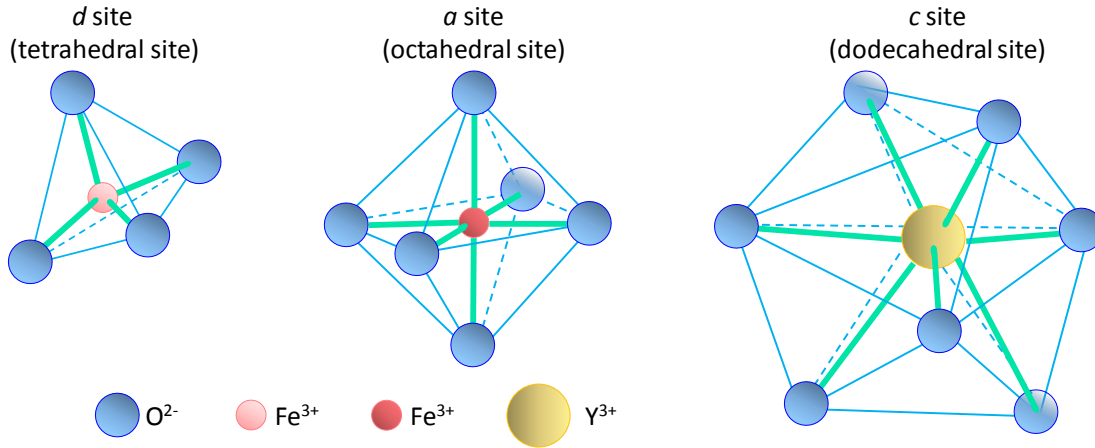


Figure 2.1. Schematic diagrams of three different sites occupied by cations in yttrium iron garnet.

Figure 2.2 shows the cation arrangement in one octant of an YIG unit cell. The magnetization in the YIG originates from super-exchange interaction<sup>32,33</sup> between a-site and d-site  $\text{Fe}^{3+}$  cations. The  $\text{Y}^{3+}$  cations have no magnetic moment. Based on Anderson's theory<sup>33</sup>, in magnetic ion – oxygen ion – magnetic ion bonds, the interaction is strongest with a bond angle near  $180^\circ$  and weakest for  $90^\circ$ . In the YIG crystal structure, the largest bond angle of  $126.6^\circ$ <sup>34</sup> occurs at "a-site  $\text{Fe}^{3+}$ " -  $\text{O}^{2-}$  - "d-site  $\text{Fe}^{3+}$ " and such interaction leads to anti-parallel magnetic moments between the a-site and d-site  $\text{Fe}^{3+}$  ions. Each  $\text{Fe}^{3+}$  ion contributes 5 Bohr magnetons ( $\mu_B$ ) and each unit cell in YIG material has a net magnetic moment of  $40 \mu_B$  (Bohr magneton). This corresponds to a theoretical saturation induction ( $4\pi M_S$ ) of 2470 G at 0 K, which is very close to the value (2463 G) measured for YIG thin films at 4.2 K.<sup>35</sup> The  $4\pi M_S$  value at room temperature is about 1750 G and may vary from 1450 to 2100 G, depending on fabrication methods and defects in the films.

<sup>32</sup> H. A. Kramers, *Physica* **1**, 182 (1934).

<sup>33</sup> P. W. Anderson, *Phys. Rev.* **79**, 350 (1950).

<sup>34</sup> B. Lax and K. J. Button, *Microwave Ferrites and Ferrimagnetics* (McGraw-Hill, New York, 1962).

<sup>35</sup> H. A. Algra and P. Hansen, *Appl. Phys. A* **29**, 83 (1982).

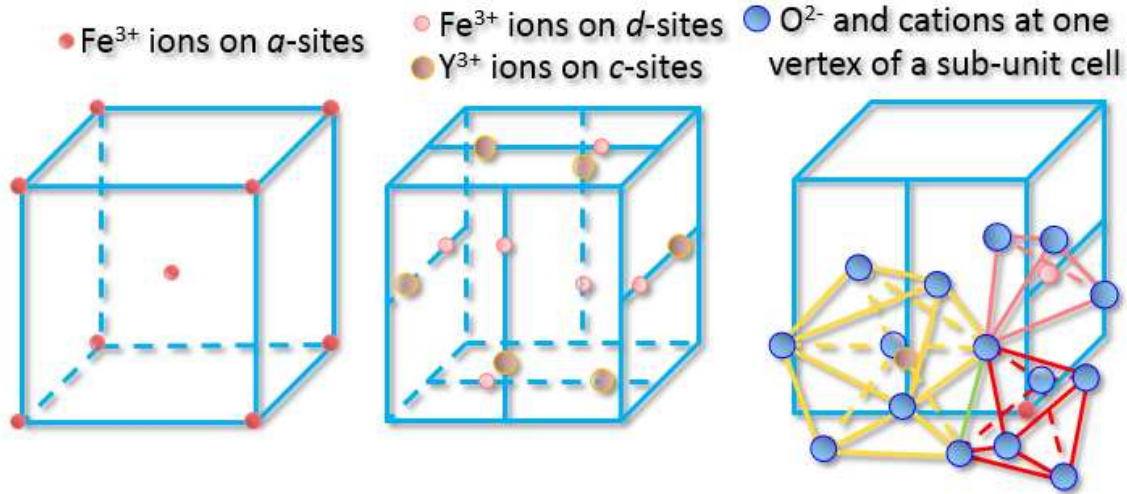


Figure 2.2. Cation arrangement in one octant of a YIG unit cell. A-site ions form a body-centered cubic (bcc) sub-unit cell. D-site and c-site cations are distributed symmetrically along the center lines of the cubic faces.

The single-crystal yttrium iron garnet has a weak cubic magneto-crystalline anisotropy with the easy axis along (111) direction. The first- and second-order cubic anisotropy constants are  $-6100 \text{ erg/cm}^3$  and  $-260 \text{ erg/cm}^3$ , respectively, at room temperature,<sup>36</sup> corresponding to the effective magnetic anisotropy fields of  $-87.6 \text{ Oe}$  and  $-3.7 \text{ Oe}$ , respectively, for a saturation induction of  $1750 \text{ Oe}$ . The negative sign indicates easy-plane anisotropy.

The ferromagnetic resonance (FMR) linewidth originated from intrinsic damping in near perfect YIG single crystals is about  $0.2 \text{ Oe}$  at  $10 \text{ GHz}$ ,<sup>37,38</sup> which corresponds to an intrinsic Gilbert damping constant  $\alpha$  of about  $3 \times 10^{-5}$  assuming zero inhomogeneous linewidth broadening. This value is about one order of magnitude smaller than that in barium hexagonal ferrites<sup>39</sup> and two orders of magnitude smaller than that in ferromagnetic metals. The extremely small intrinsic magnetic damping makes YIG a material of choice for studies of spin waves as well as magnetic

<sup>36</sup> D. Stancil and A. Prahakar, *Spin Waves – Theory and Applications* (Springer, New York, 2009).

<sup>37</sup> M. Sparks, *Ferromagnetic-Relaxation Theory* (McGraw Hill, New York, 1964).

<sup>38</sup> A. G. Gurevich and G. A. Melkov, *Magnetization Oscillations* (CRC Press, Boca Raton, 2000).

<sup>39</sup> Y. Y. Song, S. Kalarickal, and C. E. Patton, *J. Appl. Phys.* 94, 5103 (2003).

insulator-based spintronics applications. More structural and physical properties of single-crystal YIG are provided in Table 2.1. All values listed are for room temperature unless specified.

Table 2.1. Properties of yttrium iron garnet

Parameter	Value	Reference
Lattice constant $a$ (273 K)	$12.376 \pm 0.004 \text{ \AA}$	31, 34
Lattice constant $a$ (77 K)	$12.361 \text{ \AA}$	31
Lattice constant $a$ (4 K)	$12.359 \text{ \AA}$	31
Thermal expansion coefficient (298 K)	$8.3 \times 10^{-6}$	31
Thermal expansion coefficient (623 K)	$11.0 \times 10^{-6}$	31
Density	$5.17 \text{ g/cm}^3$	36
Band gap	2.85 eV	36
Saturation induction $4\pi M_s$	1750 G	34
Saturation induction $4\pi M_s$ (4.2 K)	2463 G	35
Cubic anisotropy constant $K_1$	$-6100 \text{ erg/cm}^3$	36
Cubic anisotropy constant $K_2$	$-260 \text{ erg/cm}^3$	36
Curie temperature $T_c$	559 K	36
Exchange constant $\alpha$	$3 \times 10^{-12} \text{ cm}^2$	36
Intrinsic damping constant $\alpha$	$3 \times 10^{-5}$	37
Faraday rotation (1.2 $\mu\text{m}$ )	240 deg/cm	36
Dielectric constant (10 GHz)	14.7	40
Dielectric loss tangent (10 GHz)	0.0002	40

## 2.2 Magnetron sputtering techniques

Magnetron sputtering is a widely used physical vapor deposition (PVD) technique. Its creation traces back to 1930s when F. M. Penning described the trapping of electrons in certain

<sup>40</sup> H. How, P. Shi, C. Vittoria, L. C. Kempel, and K. D. Trott, J. Appl. Phys. **87**, 4966 (2000).

electric and magnetic field configurations,<sup>41,42,43</sup> a concept that leads to the further development of the modern magnetron sputtering configurations in the 1970s.<sup>44,45,46</sup> This technique has been widely implemented in thin film fabrication industries including semiconductors, optics, magnetic storage, and many others because it allows for fast production, pre-surface sputter cleaning, easy control, and uniformity over a large size, among others.

## 2.2.1 Plasma ignition and sputtering process

In magnetron sputtering, plasma needs to be ignited and created before sputtering target materials to substrates. A plasma is a dilute ionized gas containing free electrons and positive ions. In a vacuum chamber, argon gas is typically filled in with low pressure, typically several mTorr. Then a voltage between the cathode (targets) and the anode (shutters or substrate holders) is applied (2-5 kV). If the voltage is larger than the breakdown voltage, ionization of argon atoms occurs, making the gas electrically conductive and forming a plasma. This process is called glow discharge as the plasma will glow with colors. The actual color depends on the type of the gas in the chamber.

The breakdown voltage is critical for the plasma ignition. It can be described by Paschen's law, as shown by Eq. 2.1, which was initially proposed by Friedrich Paschen when he studied gas glow under low pressure in a glass tube in 1889.<sup>47</sup> A brief derivation of the Paschen's law is in Appendix A for interested readers.

---

<sup>41</sup> F. M. Penning, *Physica* **8**, 137 (1928).

<sup>42</sup> F. M. Penning, *Proc. Roy. Soc. Amst.* **31**, 14 (1928).

<sup>43</sup> F. M. Penning, *Proc. Roy. Soc. Amst.* **33**, 841 (1930).

<sup>44</sup> I. I. Aksenov, V. A. Belous, V. G. Padalka, and V. M. Khoroshikh, *Phys. Chem. Mater. Process.* **6**, 89 (1977).

<sup>45</sup> M. S. P. Lucas, J. H. A. Owen, W. C. Stewart, and C. R. Vail, *Rev. Sci. Instrum.* **32**, 203 (1961).

<sup>46</sup> A. A. Snaper, "Arc deposition process and apparatus", US 3,625,848 (1971).

<sup>47</sup> F. Paschen, *Annalen der Physik.* **273**, 69 (1889).

$$V_{BD} = \frac{Bpd}{\ln(Apd) - \ln(\ln(1 + 1/\gamma))} \quad (2.1)$$

Equation 2.1 describes the breakdown voltage  $V_{BD}$ . In the equation,  $p$  is the pressure of the neutral gas,  $d$  is the gap distance between the cathode (the target) and the anode (the substrate),  $\gamma$  is the secondary electron emission coefficient at the cathode,  $A$  is the saturation ionization in the gas at a particular electric field/pressure ratio, and  $B$  is related to the excitation and ionization energies. Table 2.2 shows the minimum breakdown voltage and the corresponding  $pd$  products for some gases. Some Paschen's curves for gases are shown in Fig. 2.3.

Table 2.2 Minimum breakdown voltages and the corresponding  $pd$  products for some gases<sup>48</sup>

Gas	$(V_{BD})_{\min}$ (V)	$pd_{\min}$ (Torr · cm)
Air	327	0.567
Ar	137	0.9
CO <sub>2</sub>	420	0.51
H <sub>2</sub>	273	1.15
N <sub>2</sub>	251	0.67
He	156	4.0

There is a minimal point in each Paschen's curve in Fig. 2.3. The physical explanation is as follows. For a bigger  $pd$  product, electrons will collide frequently and cannot acquire sufficient energy to ionize neutral particles. Thus, a bigger electric potential should be applied for plasma ignition. While for a smaller  $pd$  product, more electrons will collide with the anode before colliding and ionizing the gas, also leading to a bigger breakdown voltage.

<sup>48</sup> M. S. Naidu and V. Kamaraju, High Voltage Engineering 2nd (McGraw Hill, 1995).

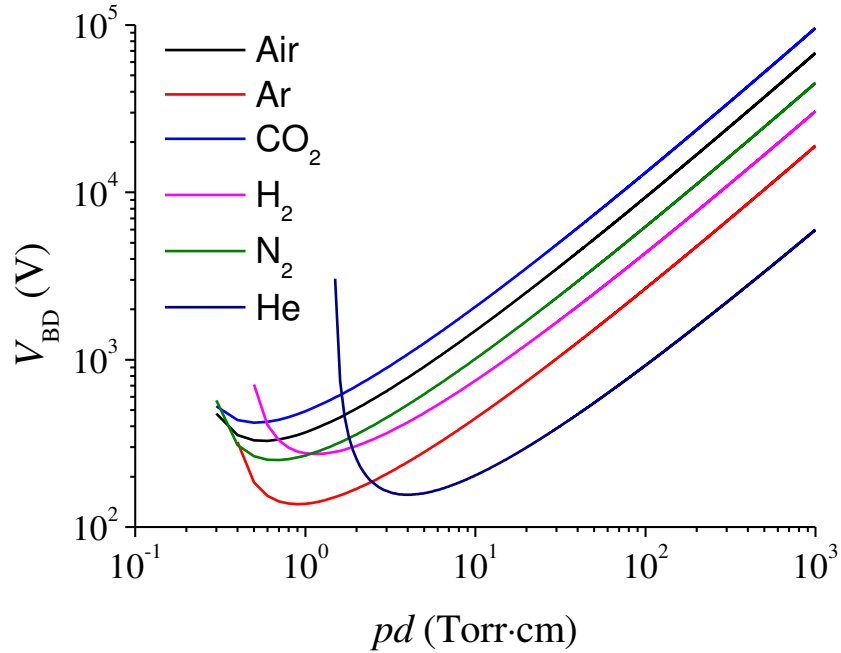


Figure 2.3. Paschen's curves for some gases

For the system used in the laboratory with a general setup, the distance  $d$  between the cathode and the anode is  $\sim 10$  cm. And the argon gas pressure is from 3 to 20 mTorr. Based on this, the breakdown voltage lands on the monotonically decreasing range in Fig. 2.3. In this range one needs to increase the distance  $d$  and/or the gas pressure to get a lower breakdown voltage for an easy plasma ignition. Experimentally, it is convenient to use a higher gas pressure than that used in a fabrication recipe for the ignition. When the plasma is ignited and stabilized, the pressure is reduced gradually to the designated value for thin film deposition. One physical reason that argon gas is widely used for sputtering is the relatively low breakdown voltage compared with other gases, as shown in Table 2.2 and Fig. 2.3. This makes the ionization process easier. Other reasons include inertness, safety in transportation, and cost.

As the plasma is created and sustained by frequent collisions between electrons and argon atoms, argon ions with positive charges will move to and collide with the target (cathode) surface and the free electrons will fly to the substrates (anode) due to the electric field. From

material fabrication perspective, there are two shortcomings in this process. First, large amount of free electrons impinge the surface of the substrate (and the film) with high energy acquired from the acceleration in the electric field, which will damage and heat the substrate. This is not desired for either smooth interfaces or sustainable growth. Second, the plasma needs to be maintained with high pressure, as electrons and argon particles keep moving away so that the collision rate is thus decreased.



Figure 2.4. Top view of a modern magnetron sputtering gun. The bar magnets surrounded have identical S poles pointing up and the center magnet has an opposite pole direction. Sometimes the center magnet is replaced with a Cu rod for non-magnetic materials, as shown in the figure.

These problems can be solved with a smart design of trapping electrons in a magnetic field. Figure 2.4 shows the top view of a modern magnetron gun. The center magnet has an opposite pole with the surrounding magnets. Sometimes a Cu center bar is used instead of a magnetic bar for non-magnetic materials. The target was mounted on top of the surface and the electric field (DC or RF) is applied vertically to the gun surface. The motion of electrons can be described as follows. For convenience of description without loss of generality, the area near the top surface of the target can be decomposed into two regions: the cathode dark space (CDS) region right on top of the target surface and the negative glow region (NG) as shown in Fig. 2.5. Approximately,

a free electron moves mainly under the influence of the electric field in CDS region and the magnetic field in NG region. A free electron, first located on the surface of the target, will be accelerated by the electric field in the CDS region and move to the NG region with some kinetic energy. Then, via the Lorentz force, the magnetic field will bend the electron path so that the electron will spiral in the bended magnetic field and circle around the center axis, being confined in the NG region. As more electrons are confined, more collisions will happen between gas atoms and electrons, which helps ionize the neutral argon atoms and sustain the plasma. The bending effect of the magnetic field is mass dependent, so argon ions will be far less affected. The exhausted electrons, after loss of kinetic energies due to multiple collisions with atoms and ions, will fly away from the CDS region towards the anode region without breaking or heating up the substrate surface.

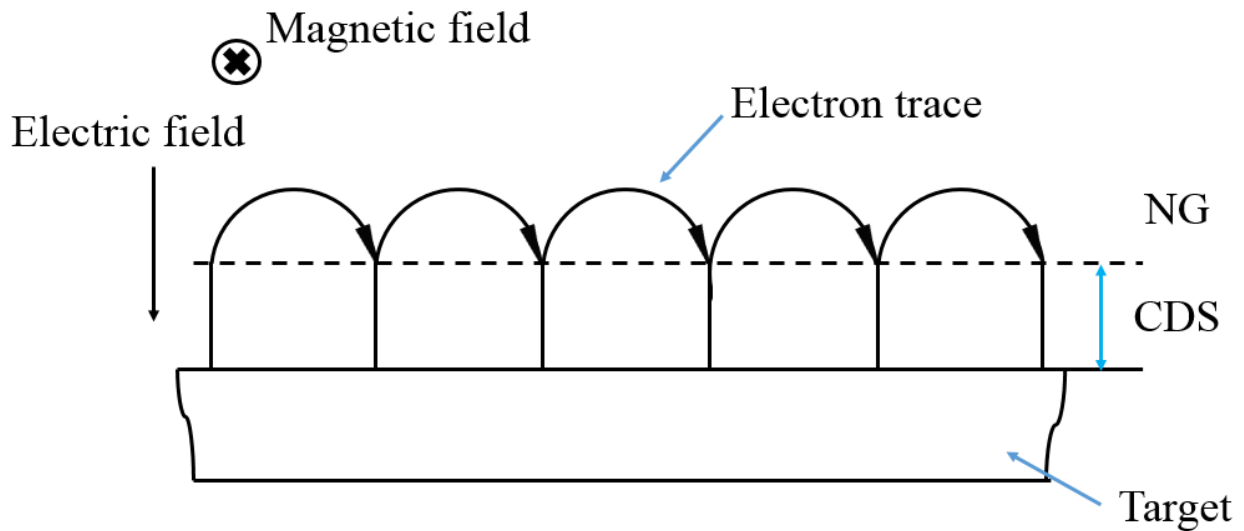


Figure 2.5. Cartoon illustration for field distribution and electron motion near the surface of the target. CDS and NG denote the cathode dark space and the negative glow regime, respectively.

On the other hand, argon ions will be accelerated under the electric field and move towards the cathode target materials with an energy range from 100 eV to 2000 eV, in which the collision

of argon ions and the atoms of the target surface can be modeled as hard sphere collisions in which the momentum transfer process dominates. Some relevant discussion is in Sec. 2.2.2. About 95% of the incident energy is transferred to heat in the target and only a small portion (about 5%) is absorbed by atoms (5–100 eV) on the surface. Target atoms will eject if the absorbed energy is larger than their binding energy. As most of the energy from argon ions is transferred to heat in the target, damage will occur to the cathode without proper cooling. In a magnetron sputtering gun, chilling water is supplied on the back to remove excessive heat. For high efficient momentum transfer, the atomic weight of the sputtering gas should be close to that of the target material. Argon gas is chosen as a compromise for light and heavy element atoms.

Target ions may also be ejected with a small portion (1-2%). These energetic ionized materials will fly to the substrates or the wall of the chamber, causing re-sputtering process. This process will contaminate the fabricated layer and should be suppressed. A moderate increase in the argon pressure will help suppress this re-sputtering process by slowing down such ionized materials with multiple collisions. There are also electrons ejected from the target surface as mentioned in Appendix A, which will help sustain the plasma.

As target atoms (5–100 eV) move through the plasma and the neutral gas phase, they collide with argon atoms and ions as well as electrons. This process can be treated as random walk and will make the energy of target atoms further down to 1 – 10 eV. This is critical for film formation because such an energy range is large enough for the atoms to stick to the substrates but sufficiently small to avoid being bounced back from the substrate surface. Some more details are provided in Appendix B for interested readers.

In DC magnetron sputtering process, positive charges will build up at the target surface and can be conducted away for metallic targets. For ceramic targets like YIG, positive charges will

accumulate and block the sputtering process. Thus, an alternating electric potential instead of a DC field is applied between targets and substrates to remove accumulated excessive electrons. Figure 2.6 shows the pace of the alternating potential and sputtering process occurs when the target is negative. The typical frequency for the alternating potential is in the MHz range. The reason is as follows.

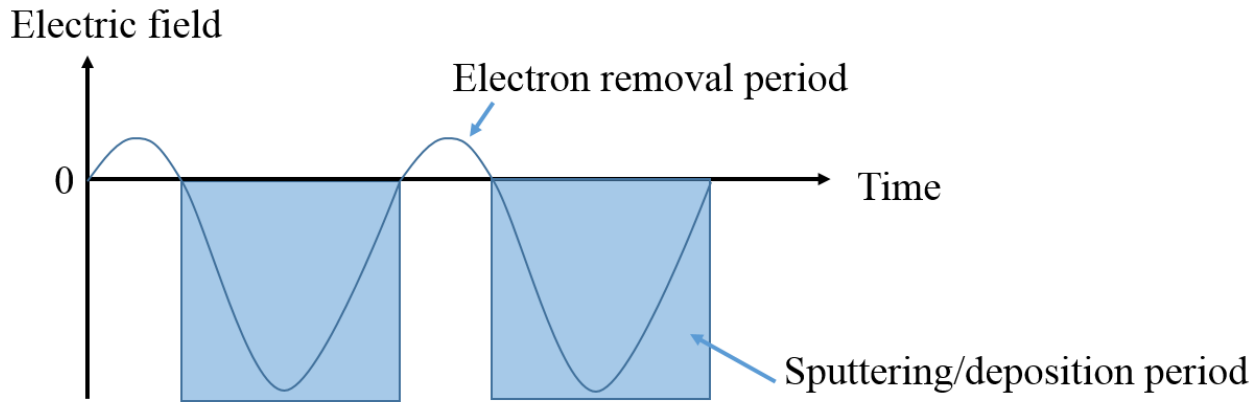


Figure 2.6. Alternating electric field for excessive electron removal. A reversed electric field with a small amplitude for a quarter of the period is applied for electron removal. The rest of the period is for sputtering and deposition.

For an RF electric field with a frequency less than about 50 kHz, electrons and ions in the plasma are mobile. Both will follow the switching pattern of the anode and cathode. In this situation, two steps happen within one period. For the first three quarters of the period, the target surface is the cathode and the substrate is the anode. Normal sputtering process happens on the target surface and the deposition process happens on the substrate side. For the last quarter of the period, the sign of the electric field is switched and the target surface becomes the anode while the substrate becomes the cathode. In this case, the sputtering process will happen on the substrate surface and the deposition will happen on the target. This process will damage the substrate surface and contaminate the target. To avoid this situation, the frequency of the electric field needs to be much higher than 50 kHz so that ions with heavy mass can no longer follow the

electric field switching pattern while electrons can respond to the switching and neutralize positive charge built up on the target surface.

The magnetron sputtering system used in the laboratory was from AJA Inc. It has two chambers. One is for metallic material deposition with three magnetron guns. The other has a face-to-face setup for ceramic material deposition. A heating box is on the back of the substrate holders for high-temperature (up to 800 °C) deposition and in-situ annealing. Both DC and RF (alternating frequency=13.56 MHz) sputtering modes are available. The substrate holders can rotate, allowing for uniform deposition. Beside argon gas, nitrogen and oxygen gases are available during deposition as supplement to improve thin film texture. The maximum gas flow rate is 20 sccm. In this dissertation, all the thin films were fabricated by using this magnetron sputtering system unless otherwise noted.

### 2.2.2 Deposition process, film formation, and ion etching process

Deposition, film formation, and ion etching are extremely complicated physical processes. Here, a one-dimensional linear chain model<sup>49</sup> under harmonic approximation is utilized to facilitate qualitative discussions on atom trapping and dissociation phenomena.

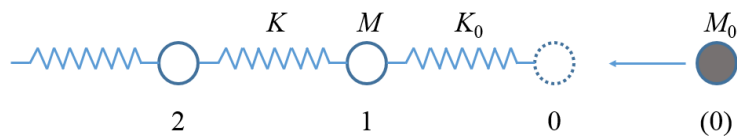


Figure 2.7. Cartoon of a one-dimensional linear chain model. The hollow spheres represent lattice particles in crystals, and the shaded one represents the incident particle.

A schematic diagram of the model is shown in Fig. 2.7. The hollow spheres represent the ions (mass  $M$ ) in the crystal of the substrate which interact with the nearest neighbors through

<sup>49</sup> B. McCarroll and G. Ehrlich, J. Chem. Phys. **38**, 523 (1963).

harmonic oscillation (force constant  $K$ ). The shaded sphere represents an incident atom with mass  $M_0$ . When the incident particle arrives at position 0, it starts to interact with the first lattice particle. Such interaction is described by a harmonic potential with a force constant  $K_0$ . The details of derivation and the program for the calculation of the results in Fig. 2.8-2.10 are given in Appendixes B and C for interested readers. Some main results and analysis are presented below.

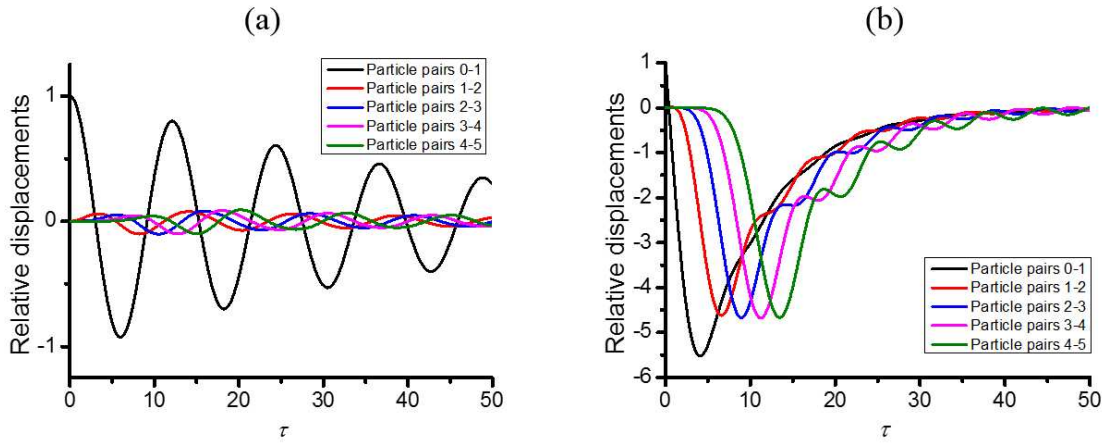


Figure 2.8. Relative displacements of adjacent particle pairs of atoms in the crystal chain as a function of dimensionless time  $\tau = 2\sqrt{K/M}t$ . 0 represents the incident particle, as shown in Fig. 2.7. Displacements and velocities are normalized with respect to the initial relative displacement of particle pair 0-1. (a)  $M_0/M = 0.1$ ,  $K_0/K = 0.1$ , and an initial velocity of 0 for light mass and weak force constant of the incident particle; (b)  $M_0/M = 5$ ,  $K_0/K = 0.8$ , and an initial velocity of -2.5 for heavy mass and strong force constant of the incident particle.

Two extreme cases are discussed first. Figure 2.8 shows the relative displacements of adjacent particle pairs of atoms in the crystal chain as a function of dimensionless time. 0 represents the incident particle and other numbers represent the particle in the one-dimensional crystal. For Fig. 2.8 (a), at  $\tau = 0$  the incident particle starts to interact with the first particle in the one-dimensional crystal. As the time evolves, both the incident particle and the crystal particles oscillate but with different amplitudes. The incident particle can take almost free oscillation with slow decay in amplitude and is hardly captured by the crystal because of the very

weak interaction. So the binding energy transmitted to the lattice is low. The crystal lattice will also oscillate in response to the incident particle but with a quite smaller amplitude. This is because the mass of the incident particle is very small. For Fig. 2.8 (b), the situation is quite different. Due to the heavy mass, strong interaction with crystal particles, and big initial incident velocity of the incident particle, the crystal particles are punched deeply into the crystal, causing dislocation, surface defects, and other defects.

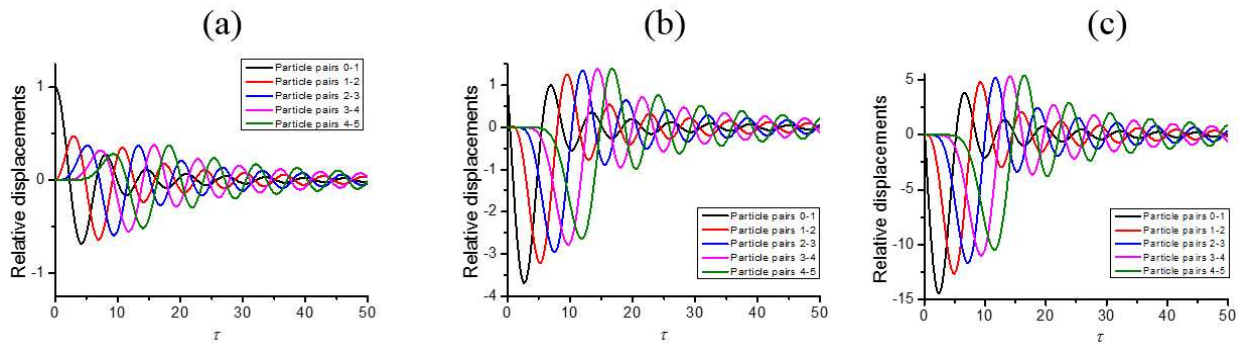


Figure 2.9. Relative displacements of adjacent particle pairs of atoms in a crystal chain as a function of dimensionless time  $\tau = 2\sqrt{K/M}t$ .  $M_0/M = 1$  and  $K_0/K = 1$ . (a) Initial velocity equal to 0; (b) initial velocity equal to -4.96; (c) initial velocity equal to -20.

Next, the case where the incident particle has an identical mass and an interaction constant with the lattice atoms is considered. On the contrary with the case of Fig. 2.8 (a), the binding energy is rapidly transmitted to the lattice even after the first oscillation period even with an initial velocity equal to 0, as shown in Fig. 2.9(a). In this case, the approach to the equilibrium state is more rapid. This particle capture process is critical for deposition in sputtering techniques. A further increase in the initial velocity from 0 will increase the oscillation amplitude of the lattice atoms. Figure 2.9(b) shows a critical point where the incident particle will bounce back to the original incident position with zero velocity after the first oscillation period. As seen from Fig. 2.9 (b), the oscillation amplitude of the lattice atoms is even bigger than that of the incident particle. This is an indication for startup of potential lattice particle dissociation, which

depicts the process of the ion etching process or the atom dissociation process. The critical point divides the collision into two opposite processes: (1) Deposition process (particle capture) for lower incident velocity (kinetic energy) and (2) etching process (lattice particle dissociation) for higher incident velocity (kinetic energy). In the magnetron sputtering chamber, ions in plasma with high kinetic energies collide with target materials and etching process takes place. Target atoms will bound up and move to the substrate under the electric field. Collisions between target atoms and particles in plasma help decrease the kinetic energy and the deposition process takes place at the substrate surface. Thus, target atoms are captured by the substrate and a thin film is formed. The critical energy for given relative mass ratio  $M_0 / M$  and interaction constant ratio  $K_0 / K$  is shown in Fig. 2.10.

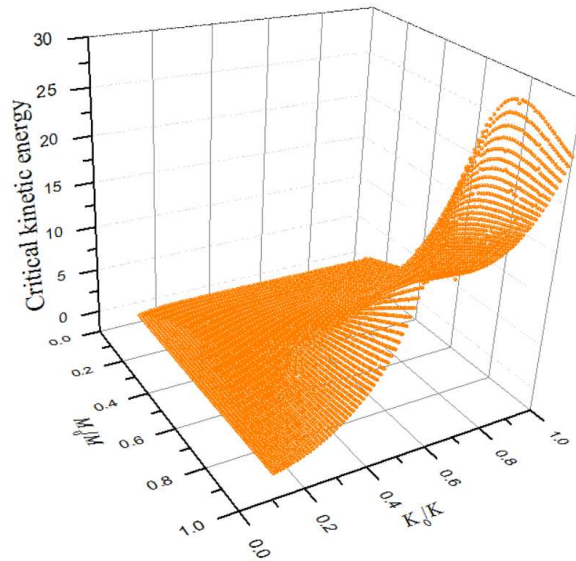


Figure 2.10. Critical kinetic energy of the incident particle as a function of  $M_0 / M$  and  $K_0 / K$ . The kinetic energy is scaled to  $\frac{1}{2} K [x_1(0)]^2$ , the energy necessary for extracting the end particle from a homogeneous linear lattice. Note that  $x_1(0)$  is the initial relative displacement of particle pair 0-1.

The concept of the critical point dividing the deposition and etching processes can be intuitive and applied to analysis in actual deposition/etching processes. Take YIG thin film

deposition as an example. If the argon pressure is a little higher than a baseline, the kinetic energy of the incident particles (Y, Fe, and O) is below the critical kinetic energy and the deposition process takes place with a normal rate (~1 nm/min). With a lower argon pressure, the kinetic energy of the incident target atoms will increase. This, on one hand, will make the deposition rate increase as higher kinetic energy leads to faster deposition. On the other hand, however, the quality of the YIG thin films may become low because the etching process will gradually arise near the critical point which leads to the dissociation and surface defects of the substrates as well as the deposited thin film. A further decrease of the argon pressure (~5 mTorr) will lead to a serious dissociation and etching case. This situation corresponds to Fig. 2.9(c) where the kinetic energies of the incident particles are huge due to low argon pressure. As shown in Fig. 2.9(c), the relative displacements of particles on the lattice are much bigger than those in Fig. 2.9(a) and (b), indicating a bond-breaking and dissociation of particles at substrate surfaces.

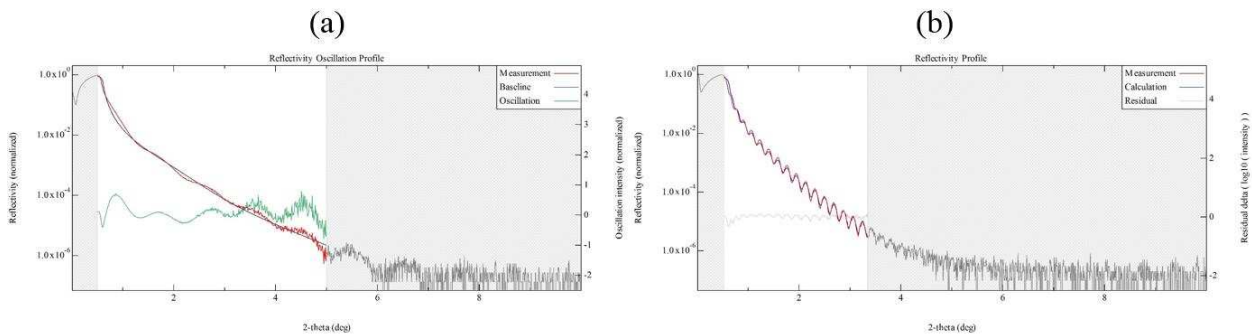


Figure 2.11. X-ray reflectometry data for Cr<sub>2</sub>O<sub>3</sub> deposited with identical control parameters but different RF power. (a) 50 W; (b) 75 W.

Another example is the sputtering process of Cr<sub>2</sub>O<sub>3</sub> thin films. The kinetic energies of incident target atoms can be tuned by controlling the output power of the electric field. Figure 2.11 shows the x-ray reflectometry data for Cr<sub>2</sub>O<sub>3</sub> thin films deposited with different RF powers. The thin film deposited with 75 W RF power and 30 min shows a normal oscillation curve, as presented in Fig. 2.11 (b), with a thickness of 45.8 nm. The film deposited with 50 W RF power

and 30 min, in a contrast, has a thickness of 7.6 nm only and low quality indicated by a poor fit. With the 50 W power the kinetic energies of the target atoms are too low ( $< 1$  eV) for particle capture and adhesion. This situation corresponds to the case shown in Fig. 2.8 (a) where incident particles have little interaction and energy transfer with the lattice.

The limitation of this one-dimensional linear chain model for particle deposition, adhesion, etching, and dissociation includes ignorance of anharmonicity, finite temperature, lattice defects, and restriction of three-dimensional motion to one dimension. In real materials, oblique collision, diffusions, and nucleation of incident particles happen and thereby make the deposition and etching processes much more complicated. In spite of the severe limitations of this model, some qualitative features of the calculation, such as the existence of critical point of the kinetic energy of incident particles for dividing deposition, etching, and punching processes, should still be valid and intuitive in the three-dimensional case.

## **2.3 Measurement techniques**

### **2.3.1 X-ray diffraction**

X-ray diffraction techniques utilized x-ray to determine the atomic structure of crystals, either bulk or thin films. In a typical configuration, a fine focused monochromatic beam of x-rays is beamed at samples and scattered elastically, forming diffraction patterns. The angles and intensities of these diffraction patterns provide information on lattice constants, chemical bonds, lattice types, and others.

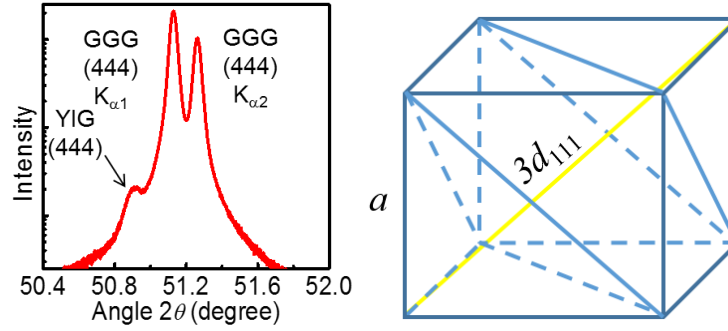


Figure 2.12. Left: X-ray  $2\theta$  scan spectrum of an 11-nm-thick YIG film. Right: illustration of the lattice constant  $a$  and spacing  $d_{111}$  along  $\langle 111 \rangle$ .

The left graph of Fig. 2.12 shows the YIG and GGG substrate peaks of a typical x-ray  $2\theta$  scan with a Bruker D8 system in the Central Instrument Facility (CIF) at Colorado State University (CSU). The  $2\theta$  angle of the YIG (444) peak is  $\sim 50.9^\circ$ . The wavelength of the Cu x-ray source is 0.154 nm ( $K_{\alpha}$ ). With these parameters, one can estimate the YIG lattice constant by using the Braggs law

$$2d \sin \theta = n\lambda \quad (2.2)$$

where  $d$  is the spacing between neighboring diffraction planes in the crystal,  $n$  is a positive integer indicating the Miller index which is 4 here, and  $\lambda$  is the x-ray wavelength. One can calculate the lattice constant  $a$  as  $a = 3d_{111}/\sqrt{3} = 3 \times (4\lambda / 2 \sin \theta) / \sqrt{3} = 12.414 \text{ \AA}$ . This value is close to the standard value which is  $12.376 \text{ \AA}$  at room temperature.

### 2.3.2 Atomic force microscopy

Atomic force microscopy (AFM) is a typical surface scanning technique and can have a resolution better than one nanometer. By measuring the atomic force between the probe tip and the sample, surface information like height, friction, and magnetism can be detected and acquired.



Figure 2.13. Pictures of the AFM device used in the magnetic laboratory at CSU.

Figure 2.13 shows the AFM device used in the magnetic laboratory at CSU. This Veeco Innova AFM device can support typical surface imaging with tapping and contact modes. A high-resolution microscopy on top of the probing block is for precise operations of tip mounting and laser beam alignment.

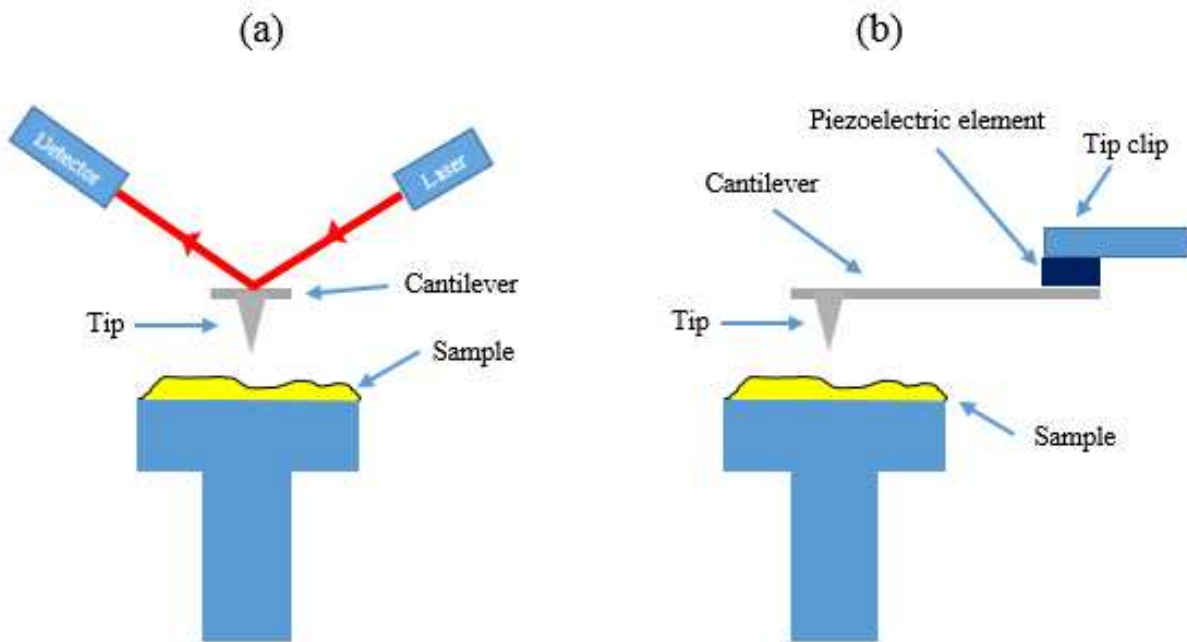


Figure 2.14. Front view (a) and side view (b) of the AFM configuration.

Figure 2.14 shows the configuration of the AFM device. The laser is beamed onto the back of the tip and reflected back into a photo diode, as shown in Fig. 2.14 (a). The tip oscillates at its

eigen-frequency and is controlled by a piezoelectric element through the cantilever, as shown in Fig. 2.14 (b). When the cantilever is scanning across the surface of the sample, the tip is tapping or contacting with the surface of the sample. Due to the atomic forces between the sample and the tip, the oscillating amplitude changes with the height of the surface, leading to deflection of the cantilever. This displacement is tracked by the angle and amplitude change of the reflected laser through the photodiode. Imaging information is then gathered, integrated, and displayed.

### 2.3.3 Vibrating sample magnetometry

Vibrating sample magnetometry (VSM) is a technique that measures magnetic properties of samples. Figure 2.15 shows the schematic of the key part of the VSM instrument. A quartz rod is suspended with the magnetic sample attached to one end. An electromagnet is used to magnetize the sample. By vibrating the quartz rod up and down with a high frequency, the coil can pick up a current signal from the changing magnetic field generated from the sample due to the Faraday's Law of Induction. By analyzing signal change with the external static magnetic field, magnetic properties of the sample such as saturation induction and coercivity can be acquired.

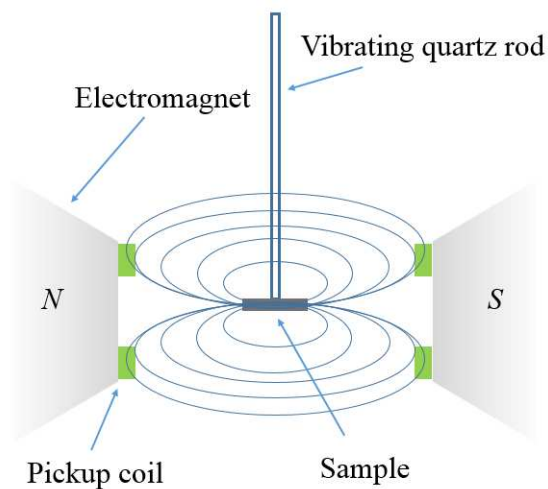


Figure 2.15. A schematic of the VSM instrument

### 2.3.4 Ferromagnetic resonance measurements

In real magnetic materials, magnetic moments can precess about the net magnetic field if they have a different orientation from the field. However, this precessional motion cannot be sustained without a continuous driving force. The interactions of magnon-phonon, magnon-electron, and magnon-magnon and other interactions will damp the precession and make it decay with time. This damping process is called magnetization relaxation.

Ferromagnetic resonance techniques have been widely used to study the magnetization dynamics, relaxation, spin transfer torques, domain wall motion, and magnetization switching in materials. The measurement of the FMR responses can provide information on magnetization dynamic properties, such as the Gilbert damping constant, as well as static magnetic properties, such as the saturation induction, anisotropy field, and gyromagnetic ratio.

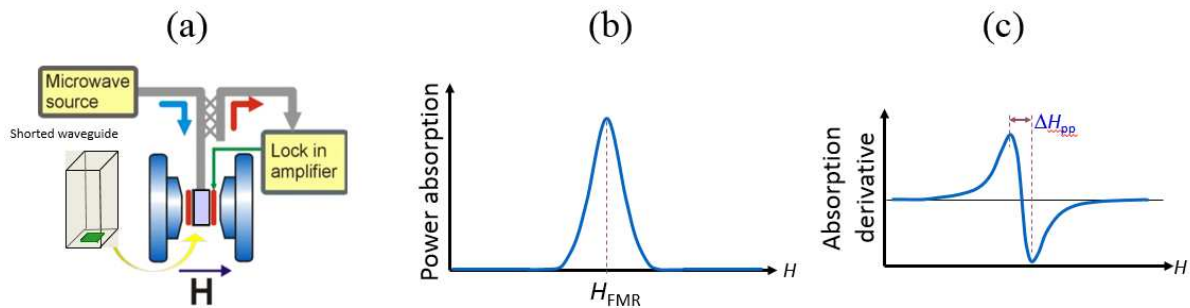


Figure 2.16. (a) The schematic for a typical FMR device using a rectangular waveguide, a lock-in amplifier, and an electromagnet. (b) A typical power absorption curve in an FMR measurement. (c) A typical curve of power absorption derivative in an FMR measurement with field modulation.

Fig. 2.16 (a) presents a schematic diagram of a typical FMR system. A sample is mounted at the end of a rectangular waveguide in which a microwave field can propagate and drive the magnetic moments in the sample. The electromagnets supply a constant external magnetic field to saturate the sample. The dynamic behavior of the magnetization in the sample can be described by the Gilbert equation Eq. 3.3. During the measurement, either the microwave

frequency or the external field is swept continuously till the resonance condition is satisfied. The FMR conditions can be predicted by the dispersion relations discussed in details in Chapter 3. At resonance, the power absorption reaches the maximum, and a peak (or a dip) as shown in Fig. 2.16 (b) will arise in the reflected microwave signal. Sometimes a lock-in amplifier and field modulation are utilized to enhance the signal-to-noise ratio. In this case, the detected signal will be the derivative of the absorption curve. The peak-to-peak linewidth shown in Fig. 2.16 (c) reflects the relaxation process. The relation between the FMR linewidth broadening and the Gilbert damping constant for the uniform resonance mode in a linear regime is described by Eq. 3.45. Reference [50] elaborates much details on the setup, calibration, and modification of the FMR system.

---

<sup>50</sup> C. Poole Jr., *Electron Spin Resonance: A Comprehensive Treatise on Experimental Techniques* (Interscience Publishers, New York, 1967).

## CHAPTER 3

# INTRODUCTION TO SPIN WAVE THEORY AND RELAXATION

Magnetization dynamics was first studied by Lev D. Landau and E. M. Lifshitz in 1935 with a phenomenological model.<sup>51</sup> Since then it has been studied for years in both bulk and thin film materials. Magnetic materials have been widely used in many areas like microwave applications, power conversion, and magnetic recording. Research on the behavior of magnetization dynamics is fundamental for the improvement of both applications in existing magnetic recording media and development of novel and new magnetic materials. The purpose of this chapter is to introduce briefly the concepts of magnetization dynamics and spin waves, especially ferromagnetic resonance (FMR) for thin films with consideration of different boundary conditions. Relaxation for the uniform resonance mode is also discussed. These are necessary for both understanding collective motion of spins in magnetic materials and study of FMR.

### 3.1 Equations of motion and boundary conditions for magnetic moments in materials

As mentioned in many textbooks,<sup>36-38</sup> the precession motion of a magnetic moment  $\vec{\mu}$  under a uniform magnetic field  $H$  can be described by

---

<sup>51</sup> L. Landau and E. Lifshitz, Physik. Zeits. Sowjetunion **8**, 153 (1935).

$$\frac{d\vec{\mu}}{dt} = -|\gamma|\vec{\mu} \times \vec{H} \quad (3.1)$$

where  $\gamma$  is the gyromagnetic ratio and is described by

$$|\gamma| = \left| g \frac{q}{2m_q} \right| \quad (3.2)$$

In Eq. (3.2),  $q$  is electron charge,  $m_q$  is the mass, and  $g$  is the Landé factor.  $g$  has the value 2 for a pure spin and 1 for pure orbital angular momenta. For the mixtures of the two, it has an intermediate value. In YIG materials, the magnetic moments are entirely from spins of electrons and one has  $|\gamma| = 2.8$  MHz/Oe. The orbital magnetic moments are “quenched”.<sup>36</sup> As described by Eq. (3.1), the magnetic moment precesses around the direction of the uniform magnetic field and never reaches the equilibrium position. The equation conserves both the energy and the magnitude of the magnetic moment.

For a macroscopic magnetization vector  $\vec{M}$  representing the mass spins per unit volume, its motion under an external field can be described by a similar equation but a damping term should be added for description of energy dissipation and absorption in real materials. L. Landau and E. Lifshitz proposed a term<sup>51</sup> to obtain a phenomenological equation of the spin dynamics. Later T. Gilbert suggested a viscous force<sup>52,53</sup> term in 1955 to the equation of precession motion Eq. (3.1) which is more favorable because it predicts slower motion with increasing damping as well as fits for numerical computing:

$$\frac{d\vec{M}(\vec{r}, t)}{dt} = -|\gamma|\vec{M}(\vec{r}, t) \times \vec{H}_{eff}(t) + \frac{\alpha}{M_s} \vec{M}(\vec{r}, t) \times \frac{d\vec{M}(\vec{r}, t)}{dt} \quad (3.3)$$

---

<sup>52</sup> T. Gilbert and H. Ekstein, Bull. Amer. Phys. Soc. **1**, 25 (1956).

<sup>53</sup> T. Gilbert, IEEE Trans. Magn., **40**, 3443 (2004).

In the Gilbert equation Eq. (3.3), the second term in the right hand, or the damping torque term, points towards the precession axis and thereby drags the magnetization back to the equilibrium position.  $\alpha$  is the Gilbert damping constant and is dimensionless.  $\vec{M}$  represents the total magnetic moments in a unit volume and is defined as

$$\vec{M} = \sum_i \frac{\vec{\mu}_i}{V} \quad (3.4)$$

where  $\mu_i$  is the spin on site  $i$  and  $V$  is the volume.  $\vec{H}_{eff}$  is the effective magnetic field applied to the magnetic moments including the static internal field, anisotropy field, dynamic dipolar field, dynamic exchange field, and others.

The collective motion of magnetic moments in materials under excitation is called spin waves or magnons in the wave picture of quantum mechanics. These magnetic waves have wavelengths much greater than the lattice parameters and propagate in low-loss ferromagnetic films for distances much greater than their wavelengths. In this section the problem of solving dispersion relations for dipole – exchange spin wave spectra with boundary conditions is mathematically formed with physical considerations and approximation added to Eq. (3.1). A general solution of the dispersion relations is derived in Sec. 3.2. The explicit form of dispersion relations for the uniform resonance mode is analyzed which is useful in the following chapters. Relaxation (or damping) mechanisms for the uniform resonance mode is discussed in Sec. 3.4.

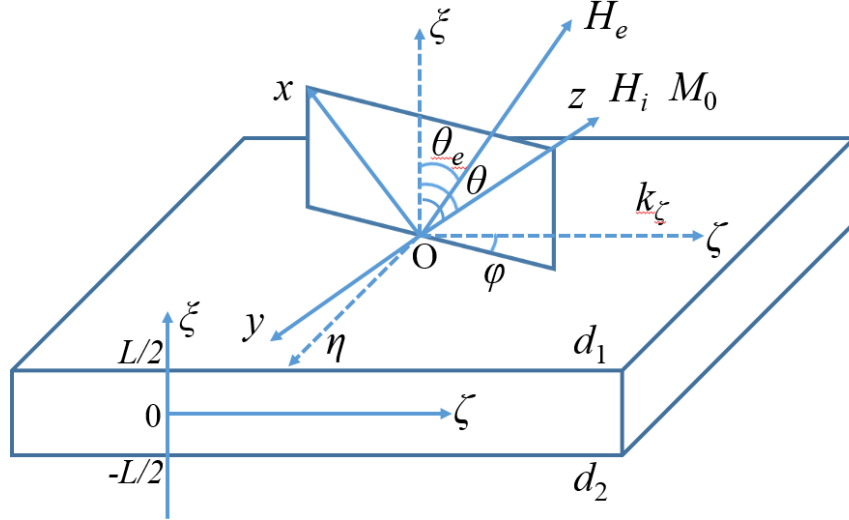


Figure 3.1. The coordinate configurations in the thin film sample

Figure 3.1 shows the configuration used in the dispersion relation derivation. A thin film is displayed as a cuboid. The external and internal fields are  $H_e$  and  $H_i$ , respectively. The magnetization of the film is  $M_0$ .  $(\xi, \eta, \zeta)$  and  $(x, y, z)$  are the two sets of coordinate systems. The thickness of the sample is  $L$  and the lateral dimension is sufficiently large that it can be assumed infinite. Axis  $\xi$  is perpendicular to the film plane and  $\zeta$  is set to parallel with the spin wave vector  $k_z$ . Axis  $z$  is along the magnetization direction and the angle between  $z$  and  $\xi$  is  $\theta$ . Axis  $y$  is in the film plane and perpendicular with  $z$ . The angle between the external magnetic field and  $\xi$  is  $\theta_e$ . The angle between the  $xz$  plane and  $\zeta$  is  $\phi$ . Parameters  $d_1$  and  $d_2$  are pinning parameters for top and bottom surfaces, respectively, with the form

$$d = \frac{K_S}{A_{ex}} \quad (3.5)$$

where  $K_S$  is the surface anisotropy constant and  $A_{ex}$  is the exchange coefficient with the unit of  $m^2$  in the Gaussian unit system<sup>54</sup>. The film is assumed to be fully saturated. The  $(x, y, z)$  coordinate system is introduced to conveniently describe the precession.

<sup>54</sup> R. Soohoo, Phys. Rev. **131**, 594 (1963).

First, dynamic interactions between spins in the material are discussed. Precessing magnetic moments confined in the material can interact with each other, for example, through dipole interaction and exchange interaction. For the dipole interaction, two magnetic moments in space will interact through magnetic fields and the potential energy of the interaction has the form

$$E = \frac{\mu_0}{4\pi r^3} \left[ \vec{\mu}_1 \cdot \vec{\mu}_2 - \frac{3}{r^2} (\vec{\mu}_1 \cdot \vec{r})(\vec{\mu}_2 \cdot \vec{r}) \right] \quad (3.6)$$

where  $\mu_0$  is the magnetic permeability constant in vacuum,  $r$  is the distance between the two moments, and  $\vec{\mu}_i$  is the magnetic moment vector ( $i = 1, 2$ ). Though a weak energy, it has a relatively longer interaction distance than that of the exchange interaction and is fundamental for spin waves with not-too-big wave vectors. Usually the dipole interaction can be described by a dipole field which is the effective field from all other magnetic moments acting on one magnetic moment in the material. Instead of a common method<sup>36</sup> used in many textbooks, a Green's function form of the dipole field is derived and used here for a more precise description. Details of the derivation for this dipole field in the Green's function form from Eq. (3.6) are provided in Appendix D for interested readers. Equation (3.7a) shows that the dipole field acting on one magnetic moment is the integral of contributions from all dynamic magnetic moments  $\vec{m}$ . Equation (3.7b) provides the exact form of the tensor. The subscripts mark the  $(\xi, \eta, \zeta)$  coordinate system shown in Fig. 3.1.

$$\vec{h}_d(\xi) = \int_{-L/2}^{L/2} \hat{G}_{\xi\eta\zeta}(\xi, \xi') \vec{m}(\xi') d\xi' \quad (3.7a)$$

$$\hat{G}_{\xi\eta\zeta}(\xi, \xi') = \begin{bmatrix} G_p - \delta(\xi - \xi') & 0 & iG_Q \\ 0 & 0 & 0 \\ iG_Q & 0 & -G_p \end{bmatrix} \quad (3.7b)$$

where

$$G_P = \frac{k_\zeta}{2} e^{-k_\zeta |\xi - \xi'|} \quad (3.7c)$$

$$G_Q = G_P \operatorname{sgn}(\xi - \xi') \quad (3.7d)$$

and  $k_\zeta$  is the wave vector of spin waves propagating along the  $\zeta$  direction. The dipole field described by Eq. (3.6) is the volume type which is important to spin waves with non-zero wave vectors. For a uniformly precessing mode, this contribution is zero as  $k_\zeta$  goes to zero. The other dipole field, the surface dipole field (or demagnetization field) induced by the surface magnetic moments, is approximately zero for spin waves with wavelengths much smaller than sample dimensions. However, it is critical for the uniform mode and is discussed in Appendix E.

Another important type of dynamic interaction between spins in the material is the exchange interaction which accounts for room-temperature ferromagnetism and is a quantum effect. ‘‘Exchange’’ refers to the property of electrons that leads to the Pauli exclusion principle. In the formation of magnetic crystals, as the ions get closer, electrons are shared and electrostatic energy arises from electrons being either closer together or further apart depending on whether they have the same spin orientation or not. The simplest form of the orientation-dependent interaction energy between spins of the  $i^{\text{th}}$  and  $j^{\text{th}}$  sites in the crystal is

$$E_{ij}^{\text{ex}} = -2J_{ij} \vec{S}_i \cdot \vec{S}_j \quad (3.8)$$

where  $J_{ij}$ , the exchange constant, has the dimension of energy and is positive for parallel alignment and negative for anti-parallel alignment. In a material, the following form

$$H_{\text{ex}} = A_{\text{ex}} \nabla^2 \vec{m} \quad (3.9)$$

is used<sup>36</sup> where  $A_{ex}$  is the exchange coefficient with the unit of  $m^2$  in the Gaussian unit system and  $\vec{m}$  represents the dynamic magnetic moment vector.

The static interactions between the spins and the external fields are discussed in Appendix E. The mathematical form of the magnetization (the total magnetic moments per unit volume)  $\vec{M}$ , under stimulation (like microwave) with an angular frequency  $\omega$ , can also be decomposed into the dynamic and static part as

$$\vec{M}(\vec{r}, t) = \vec{m}(\xi, \zeta, t) + M_0 \hat{z} \quad (3.10a)$$

where a slight decrease of the magnetization along the  $z$  direction is neglected for small-angle precession and  $\vec{m}(\xi)$  is also the dynamic component of the plane spin wave with the form

$$\vec{m}(\xi, \zeta, t) = \vec{m}(\xi) e^{i(\omega t - k_\zeta \zeta)} \quad (3.10b)$$

$M_0$  is the static component of the magnetization and is biased under the internal static magnetic field. As calculated in Appendix E, the relations between the static magnetic fields (the external uniform field, the demagnetization field, and the internal field) and the angles are

$$H_i \cos \theta = H_e \cos \theta_e - 4\pi M_0 \cos \theta \quad (3.11a)$$

$$4\pi M_0 \sin 2\theta = 2H_e \sin(\theta - \theta_e) \quad (3.11b)$$

$$H_i = H_e \cos(\theta - \theta_e) - 4\pi M_0 \cos^2 \theta \quad (3.11c)$$

Note that the magneto-crystalline anisotropy field is not considered here.

The total effective field, including the static and dynamic parts, for spin waves has the form

$$\vec{H}_{eff} = \vec{H}_i \hat{z} + \vec{h}_d(\vec{r}, t) + A_{ex} \nabla^2 \vec{m}(\vec{r}, t) \quad (3.12)$$

By inserting Eq. (3.10) and Eq. (3.12) into the Gilbert equation Eq. (3.3) and neglecting the

damping term, one can get

$$\frac{\partial}{\partial t} [M_0 \hat{z} + \vec{m}(\xi, \zeta, t)] = -|\gamma| [M_0 \hat{z} + \vec{m}(\xi, \zeta, t)] \times [\vec{H}_i \hat{z} + \vec{h}_d(\vec{r}, t) + A_{ex} \nabla^2 \vec{m}(\vec{r}, t)] \quad (3.13)$$

Neglecting the second order terms in Eq. (3.12) leads to the linearized form

$$\frac{\partial \vec{m}(\xi, \zeta, t)}{\partial t} = -|\gamma| \left\{ \vec{H}_i \vec{m}(\xi, \zeta, t) \times \hat{z} - M_0 [\vec{h}_d(\vec{r}, t) + A_{ex} \nabla^2 \vec{m}(\vec{r}, t)] \times \hat{z} \right\} \quad (3.14)$$

With some calculation given in Appendix F, a neat form is obtained

$$\hat{N} \cdot \vec{m}(\xi) = -i \frac{\omega}{\omega_M} \hat{T} \vec{m}(\xi) + \int_{-L/2}^{L/2} \hat{G}_{xy}(\xi, \xi') \vec{m}(\xi') d\xi' \quad (3.15)$$

where

$$\hat{I} = \begin{bmatrix} 1 & 0 \\ 0 & 1 \end{bmatrix}, \hat{T} = \begin{bmatrix} 0 & -1 \\ 1 & 0 \end{bmatrix}, \hat{N} = \left( -A_{ex} \frac{\partial^2}{\partial \xi^2} + A_{ex} k_\zeta^2 + \frac{\omega_H}{\omega_M} \right) \hat{I}$$

and

$$\omega_H \equiv |\gamma| H_i, \omega_M \equiv |\gamma| 4\pi M_0$$

Though not explicitly addressed, the dynamic magnetic moment vectors should be represented in the  $(x, y, z)$  coordinate system.

Boundary conditions are necessary for solving the integral-differential equation Eq. (3.15) and have the form<sup>54</sup>

$$\left\{ \frac{\partial m^x(\xi)}{\partial n} + d \cos 2\theta m^x(\xi) = 0 \right. \quad (3.16a)$$

$$\left. \frac{\partial m^y(\xi)}{\partial n} + d \cos^2 \theta m^y(\xi) = 0 \right\} \quad (3.16b)$$

where

$$\frac{\partial}{\partial n} = \begin{cases} \frac{\partial}{\partial \xi} & \text{if } \xi = L/2 \\ -\frac{\partial}{\partial \xi} & \text{if } \xi = -L/2 \end{cases}$$

The  $d$  is the pinning parameter mentioned in Fig. 3.1. Equations (3.15) and (3.16) complete the problem for solving the dispersion relations of dipole-exchange spin waves.

### 3.2 Dispersion relations for dipole-exchange spin waves

Mathematically it is impossible to get an analytical solution of the complete problem described by Eqs. (3.15) and (3.16). However, if  $\bar{m}$  can be expanded in a series of some proper complete orthogonal basis which also satisfies the boundary condition, an approximate solution can be acquired to any accuracy. The operator  $\hat{N}$  is chosen with the boundary conditions to form a general Sturm-Liouville (S-L) problem and addressed as follows.

$$\begin{cases} \hat{N}\bar{S}(\xi) = N\bar{S}(\xi) \\ \hat{B}_1\bar{S}(\xi) = 0 \text{ when } \xi = L/2 \\ \hat{B}_2\bar{S}(\xi) = 0 \text{ when } \xi = -L/2 \end{cases} \quad (3.17)$$

where

$$\hat{B}_1 = \begin{bmatrix} \frac{\partial}{\partial \xi} + d_1 \cos 2\theta & 0 \\ 0 & \frac{\partial}{\partial \xi} + d_1 \cos^2 \theta \end{bmatrix}$$

$$\hat{B}_2 = \begin{bmatrix} -\frac{\partial}{\partial \xi} + d_2 \cos 2\theta & 0 \\ 0 & -\frac{\partial}{\partial \xi} + d_2 \cos^2 \theta \end{bmatrix}$$

The subscripts 1 and 2 are for the upper and the lower surfaces of the film, respectively. A

detailed derivation for solving this ordinary differential equation is elaborated in Appendix G.

The eigenfunctions of the S-L problem are

$$\bar{S}_n^x(\xi) = \begin{pmatrix} \Phi_n^x(\xi) \\ 0 \end{pmatrix}, \quad \bar{S}_n^y(\xi) = \begin{pmatrix} 0 \\ \Phi_n^y(\xi) \end{pmatrix} \quad (3.18a)$$

where

$$\Phi_n^p(\xi) = A_n^p \left\{ \cos \left[ \kappa_n^p \left( \xi + \frac{L}{2} \right) \right] + \frac{d_2^p}{\kappa_n^p} \sin \left[ \kappa_n^p \left( \xi + \frac{L}{2} \right) \right] \right\} \quad (p = x, y) \quad (3.18b)$$

and the transverse wavenumber  $\kappa_n^p$  of the spin wave obeys

$$\left[ (\kappa_n^p)^2 - d_1^p d_2^p \right] \tan(\kappa_n^p L) = \kappa_n^p (d_1^p + d_2^p) \quad (3.18c)$$

where

$$d_{1,2}^x = d_{1,2} \cos 2\theta \quad d_{1,2}^y = d_{1,2} \cos^2 \theta$$

The eigenvalues are

$$N_n^p = \frac{\omega_H}{\omega_M} + A_{ex} \left[ k_\zeta^2 + (\kappa_n^p)^2 \right] \quad (3.19)$$

The eigenfunctions have the orthonormality property as

$$\left( S_n^p(\xi), S_m^q(\xi) \right) = L \delta_{nm} \delta_{pq} \quad (3.20)$$

where the bracket denotes the integral across the thickness of the thin film sample and  $\delta$  is the Kronecker function. The amplitude of the eigenfunctions  $A_n^p$  in Eq. (3.18b) can be acquired from the normalization condition Eq. (3.20) and is derived in detail in Appendix H for interested readers.

The series solution of Eq. (3.17) can be expanded on an orthogonal basis of the operator  $\hat{N}$  as

$$\vec{m}(\xi) = M_0 \sum_n \left( m_n^x \vec{S}_n^x(\xi) + m_n^y \vec{S}_n^y(\xi) \right) \quad (3.21)$$

Let us now come back to the complete problem of spin waves. By substituting Eq. (3.21) into Eq. (3.15), one can get

$$\begin{aligned} \sum_n \left[ m_n^x N_n^x \begin{pmatrix} \Phi_n^x(\xi) \\ 0 \end{pmatrix} + m_n^y N_n^y \begin{pmatrix} 0 \\ \Phi_n^y(\xi) \end{pmatrix} \right] = -i \frac{\omega}{\omega_M} \sum_n \left[ m_n^x \begin{pmatrix} 0 \\ \Phi_n^x(\xi) \end{pmatrix} - m_n^y \begin{pmatrix} \Phi_n^y(\xi) \\ 0 \end{pmatrix} \right] + \\ \sum_n \int_{-L/2}^{L/2} \hat{G}_{xy}(\xi, \xi') \left[ m_n^x \begin{pmatrix} \Phi_n^x(\xi') \\ 0 \end{pmatrix} + m_n^y \begin{pmatrix} 0 \\ \Phi_n^y(\xi') \end{pmatrix} \right] d\xi' \end{aligned} \quad (3.22)$$

The only undetermined term is the tensor of the Green's function  $\hat{G}_{xy}$  in the  $xy$  plane. Details of the derivation are in Appendix I for interested readers. By inserting the explicit form of the two-dimensional Green's function tensor

$$\hat{G}_{xy}(\xi, \xi') = \begin{bmatrix} -AG_p + \frac{B}{2}iG_Q - \delta(\xi - \xi')\sin^2\theta & \frac{D}{2}iG_Q - CG_p \\ \frac{D}{2}iG_Q - CG_p & -EG_p \end{bmatrix} \quad (3.23)$$

in Eq. (3.22), one can then obtain the second term on the right side of Eq. (3.22) as

$$\begin{aligned} & \sum_n \int_{-L/2}^{L/2} \hat{G}_{xy}(\xi, \xi') \left[ m_n^x \begin{pmatrix} \Phi_n^x(\xi') \\ 0 \end{pmatrix} + m_n^y \begin{pmatrix} 0 \\ \Phi_n^y(\xi') \end{pmatrix} \right] d\xi' \\ &= \sum_n \int_{-L/2}^{L/2} \begin{bmatrix} -AG_p + \frac{B}{2}iG_Q - \delta(\xi - \xi')\sin^2\theta & \frac{D}{2}iG_Q - CG_p \\ \frac{D}{2}iG_Q - CG_p & -EG_p \end{bmatrix} \left[ m_n^x \begin{pmatrix} \Phi_n^x(\xi') \\ 0 \end{pmatrix} + m_n^y \begin{pmatrix} 0 \\ \Phi_n^y(\xi') \end{pmatrix} \right] d\xi' \\ &= \sum_n \int_{-L/2}^{L/2} \left[ m_n^x \begin{pmatrix} -AG_p + \frac{B}{2}iG_Q \\ \frac{D}{2}iG_Q - CG_p \end{pmatrix} \Phi_n^x(\xi') + m_n^y \begin{pmatrix} \frac{D}{2}iG_Q - CG_p \\ -EG_p \end{pmatrix} \Phi_n^y(\xi') \right] d\xi' - \sum_n m_n^x \sin^2\theta \begin{pmatrix} \Phi_n^x(\xi) \\ 0 \end{pmatrix} \end{aligned}$$

Then the explicit form of Eq. (3.22) is

$$\begin{aligned}
& \sum_n \left[ m_n^x N_n^x \begin{pmatrix} \Phi_n^x(\xi) \\ 0 \end{pmatrix} + m_n^y N_n^y \begin{pmatrix} 0 \\ \Phi_n^y(\xi) \end{pmatrix} \right] = -i \frac{\omega}{\omega_M} \sum_n \left[ m_n^x \begin{pmatrix} 0 \\ \Phi_n^x(\xi) \end{pmatrix} - m_n^y \begin{pmatrix} \Phi_n^y(\xi) \\ 0 \end{pmatrix} \right] + \\
& \sum_n \int_{-L/2}^{L/2} \left[ m_n^x \begin{pmatrix} -AG_p + \frac{B}{2}iG_Q \\ \frac{D}{2}iG_Q - CG_p \end{pmatrix} \Phi_n^x(\xi') + m_n^y \begin{pmatrix} \frac{D}{2}iG_Q - CG_p \\ -EG_p \end{pmatrix} \Phi_n^y(\xi') \right] d\xi' - \sum_n m_n^x \sin^2 \theta \begin{pmatrix} \Phi_n^x(\xi) \\ 0 \end{pmatrix} \quad (3.24)
\end{aligned}$$

Equation (3.24) provides the explicit form of equations for spin wave amplitudes  $m_n^x$  and  $m_n^y$ .

After simplification (see Appendix J), a compact form of Eq. (3.24) is acquired as

$$\hat{D}_{nn} \bar{m}_n + \sum_{n' \neq n} \hat{R}_{nn'} \bar{m}_{n'} = 0 \quad (3.25)$$

where

$$\bar{m}_n = \begin{pmatrix} m_n^x \\ m_n^y \end{pmatrix}$$

$$\hat{D}_{nn} = \begin{bmatrix} N_n^x + \sin^2 \theta + AP_{nn}^{xx} & CP_{nn}^{xy} - i \left( \frac{\omega}{\omega_M} T_{nn}^{xy} - DQ_{nn}^{xy} \right) \\ CP_{nn}^{yx} + i \left( \frac{\omega}{\omega_M} T_{nn}^{yx} + DQ_{nn}^{yx} \right) & N_n^y + EP_{nn}^{yy} \end{bmatrix} \quad (3.26a)$$

$$\hat{R}_{nn'} = \begin{bmatrix} AP_{nn'}^{xx} + iBQ_{nn'}^{xx} & CP_{nn'}^{xy} - i \left( \frac{\omega}{\omega_M} T_{nn'}^{xy} - DQ_{nn'}^{xy} \right) \\ CP_{nn'}^{yx} + i \left( \frac{\omega}{\omega_M} T_{nn'}^{yx} + DQ_{nn'}^{yx} \right) & EP_{nn'}^{yy} \end{bmatrix}$$

$$P_{nn'}^{pp'}(k_\zeta) = P_{n'n}^{p'p}(k_\zeta) = \frac{1}{L} \int_{-L/2}^{L/2} \int_{-L/2}^{L/2} G_p(\xi, \xi', k_\zeta) \Phi_n^p(\xi) \Phi_{n'}^{p'}(\xi') d\xi d\xi' \quad (3.26b)$$

$$Q_{nn'}^{pp'}(k_\zeta) = -Q_{n'n}^{p'p}(k_\zeta) = \frac{1}{2L} \int_{-L/2}^{L/2} \int_{-L/2}^{L/2} G_Q(\xi, \xi', k_\zeta) \Phi_n^p(\xi) \Phi_{n'}^{p'}(\xi') d\xi d\xi' \quad (3.26c)$$

$$T_{nn'}^{pp'} = T_{n'n}^{p'p} = \frac{1}{L} \int_{-L/2}^{L/2} \Phi_n^p(\xi) \Phi_{n'}^{p'}(\xi) d\xi \quad (3.26d)$$

$$\begin{aligned}
A &= \cos^2 \varphi - (1 + \cos^2 \varphi) \sin^2 \theta \\
B &= -2 \cos \varphi \sin 2\theta \\
C &= \cos \theta \sin \varphi \cos \varphi \\
D &= -2 \sin \theta \sin \varphi \\
E &= \sin^2 \varphi
\end{aligned}$$

The physical significance of the two terms in Eq. (3.25) is interpreted as follows.  $\hat{D}_{nn}$  describes the dynamic behavior of spin waves with a given mode  $n$  without perturbation from other spin waves and  $\hat{R}_{nn'}$  describes the perturbation and interaction from other spin wave modes  $n'$  through dipole interaction on mode  $n$ .

Mathematically the exact dispersion relations for propagating spin waves can be achieved by calculating the eigenvalues of the determinant of the infinite system of Eq. (3.25). However, a zero-order dispersion relation for dipole-exchange spin waves is sufficient for deriving (quasi) ferromagnetic resonance uniform mode and calculated.

For the zero-order approximation without perturbation terms, Eq. (3.25) leads to

$$\det \hat{D}_{nn} = 0 \quad (3.27)$$

The corresponding vector amplitude of the spin wave with the mode index  $n$  is

$$\vec{m}_n^{(0)} = \begin{pmatrix} 1 \\ 1 \end{pmatrix}$$

So the dynamic magnetization of the eigenwave for the  $n$  mode is

$$\vec{m}_n(\xi) = m_0 [\Phi_n^x(\xi) \hat{x} + \Phi_n^y(\xi) \hat{y}]$$

Substituting Eq. (3.26a) into Eq. (3.27), one can get

$$\det \hat{D}_{nm} = \det \begin{bmatrix} N_n^x + \sin^2 \theta + AP_{nm}^{xx} & CP_{nm}^{xy} - i \left( \frac{\omega}{\omega_M} T_{nm}^{xy} - DQ_{nm}^{xy} \right) \\ CP_{nm}^{yx} + i \left( \frac{\omega}{\omega_M} T_{nm}^{yx} + DQ_{nm}^{yx} \right) & N_n^y + EP_{nm}^{yy} \end{bmatrix} = 0 \Rightarrow$$

$$(N_n^x + \sin^2 \theta + AP_{nm}^{xx})(N_n^y + EP_{nm}^{yy}) - \left[ CP_{nm}^{xy} - i \left( \frac{\omega}{\omega_M} T_{nm}^{xy} - DQ_{nm}^{xy} \right) \right] \left[ CP_{nm}^{yx} + i \left( \frac{\omega}{\omega_M} T_{nm}^{yx} + DQ_{nm}^{yx} \right) \right] = 0$$

This leads to, with some algebra and help from Eqs. (3.26b)-(3.26d),

$$\left( \frac{\omega_n}{\omega_M} T_{nm}^{yx} + DQ_{nm}^{yx} \right)^2 = \left( \frac{\Omega_n^x}{\omega_M} + \sin^2 \theta + AP_{nm}^{xx} \right) \left( \frac{\Omega_n^y}{\omega_M} + EP_{nm}^{yy} \right) - C^2 (P_{nm}^{yx})^2 \quad (3.28)$$

where

$$\Omega_n^p \equiv \omega_M N_n^p = \omega_H + \omega_M A_{ex} \left[ k_\zeta^2 + (\kappa_n^p)^2 \right]$$

The explicit forms of each term in Eq. (3.28) are

$$\omega_H = |\gamma| H_i, \quad \omega_M = |\gamma| M_0$$

$$P_{nm'}^{pp'}(k_\zeta) = P_{n'n}^{p'p}(k_\zeta) = J_1 + J_2$$

$$Q_{nm'}^{pp'}(k_\zeta) = -Q_{n'n}^{p'p}(k_\zeta) = \frac{J_1 - J_2}{2}$$

where

$$J_1 = \frac{k_\zeta A_n^{p'} A_n^p}{2L(k_n^{p'})^2} \left\{ \frac{(d_2^{p'} - k_\zeta)}{(k_n^p)^2} \left[ \frac{e^{-k_\zeta L} (\kappa_n^p)^2 - d_2^p k_\zeta}{\kappa_n^p} \sin \kappa_n^p L + (d_2^p + k_\zeta) (1 - e^{-k_\zeta L} \cos \kappa_n^p L) \right] - \right.$$

$$\frac{(d_2^{p'} - k_\zeta)}{2} \left[ \frac{\sin(\kappa_n^p + \kappa_n^{p'}) L}{\kappa_n^p + \kappa_n^{p'}} + \frac{\sin(\kappa_n^p - \kappa_n^{p'}) L}{\kappa_n^p - \kappa_n^{p'}} - \frac{d_2^p}{\kappa_n^p} \left( \frac{\cos(\kappa_n^p + \kappa_n^{p'}) L - 1}{\kappa_n^p + \kappa_n^{p'}} + \frac{\cos(\kappa_n^p - \kappa_n^{p'}) L - 1}{\kappa_n^p - \kappa_n^{p'}} \right) \right] +$$

$$\left. \frac{(\kappa_n^{p'})^2 + d_2^{p'} k_\zeta}{2\kappa_n^{p'}} \left[ \frac{1 - \cos(\kappa_n^p + \kappa_n^{p'}) L}{\kappa_n^p + \kappa_n^{p'}} + \frac{\cos(\kappa_n^p - \kappa_n^{p'}) L - 1}{\kappa_n^p - \kappa_n^{p'}} + \frac{d_2^p}{\kappa_n^p} \left( \frac{\sin(\kappa_n^p - \kappa_n^{p'}) L}{\kappa_n^p - \kappa_n^{p'}} - \frac{\sin(\kappa_n^p + \kappa_n^{p'}) L}{\kappa_n^p + \kappa_n^{p'}} \right) \right] \right\}$$

$$J_2 = \frac{k_\zeta A_n^{p'} A_n^p}{2L(k_n^{p'})^2} \left\{ \begin{aligned} & \left[ \frac{(\kappa_n^{p'})^2 - d_2^{p'} k_\zeta}{\kappa_n^{p'}} \sin \kappa_n^{p'} L - (k_\zeta + d_2^{p'}) \cos \kappa_n^{p'} L \right] \times \\ & \frac{e^{-k_\zeta L}}{(k_n^p)^2} \left[ e^{k_\zeta L} \frac{(\kappa_n^p)^2 + d_2^p k_\zeta}{\kappa_n^p} \sin \kappa_n^p L + (d_2^p - k_\zeta) (1 - e^{k_\zeta L} \cos \kappa_n^p L) \right] - \\ & \frac{(d_2^{p'} + k_\zeta)}{2} \left[ \frac{\sin(\kappa_n^p + \kappa_n^{p'}) L}{\kappa_n^p + \kappa_n^{p'}} + \frac{\sin(\kappa_n^p - \kappa_n^{p'}) L}{\kappa_n^p - \kappa_n^{p'}} - \frac{d_2^p}{\kappa_n^p} \left( \frac{\cos(\kappa_n^p + \kappa_n^{p'}) L - 1}{\kappa_n^p + \kappa_n^{p'}} + \frac{\cos(\kappa_n^p - \kappa_n^{p'}) L - 1}{\kappa_n^p - \kappa_n^{p'}} \right) \right] - \\ & \left. \frac{(\kappa_n^{p'})^2 - d_2^{p'} k_\zeta}{2\kappa_n^{p'}} \left[ \frac{1 - \cos(\kappa_n^p + \kappa_n^{p'}) L}{\kappa_n^p + \kappa_n^{p'}} + \frac{\cos(\kappa_n^p - \kappa_n^{p'}) L - 1}{\kappa_n^p - \kappa_n^{p'}} + \frac{d_2^p}{\kappa_n^p} \left( \frac{\sin(\kappa_n^p - \kappa_n^{p'}) L}{\kappa_n^p - \kappa_n^{p'}} - \frac{\sin(\kappa_n^p + \kappa_n^{p'}) L}{\kappa_n^p + \kappa_n^{p'}} \right) \right] \right\} \end{aligned} \right.$$

The derivation of the explicit forms of  $J_1$  and  $J_2$  is elaborated in Appendix K for interested readers. Equation (3.28) is the explicit form of the zero-order approximate dispersion relation for the propagating spin wave with the mode index  $n$ , and it finalizes the task of this section. The advantage of the method of derivation applied in Sections 3.1 and 3.2 for spin waves is to take into account the top and bottom boundary conditions. This is especially useful for calculation and applications in studies of dynamics in ferromagnetic magnetic thin films (e.g. YIG and barium hexagonal ferrites) with different adjacent top (vacuum, Pt, or topological insulators) and/or bottom (GGG or Pt) media. Some special cases and formulas are discussed in the next section which are frequently used through the dissertation.

### 3.3 Ferromagnetic resonance uniform modes

In this section, the dispersion relations for the uniform resonance mode is discussed where all precessing spins are parallel with each other. This is the mode excited by microwaves if the sample dimensions are much smaller than the wavelength of microwaves and is fundamental for characterizing magnetic properties in the samples. To find the dispersion relation, the explicit analytical form rather than the integral form of  $P_{nn'}^{pp'}(k_\zeta)$  and  $Q_{nn'}^{pp'}(k_\zeta)$  should be calculated. To avoid tedious calculations, the derivation is presented in Appendix K for interested readers.

For resonance modes (uniform or standing wave modes), as there is no propagating spin wave but resonances,  $k_z$  is zero which leads to zeros of  $P_{m'}^{pp'}(k_z)$  and  $Q_{m'}^{pp'}(k_z)$ . Then Eq. (3.28) can be simplified as

$$\omega_n = \frac{1}{|T_{mm}^{yx}|} \sqrt{\left(\omega_H + A_{ex}\omega_M (\kappa_n^y)^2\right) \left(\omega_H + A_{ex}\omega_M (\kappa_n^x)^2 + \omega_M \sin^2 \theta\right)} \quad (3.29)$$

Equation (3.29) is the dispersion relation for resonant spin waves with an arbitrary internal field direction and arbitrary exchange boundary conditions. From Eq. (3.18b), nonzero  $\kappa_n$  is related to standing wave modes across the thickness direction bounded and modified by boundary conditions. This standing wave mode is not considered here. With  $\kappa_n \rightarrow 0$ , Eq. (3.13b) indicates the (quasi-) uniform precession mode across the thickness. With some calculations, the dispersion relation, the amplitude of the magnetization and the relations between static fields are therefore

$$\omega_0 = \frac{1}{|T_{00}^{yx}|} \sqrt{\omega_H (\omega_H + \omega_M \sin^2 \theta)} \quad (3.30a)$$

$$\Phi_0^p(\xi) = (d_2^p - d_1^p) \xi + \sqrt{1 - \frac{L^2}{12} (d_2^p - d_1^p)^2} \quad (3.30b)$$

This is the (quasi-) uniform resonance mode for arbitrary external fields and arbitrary boundary conditions. It should be noted that, according to Eq. (3.18c), the (quasi-) uniform resonance mode requires  $d_1^p L \ll 1$  and  $d_2^p L \ll 1$ . In most experiments of the following chapters, the external field is either perpendicular or parallel to the film plane (namely along the principal axis). In this case  $\theta = \theta_e$ . Then Eq. (3.30a) is simplified as

$$f_{\perp} = \frac{|\gamma|}{|T_{00}^{yx}|} (H_e - 4\pi M_0) \quad (3.31a)$$

$$f_{//} = \frac{|\gamma|}{|T_{00}^{yx}|} \sqrt{H_e(H_e + 4\pi M_0)} \quad (3.31b)$$

where  $f$  is the microwave frequency, and  $4\pi M_0$  is the saturation magnetization.  $|T_{00}^{yx}|$  can be calculated from Eqs. (3.26d) and (3.30b)

$$|T_{00}^{yx}| = \left| \frac{L^2}{12} (d_2^x - d_1^x)(d_2^y - d_1^y) + \left[ 1 - \frac{L^2}{12} (d_2^x - d_1^x)^2 \right] \left[ 1 - \frac{L^2}{12} (d_2^y - d_1^y)^2 \right] + \left[ 1 - \frac{L^2}{12} (d_2^x - d_1^x)^2 \right] (d_2^y - d_1^y)L + \left[ 1 - \frac{L^2}{12} (d_2^y - d_1^y)^2 \right] (d_2^x - d_1^x)L \right|$$

The value of  $|T_{00}^{yx}|$  is very close to 1. The physical significance of  $|T_{00}^{yx}|$  is the shift of the frequency of the FMR mode due to non-uniform (linear) distribution of the magnetization amplitude under different boundary pinning conditions  $d_i^p$ . Only when the pinning conditions of the top and bottom surfaces are identical, the exact uniform precession mode exists and the magnetization amplitude is uniformly distributed across the thickness.

Another interesting phenomenon indicated by Eq. (3.31) is that the deposition of an adjacent layer on the ferromagnetic film may shift the resonance frequency. Further, this shift correlates to the pinning/coupling at the interface. For example, a layer of Pt/Cu deposited on an YIG film can shift the resonance frequency from that of the bare YIG film for 0 – 30 Oe.<sup>55</sup>

In the following chapters, most FMR fits assume that the resonance is uniform ( $|T_{00}^{yx}| \approx 1$ ) and the following formula derived from Eq. (3.31) is used for fitting.

$$f_{\perp} = |\gamma| (H_{FMR} - 4\pi M_{eff}) \quad (3.32a)$$

---

<sup>55</sup> Y. Sun, H. Chang, M. Kabatek, Y. -Y. Song, Z. Wang, M. Jantz, W. Schneider, M. Wu, E. Montoya, B. Kardasz, B. Heinrich, S. G. E. te Velthuis, H. Schultheiss, and A. Hoffmann, Phys. Rev. Lett. **111**, 106601 (2013).

$$f_{||} = |\gamma| \sqrt{H_{FMR} (H_{FMR} + 4\pi M_{eff})} \quad (3.32b)$$

The subscript “*eff*” indicates that there might be a potential uniaxial anisotropy field that is added to the saturation magnetization term. For other special cases and modes, the readers can refer to Appendix K.

### 3.4 Damping caused linewidth broadening in FMR measurements

In this section the linewidth broadening due to damped magnetization precession is discussed due to non-avoidable loss. Only the Gilbert model Eq. (3.3) and the ferromagnetic uniform resonance mode are related here.

For the uniform resonance mode, the amplitude of the dynamic magnetization is identical and independent of position. The exchange field and the volume dipole field are suppressed and neglected so that Eq. (3.10) is modified as

$$\begin{cases} \vec{M}(t) = M_0 \hat{z} + \vec{m}(t) \\ \vec{m}(t) = (m_{0x} \hat{x} + m_{0y} \hat{y}) e^{i\omega t} \end{cases} \quad (3.33)$$

The angle  $\varphi$  is zero in Fig. 3.1 and the transformation matrix (Appendix I) is modified as

$$\hat{T}_t = \begin{pmatrix} \sin \theta & 0 & \cos \theta \\ 0 & 1 & 0 \\ -\cos \theta & 0 & \sin \theta \end{pmatrix}, \quad \hat{T}_t^{-1} = \begin{pmatrix} \sin \theta & 0 & -\cos \theta \\ 0 & 1 & 0 \\ \cos \theta & 0 & \sin \theta \end{pmatrix}$$

A dynamic surface demagnetization field arises due to the precession of the magnetization,

$$\vec{h}_{de} = -4\pi \begin{bmatrix} N_\xi & 0 & 0 \\ 0 & N_\eta & 0 \\ 0 & 0 & N_\zeta \end{bmatrix} \begin{pmatrix} M_\xi \\ M_\eta \\ M_\zeta \end{pmatrix}$$

where

$$N_\xi + N_\eta + N_\zeta = 1$$

in the  $(\xi, \eta, \zeta)$  coordinate system. Both the sample geometry and the magnetization orientation will affect the demagnetization field. For magnetic thin films, one has  $N_\xi \approx 1$  and  $N_\eta = N_\zeta \approx 0$ . With the help of the transformation matrix, the demagnetization matrix in the  $(x, y, z)$  coordinate system is

$$\begin{aligned} \vec{h}_{de} &= -4\pi\hat{T}_t^{-1} \begin{bmatrix} 1 & 0 & 0 \\ 0 & 0 & 0 \\ 0 & 0 & 0 \end{bmatrix} \hat{T}_t \begin{pmatrix} m_{0x}e^{i\omega t} \\ m_{0y}e^{i\omega t} \\ 0 \end{pmatrix} \\ &= \begin{pmatrix} m_{0x}e^{i\omega t} \sin^2 \theta \\ 0 \\ m_{0x}e^{i\omega t} \sin \theta \cos \theta \end{pmatrix} \end{aligned} \quad (3.34)$$

The external magnetic field should include a dynamic component to compensate damping and stimulate precession. This dynamic component may originate from the applied microwave or other stimulation and is assumed to have the following form

$$\vec{h} = (h_{0x}\hat{x} + h_{0y}\hat{y})e^{i\omega t} \quad (3.35)$$

The effective field includes the internal field (the constant external field, the static demagnetization field), the dynamic external field, and the dynamic surface demagnetization field

$$\vec{H}_{eff} = H_i\hat{z} + \vec{h} + \vec{h}_{de} \quad (3.36)$$

By substituting Eqs. (3.33) and (3.36) into the Gilbert equation (Eq. (3.3)), one can get

$$\frac{d}{dt}(M_0\hat{z} + \vec{m}(t)) = -|\gamma|(M_0\hat{z} + \vec{m}(t)) \times [H_i\hat{z} + \vec{h} + \vec{h}_{de}] + \frac{\alpha}{M_s}(M_0\hat{z} + \vec{m}(t)) \times \frac{d(M_0\hat{z} + \vec{m}(t))}{dt}$$

With some calculations, the equation above can be re-organized as

$$\frac{d\vec{m}(t)}{dt} = -|\gamma| \left[ M_0 \hat{z} \times (\vec{h} + \vec{h}_{de}) + \vec{m}(t) \times H_i \hat{z} + \vec{m}(t) \times (\vec{h} + \vec{h}_{de}) \right] + \frac{\alpha}{M_S} \left[ M_0 \hat{z} \times \frac{d\vec{m}(t)}{dt} + \vec{m}(t) \times \frac{d\vec{m}(t)}{dt} \right]$$

With  $M_S \sim M_0$  and a small signal approximation which is valid for small angle precession, all the second and higher order terms in the above equation can be dropped. The linearized Gilbert equation is then expressed as

$$\frac{d\vec{m}(t)}{dt} = -|\gamma| \left[ M_0 \hat{z} \times (\vec{h} + \vec{h}_{de}) + \vec{m}(t) \times H_i \hat{z} \right] + \alpha \hat{z} \times \frac{d\vec{m}(t)}{dt}$$

By substituting Eqs. (3.34) and (3.35) and the explicit forms of each term in the effective field expression into the equation above, one can get

$$\begin{cases} |\gamma| M_0 h_{0y} = i\omega m_{0x} + |\gamma| H_i m_{0y} + \alpha i\omega m_{0y} \\ -|\gamma| M_0 h_{0x} = i\omega m_{0y} - |\gamma| (H_i + 4\pi M_0 \sin^2 \theta) m_{0x} - \alpha i\omega m_{0x} \end{cases}$$

The solutions for  $m_{0x}$  and  $m_{0y}$  are

$$\begin{pmatrix} m_{0x} \\ m_{0y} \end{pmatrix} = \begin{bmatrix} \chi_{xx} & i\kappa \\ -i\kappa & \chi_{yy} \end{bmatrix} \begin{pmatrix} h_{0x} \\ h_{0y} \end{pmatrix}$$

where the elements of the susceptibility tensor are given below.

$$\chi_{xx} = \frac{\gamma^2 H_i M_0 + \alpha i\omega |\gamma| M_0}{\gamma^2 H_i (H_i + 4\pi M_0 \sin^2 \theta) - \omega^2 + \alpha i\omega |\gamma| (2H_i + 4\pi M_0 \sin^2 \theta) - \alpha^2 \omega^2} \quad (3.37a)$$

$$\chi_{yy} = \frac{\gamma^2 (H_i + 4\pi M_0 \sin^2 \theta) M_0 + \alpha i\omega |\gamma| M_0}{\gamma^2 H_i (H_i + 4\pi M_0 \sin^2 \theta) - \omega^2 + \alpha i\omega |\gamma| (2H_i + 4\pi M_0 \sin^2 \theta) - \alpha^2 \omega^2} \quad (3.37b)$$

$$\kappa = \frac{\omega |\gamma| M_0}{\gamma^2 H_i (H_i + 4\pi M_0 \sin^2 \theta) - \omega^2 + \alpha i\omega |\gamma| (2H_i + 4\pi M_0 \sin^2 \theta) - \alpha^2 \omega^2} \quad (3.37c)$$

The real parts of the elements are related to the dispersive properties of the materials while the imaginary parts are related with the damping in the material. A typical value of the Gilbert

damping constant  $\alpha$  is small, from  $10^{-2}$  to  $10^{-5}$  dependent on the material. If terms with  $\alpha^2$  are dropped in the susceptibility tensor elements, one can get from Eq. (3.37)

$$\chi_{xx} \approx \frac{\gamma^2 H_i M_0 + \alpha i \omega |\gamma| M_0}{\gamma^2 H_i (H_i + 4\pi M_0 \sin^2 \theta) - \omega^2 + \alpha i \omega |\gamma| (2H_i + 4\pi M_0 \sin^2 \theta)} \quad (3.38a)$$

$$\chi_{yy} \approx \frac{\gamma^2 (H_i + 4\pi M_0 \sin^2 \theta) M_0 + \alpha i \omega |\gamma| M_0}{\gamma^2 H_i (H_i + 4\pi M_0 \sin^2 \theta) - \omega^2 + \alpha i \omega |\gamma| (2H_i + 4\pi M_0 \sin^2 \theta)} \quad (3.38b)$$

$$\kappa \approx \frac{\omega |\gamma| M_0}{\gamma^2 H_i (H_i + 4\pi M_0 \sin^2 \theta) - \omega^2 + \alpha i \omega |\gamma| (2H_i + 4\pi M_0 \sin^2 \theta)} \quad (3.38c)$$

The resonance happens when the real part of the denominator is set to zero.

$$\omega_{FMR} = |\gamma| \sqrt{H_i (H_i + 4\pi M_0 \sin^2 \theta)} \quad (3.39)$$

By substituting the expression of the internal field Eq. (3.11c) into Eq. (3.39), one can obtain

$$\omega_{FMR} = |\gamma| \sqrt{(H_e \cos(\theta - \theta_e) - 4\pi M_0 \cos^2 \theta)(H_e \cos(\theta - \theta_e) - 4\pi M_0 \cos 2\theta)} \quad (3.40)$$

For a perpendicular external field, one has  $\theta = \theta_e = 0$  and Eq. (3.40) is equivalent with Eq. (3.32a). For an in-plane external field, one has  $\theta = \theta_e = 90^\circ$ , and Eq. (3.40) is equivalent with Eq. (3.32b). This confirms the validity of the derivation and formulas obtained in Sec. 3.3.

FMR experiments involve the measurement of the microwave power absorbed by the sample which depends on the loss in the material. The time-averaged microwave power  $\langle P \rangle$  absorbed by the sample is connected with the imaginary part of the magnetic susceptibility tensor as<sup>56</sup>

---

<sup>56</sup> Two magnon scattering and relaxation in thin ferrite films by Michael Hurben, Ph. D., 238 pages, OCLC 35896674.

$$\langle P \rangle = \frac{1}{2} \omega h_{0x}^2 \text{Im}(\chi_{xx})$$

$$\text{Im}(\chi_{xx}) \approx \frac{-\alpha \omega |\gamma| M_0 (\omega^2 + |\gamma|^2 H_i^2)}{(\gamma^2 H_i (H_i + 4\pi M_0 \sin^2 \theta) - \omega^2)^2 + \alpha^2 \omega^2 \gamma^2 (2H_i + 4\pi M_0 \sin^2 \theta)^2}$$

The existence of damping in the material will broaden the linewidth of the resonance peak, as shown in Fig. 2.16 in Chapter 2. The half-power linewidth of the absorption curve can be expressed in the frequency spectrum as

$$\Delta\omega = \alpha |\gamma| (2H_i + 4\pi M_0 \sin^2 \theta) \quad (3.41)$$

In some FMR measurements and this dissertation, the frequency of the microwave is fixed and the external magnetic field is swept. The corresponding linewidth broadening in the field spectrum can be obtained by

$$\Delta H = \frac{\Delta\omega}{\left. \frac{\partial\omega}{\partial H_e} \right|_{FMR}} = \frac{2\alpha}{|\gamma| \cos(\theta - \theta_e)} \omega_{FMR} \quad (3.42)$$

Equation (3.42) indicates that the linewidth broadening in the magnetic field spectrum is linear with the resonance frequency for the Gilbert damping term. This may not be true if there are other non-linear mechanisms, like two-magnon scattering<sup>37</sup>. Besides, there is always an inevitable nonzero linewidth intercept at zero frequency in the measurement which may be due to inhomogeneous linewidth broadening. A modified semi-empirical equation is used for fitting:

$$\Delta H = \frac{2\alpha}{|\gamma| \cos(\theta - \theta_e)} f_{FMR} + \Delta H_0 \quad (3.43)$$

$\Delta H_0$  reflects the inhomogeneous linewidth broadening of the thin film sample. The physical meaning of the cosine denominator is the apparent broadening of the linewidth due to angle deviation (misalignment) of the oblique external magnetic field from the magnetization direction. In conventional FMR measurements, magnetic field modulation and lock-in detection are usually

introduced to increase signal-to-noise ratios (SNR). In this case the measured signal may be a derivative of the microwave power absorption. Fig. 4.10(a) shows an example of an experimental FMR profile for a YIG sample. The line shows the fit to a derivative of Lorentzian trial function. The linewidth acquired is the peak-to-peak linewidth which has the form

$$\Delta H_{pp} = \frac{2\alpha}{\sqrt{3}|\gamma|\cos(\theta - \theta_e)} f_{FMR} + \Delta H_0 \quad (3.44)$$

For the case where the field is either perpendicular or parallel to the film plane, one has  $\theta = \theta_e$  and Eq. (3.44) becomes

$$\Delta H_{pp} = \frac{2\alpha}{\sqrt{3}|\gamma|} f_{FMR} + \Delta H_0 \quad (3.45)$$

Equation (3.45) is one of the main results that is used in the following chapters. Note that  $\alpha$  is an effective damping parameter which is only valid for the Gilbert model. The damping mechanisms in magnetic materials are too complicated to describe with a single term.

### 3.5 Summary

Chapter 3 presents conceptual and quantitative discussions of dispersion relations for both spin wave modes as well as (quasi-) uniform resonance modes. The damping mechanism under the Gilbert model for the uniform resonance mode is discussed in details where the linewidth broadening has a linear dependence on the microwave frequency. Equations (3.32) and (3.45) are the two main results that are applied for FMR data analyses in the following chapters.

# CHAPTER 4

## DEVELOPING YIG NANO FILMS BY SPUTTERING TECHNIQUES

As mentioned in the beginning of this dissertation, recent years witnessed a considerable interest in using yttrium iron garnet ( $\text{Y}_3\text{Fe}_5\text{O}_{12}$ , YIG) for spintronics.<sup>1-8,19,55,57</sup> This interest was due to the extremely small magnetization damping property of YIG. Specifically, the intrinsic Gilbert damping constant in YIG materials is  $\alpha_0 \approx 3 \times 10^{-5}$ ,<sup>37</sup> which is two orders of magnitude smaller than that in ferromagnetic metals<sup>58,59</sup> and one order of magnitude smaller than that in hexagonal ferrites.<sup>39</sup> In addition, YIG materials are also electrically insulating, which is particularly attractive since insulator-based spintronic devices not only require substantially lower power compared to conductor-based devices, but also do not have issues intrinsically associated with charge currents.

The development of YIG-based spintronics demands YIG thin films that have a thickness in the nanometer range and at the same time exhibit low damping. In spite of considerable work on the growth of micron-<sup>60,61</sup> and submicron-thick YIG films,<sup>62,63,64,65,66,67,68,69,70</sup> there has been a

---

<sup>57</sup> V. Castel, N. Vlietstra, J. B. Youssef, and B. J. van Wees, *Appl. Phys. Lett.* **101**, 132414 (2012).

<sup>58</sup> Z. Celinski and B. Heinrich, *J. Appl. Phys.* **70**, 5935 (1991).

<sup>59</sup> S. S. Kalarickal, P. Krivosik, M. Wu, and C. E. Patton, *J. Appl. Phys.* **99**, 093909 (2006).

<sup>60</sup> R. C. LeCraw, E. G. Spencer, C. S. Porter, *Phys. Review*, **110**, 1311 (1958).

<sup>61</sup> R. C. Linares, R. B. McGraw, and J. B. Schroeder, *J. Appl. Phys.* **36**, 2884 (1965).

<sup>62</sup> P. C. Dorsey, S. E. Bushnell, R. G. Seed, and C. Vittoria, *J. Appl. Phys.* **74**, 1242 (1993).

<sup>63</sup> M.-B. Park, B. J. Kim, and N.-H. Cho, *IEEE Trans. Magn.* **35**, 3049 (1999).

<sup>64</sup> T. Boudiar, S. Capraro, T. Rouiller, M.-F. Blanc-Mignon, B. Payet-Gervy, M. Le Berre, and J.-J. Rousseau, *Phys. Stat. Sol. (C)* **1**, 3347 (2004).

trend to grow nanometer-thick YIG films in the last two decades.<sup>10,71,72</sup> Particularly in Ref. [10], nanometer-thick YIG films deposited by pulsed laser deposition (PLD) techniques with significantly smaller linewidths were reported. In this chapter the development of radio frequency (RF) sputtered YIG nano films on gadolinium gallium garnet ( $\text{Gd}_3\text{Ga}_5\text{O}_{12}$ , GGG) substrates and their properties are presented. Compared with the PLD growth, the sputtering growth of YIG films has several advantages as follows. (i) The sputtered films are more uniform than the PLD films. (ii) Sputtering growth is much faster than the PLD. (iii) Sputtering is more widely used in industry than the PLD.

## 4.1 Optimization of fabrication parameters for uniform YIG nano films

In contrast to considerable previous work on the growth of micron- or submicron-thick YIG films and nanometer-thick YIG films by PLD, little work has been carried out on the growth of nm-thick YIG films using magnetron sputtering techniques. The optimized fabrication parameters and experience from the PLD<sup>10</sup> are introduced as a quick startup for YIG film development. Therefore, a brief discussion of PLD techniques is necessary to find initial fabrication parameters.

---

<sup>65</sup> S. Yamamoto, H. Kuniki, H. Kurisu, M. Matsuura, and P. Jang, *Phys. Stat. Sol. (A)* **201**, 1810 (2004).

<sup>66</sup> S. -Y. Sung, X. Qi, and B. J. H. Stadler, *Appl. Phys. Lett.* **87**, 121111 (2005).

<sup>67</sup> Y.-M. Kang, S.-H. Wee, S.-I. Baik, S.-G. Min, S.-C. Yu, S.-H. Moon, Y.-W. Kim, and S.-I. Yoo, *J. Appl. Phys.* **97**, 10A319 (2005).

<sup>68</sup> S. A. Manuilov, R. Fors, S. I. Khartsev, and A. M. Grishin, *J. Appl. Phys.* **105**, 033917 (2009).

<sup>69</sup> Y. Krockenberger, K.-S. Yun, T. Hatano, S. Arisawa, M. Kawasaki, and Y. Tokura, *J. Appl. Phys.* **106**, 123911 (2009).

<sup>70</sup> S. A. Manuilov and A. M. Grishin, *J. Appl. Phys.* **108**, 013902 (2010).

<sup>71</sup> N. Kumar, D. S. Misra, N. Venkataramani, S. Prasad, and R. Krishnan, *J. Magn. Magn. Mater.* **272-276**, e899 (2004).

<sup>72</sup> E. Popova, N. Keller, F. Gendron, M. Guyot, M. -C. Brianso, Y. Dumond, and M. Tessier, *J. Appl. Phys.* **90**, 1422 (2001).

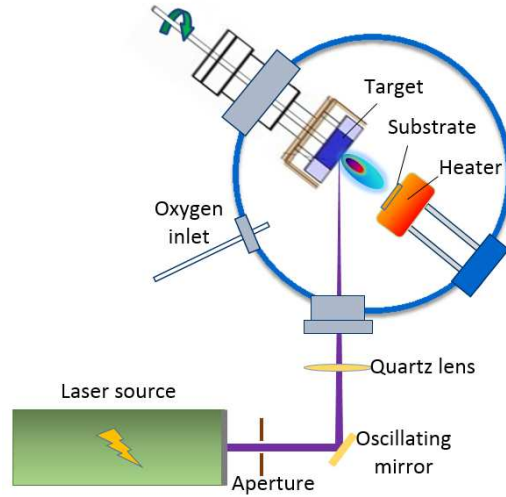


Figure 4.1. The schematic of a typical PLD system.

Figure 4.1 shows the schematic of a typical PLD system. High-power laser pulses are guided into a vacuum chamber by a set of optical apertures. The target material is then ablated by the laser beam and is evaporated onto substrates. The substrates can be heated for a designated deposition temperature or for a post-annealing process. For oxides and ceramic materials, the inlet allows O<sub>2</sub> gas into the chamber for oxygen compensation.

Table 4.1. Optimized parameters for fabricating YIG thin films with PLD techniques

<b>Deposition</b>	Target-substrate distance	6.0 cm
	Substrate temperature	850 °C
	O <sub>2</sub> pressure	0.1 Torr
	Laser energy fluence	1.7 J/cm <sup>2</sup>
	Laser pulse repetition	1 Hz
	Laser pulse duration	30 ns
<b>Annealing</b>	O <sub>2</sub> pressure	100 Torr
	Annealing temperature	850 °C
	Annealing time	10 min
	Cooling rate	2 °C/min

Table 4.1 presents the optimized parameters for fabricating YIG nanometer-thick films by PLD techniques. Three main ideas from the concept of PLD fabrication of YIG films are: (i) the deposition process is at high temperature for better crystallization; (ii) High gas pressure is sustained during the deposition process; (iii) in-situ post annealing process with oxygen gas guarantees the crystallization process and compensates the oxygen element in the YIG. Based on the main concepts, a set of trial fabrication parameters are developed and applied for YIG deposition by sputtering techniques. Table 4.2 presents the trial parameters.

Table 4.2. A set of trial fabrication parameters for sputtering techniques.

<b>Sputtering</b>	Target to substrate	6.8 cm
	Substrate temperature	750 °C
	Ar pressure	10 mTorr
	Ar flow rate	16 sccm
	Sputtering power	75 W
<b>Annealing</b>	O <sub>2</sub> pressure	1.12 Torr
	Annealing temperature	800 °C
	Annealing time	4 hr
	Cooling rate	1 °C/min

The sputtering deposition used a 2-in. YIG target, 0.5-mm-thick (111) GGG substrates, and high-purity argon (99.9997%), and was followed by an in-situ annealing process. The films were prepared with the following parameters. (1) The target-to-substrate distance was 6.8 cm. (2) Prior to sputtering, the vacuum chamber had a base pressure of  $1.0 \times 10^{-8}$  Torr. (3) The sputtering was at high temperature (800 °C). (4) During the sputtering and deposition process, the argon pressure was 10 mTorr and the flow rate was 16 sccm (standard cubic centimeter per minute at 0 °C). (5) The annealing is in situ with a temperature of 800 °C and an oxygen pressure of ~ 1 Torr.

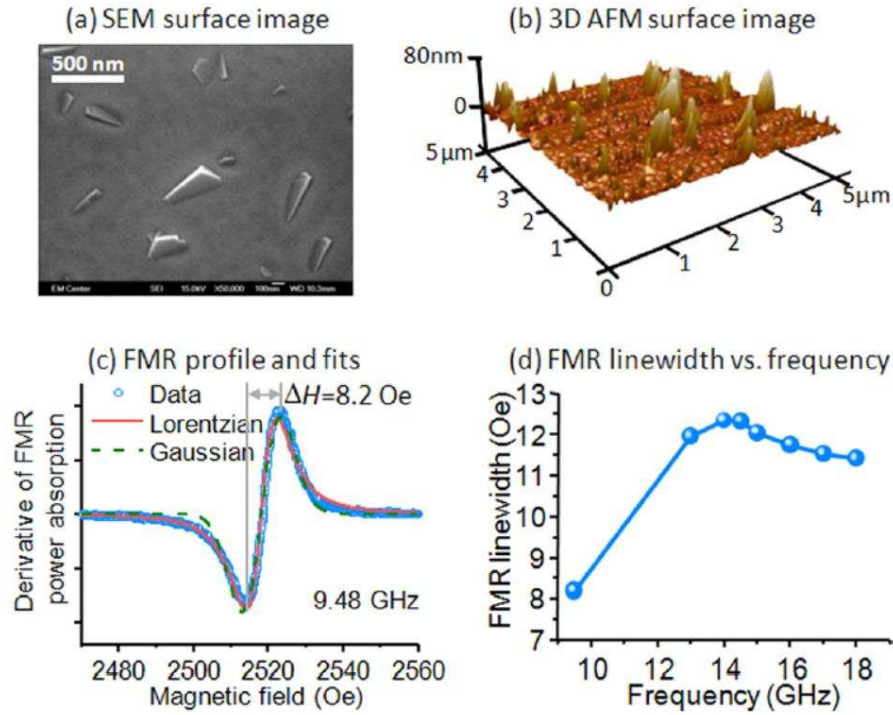


Figure 4.2. Properties of a 10-nm-thick YIG film with big grains. Graphs (a) and (b) give the SEM and AFM surface images, respectively. Graph (c) presents an FMR profile and two fits. Graph (d) gives  $\Delta H_{pp}$  as a function of  $f$ .

Figure 4.2 presents the data for a 10-nm-thick YIG film which was prepared by sputtering with the parameters and processes shown in Table 4.2. The images of Figs. 4.2(a) and 4.2(b) indicate that the surface has a smooth background surface but contains some big grains in a 100-400 nm lateral size range and a height above 80 nm. Figure 4.2(c) shows the FMR profile taken at 9.47 GHz. Two fitting trial functions are used – Lorentzian and Gaussian functions as indicated in the legend. The linewidth is on the same order of magnitude with that in the YIG sample made by PLD techniques.<sup>10</sup> Besides, the Lorentzian fit is a little better than the Gaussian fit, which may indicate long-range homogeneity of the film. Figure 4.2(d) gives the peak-to-peak FMR linewidth  $\Delta H_{pp}$  vs. microwave frequency  $f$  response. This response is strongly nonlinear, in stark contrast to the linear responses predicted by Eq. (3.45). Such a nonlinear frequency

dependence is usually an indication of two-magnon scattering (TMS).<sup>37, 73, 74, 75, 76</sup> It is conceivable that big grain-associated TMS occurs in the film. The nonlinear frequency dependence of the TMS is mainly due to the field dependence of the density of degenerate spin waves.

Though an apparent decent linewidth is acquired at 9.48 GHz, the YIG film is not uniform, as indicated by the SEM and AFM images. Similar surfaces have been observed in films made by using a wide range of deposition temperatures, as shown in Fig. 4.3.

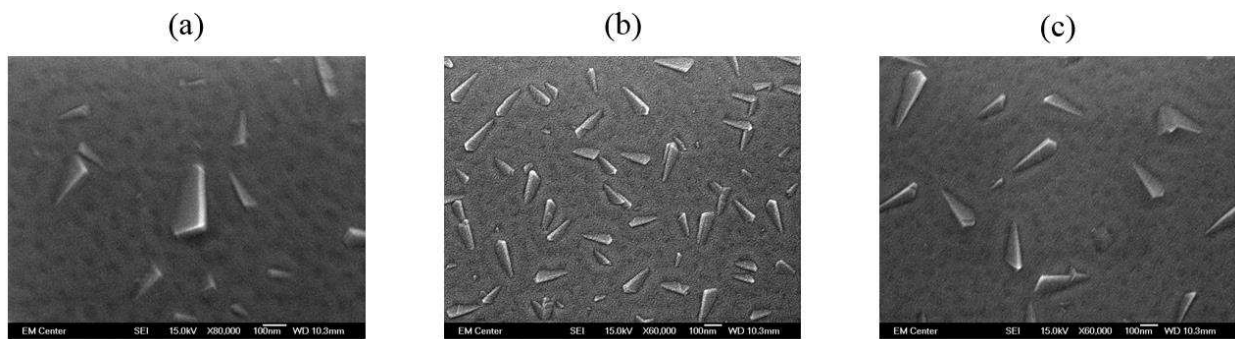


Figure 4.3. SEM images of nanometer-thick YIG films grown by sputtering and annealed at 750 °C. The argon pressure is 10 mTorr and the flow rate is 16 sccm. The deposition temperatures are (a) 550 °C, (b) 650 °C, and (c) 750 °C.

The shape of the grains indicates excessive crystallization in the YIG. The failure of getting uniform films indicates that the physical process of deposition of sputtering techniques is different from PLD techniques. The main attribute of the PLD technique is layer-by-layer deposition. Target materials will be ablated by pulsed laser with a slow repetition rate ( $< 50$  Hz) and evaporated onto the substrates. With a laser pulse repetition rate of  $\sim 1$  Hz, material molecules will diffuse at a high temperature and move uniformly in microseconds before the next input pulse. On the contrary, sputtering is a continuous growth method. Under a high

<sup>73</sup> R. Arias and D. L. Mills, Phys. Rev. B **60**, 7395 (1999).

<sup>74</sup> R. D. McMichael and P. Krivosik, IEEE Trans. Magn. **40**, 2 (2004).

<sup>75</sup> K. Lenz, H. Wende, W. Huch, K. Baberschke, K. Nagy, and A. Janossy, Phys. Rev. B **73**, 144424 (2006).

<sup>76</sup> S. S. Kalarickal, P. Krivosik, J. Das, K. S. Kim, and C. E. Patton, Phys. Rev. B **77**, 054427 (2008).

temperature, atoms from the target will diffuse insufficiently. Atoms will pile up in local clusters due to this incomplete diffusion and be distributed and crystallized non-uniformly, forming the grains with sharp edges. From this analysis, two arguments can be inferred: (1) extension of deposition time will lead to the development of the excessive crystallized clusters into granular films, and (2) the grains may be eliminated if the clustering effect is suppressed so that atoms are distributed uniformly. This can be achieved by sputtering at lower temperatures to suppress the diffusion of attached atoms.

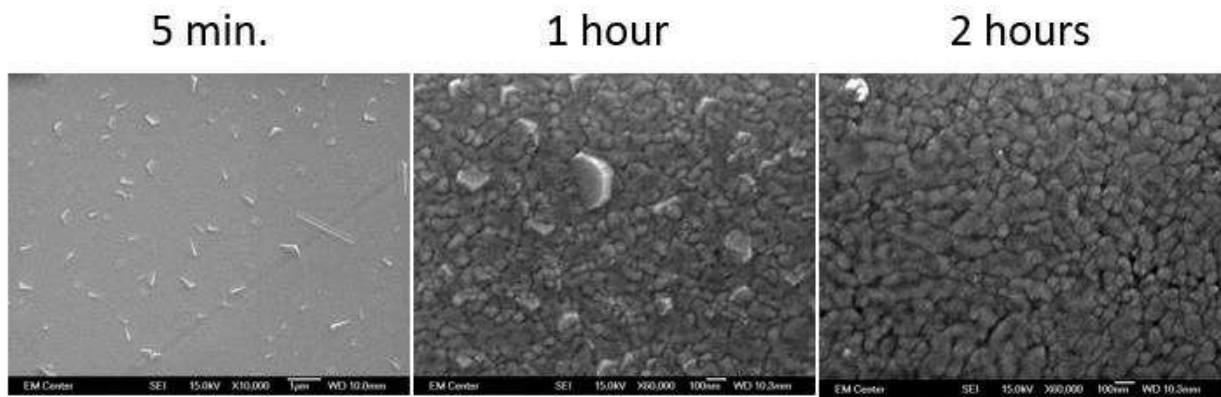


Figure 4.4. SEM images of YIG thin films grown using different deposition times. The fabrication parameters are the same as those in Table 4.2. The thicknesses are 8.92 nm, 107 nm, and 215 nm for the films using 5 min., 1 hr, and 2 hr deposition times, respectively.

Figure 4.4 presents the surface morphology of YIG thin films grown using different deposition times, as indicated. The images are measured by scanning electron microscopy (SEM). One can see clearly that as the deposition time is extended, the thin film develops into a granular film and some clusters are piled up forming localized excessive crystallized grains. This result proves the first argument. Besides, the thicknesses of the films deposited with 5 min, 1 hr, and 2 hr periods are 8.92 nm, 107 nm, and 215 nm, respectively, showing an unchanged deposition rate for time periods no longer than 2 hr.

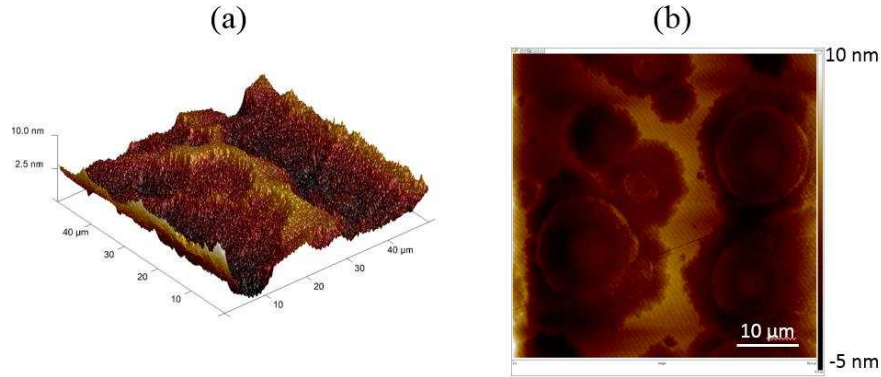


Figure 4.5. The surface images of a 20-nm-thick YIG thin film measured by AFM. The fabrication parameters are the same as those in Table. 4.2 except that it was deposited at room temperature. (a) 3D image and (b) 2D surface image.

The second argument is checked by depositing YIG films at room temperature. Figure 4.5 presents the surface images of a YIG thin film deposited at room temperature. One can see that the surface shown in Fig. 4.5(a) is smoother than that shown in Fig. 4.2(b). The surface morphology pattern shown in Fig. 4.5(b) is very different from that shown in Fig. 4.2(a), indicating that the excessive crystallization is suppressed. This is consistent with the previous analysis. However, the surface is still not uniform or smooth.

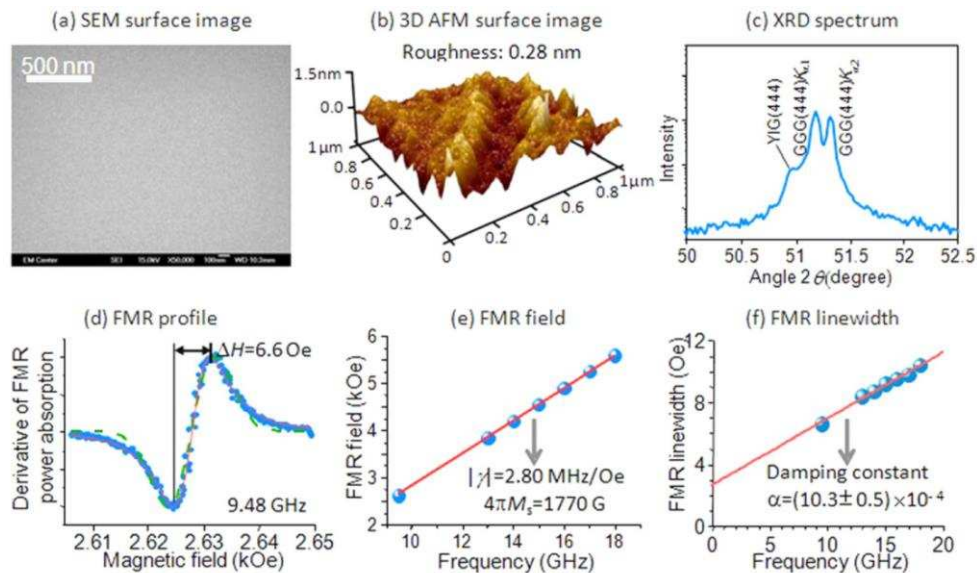


Figure 4.6. Properties of a 10.2-nm-thick YIG film. Graphs (a), (b), and (c) show the SEM, AFM, and XRD data, respectively. Graphs (d)-(f) present FMR properties, with the points showing experimental data and the curves showing numerical fits.

This problem is solved by decreasing the argon gas flow rate, as shown by the data in Fig. 4.6. The YIG thin film is deposited at room temperature and the argon flow rate is 4 sccm. The other fabrication parameters are the same as those in Table 4.2. Figures 4.6(a) and 4.6(b) give a SEM surface image and a 3D AFM surface image, respectively. The data indicate a very smooth and uniform surface with a roughness of  $0.28 \pm 0.03$  nm. Figure 4.6(c) presents an XRD spectrum, which shows that the YIG film has a (111) orientation. Figure 4.6(d) gives an FMR profile measured at 9.48 GHz using an X-band rectangular cavity, while Figs. 4.6(e) and 4.6(f) give the FMR field ( $H_{\text{FMR}}$ ) and the peak-to-peak linewidth ( $\Delta H_{\text{pp}}$ ), respectively, as a function of frequency  $f$  measured using a Ku-band rectangular shorted waveguide. In all the graphs, the points show the experimental data, and the curves show the fits. In Fig. 4.6(d), the solid and dashed curves show the fits to the derivatives of a Lorentzian function and a Gaussian function, respectively. In Fig. 4.6(e), the curve shows a fit to the Kittel equation Eq. (3.32b)). The fitting yields  $4\pi M_{\text{eff}} = 1770$  G and  $|\gamma| = 2.80$  MHz/Oe . The line in Fig. 4.6(f) shows a linear fit to Eq. (3.45). The fitting yields  $\alpha = (10.3 \pm 0.5) \times 10^{-4}$ .

Several points should be mentioned regarding the data shown in Fig. 4.6. (1) The  $|\gamma|$  value exactly equals the standard value. (2) The  $4\pi M_{\text{eff}}$  value falls into the range reported for YIG bulk materials which is 1730 – 1780 Oe.<sup>34</sup> Later it will be shown that the uniaxial anisotropy of such YIG thin films are very small at room temperature so that the effective magnetization is very close to the saturation magnetization value. (3) The film has a linewidth comparable to the values of PLD YIG films.<sup>10</sup> (4) The damping of the film is about 3 times larger than that of the PLD film<sup>10</sup> but is significantly smaller than that of metallic films of similar thicknesses.<sup>58,59</sup> (5) The film is homogeneous as indicated by the following two facts: (i) The Lorentzian function fits the FMR profile much better than the Gaussian function as shown in Fig. 4.6(d) and (ii) the

linear fit in Fig. 4.6(f) yields a small  $\Delta H_0$  value ( $< 3$  Oe). These results together indicate the high quality of the film and thereby demonstrate the feasibility of the sputtering growth of YIG nano films. The mechanism of the relation between such surface morphology and the argon gas flow rate is still unknown and further study is needed in the future. One of the reasons might be that plasma will be distributed more homogeneously with a lower flow rate. Then the distribution of kinetic energy of incident particles is spatially uniform.

## 4.2 Dependence of YIG film properties on sputtering processes

In this section, the dependence of YIG thin film properties on some fabrication parameters are discussed in details to elaborate the physical process of sputtering techniques.

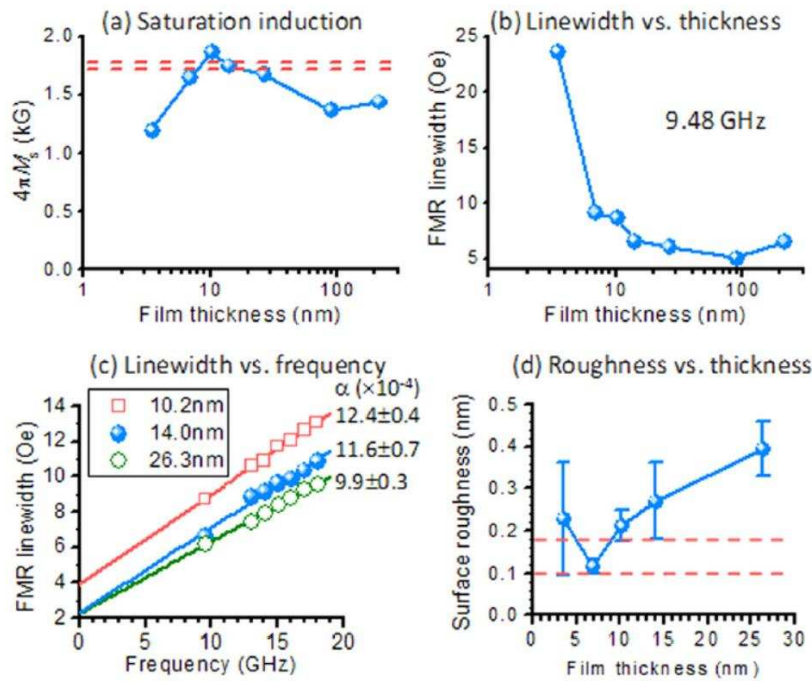


Figure 4.7. Graphs (a) and (b) give the  $4\pi M_{\text{eff}}$  and  $\Delta H_{\text{pp}}$  values, respectively, as a function of film thickness. Graph (c) gives the  $\Delta H_{\text{pp}}$  vs.  $f$  responses for three films, as indicated. Graph (d) gives the roughness as a function of film thickness.

Figure 4.7 shows how the film properties vary with the film thickness  $d$ , after annealing at 750 °C. The fabrication parameters are shown in Table. 4.3 which are optimized as discussed in

Section 4.1. Figure 4.7(a) gives  $4\pi M_{\text{eff}}$  as a function of  $d$ . The  $4\pi M_{\text{eff}}$  values were obtained by fitting the  $H_{\text{FMR}}$  vs.  $f$  responses with Eq. (3.32(b)), using  $|\gamma|=2.80$  MHz/Oe. The dashed lines indicate the  $4\pi M_S$  range expected for YIG bulk materials.<sup>34</sup> Figure 4.7(b) shows  $\Delta H_{\text{pp}}$  as a function of  $d$  obtained from FMR measurements at 9.48 GHz. In Fig. 4.7(c), the symbols present the  $\Delta H_{\text{pp}}$  vs.  $f$  responses for three films while the lines show fits to Eq. (3.45). The fitting-yielded  $\alpha$  values are also indicated in the graph. Figure 4.7(d) presents the surface roughness as a function of  $d$ . The dashed lines indicate the roughness range of the GGG substrate, which is  $0.14 \pm 0.04$  nm.

Table 4.3. Optimized fabrication parameters for sputtering YIG films at room temperature and smaller Ar flow rates.

<b>Sputtering</b>	Target to substrate	6.8 cm
	Substrate temperature	23 °C
	Ar pressure	10 mTorr
	Ar flow rate	4 sccm
	Sputtering power	75 W
<b>Annealing</b>	O <sub>2</sub> pressure	1.12 Torr
	Annealing temperature	750 °C
	Annealing time	4 hr
	Cooling rate	1 °C/min

Four important results are evident from the data in Fig. 4.7. (1) For films in the 7 – 26 nm thickness range, the  $4\pi M_S$  values are close to those expected for YIG bulk materials, the  $\Delta H_{\text{pp}}$  values are all smaller than 10 Oe, and the roughness values are in the 0.1 – 0.4 nm range and are close to the roughness of the GGG substrate. These results together indicate that the films in the 7 – 26 nm range have high quality. (2) The 7 – 26 nm films also show an increase in  $\Delta H_{\text{pp}}$  when

the film thickness is reduced, as shown in Fig. 4.7(b). The film surface imperfections can enhance ferromagnetic relaxation (such as magnon-phonon scattering, two-magnon scattering, or charge transfer relaxation) at the film surface. This surface-associated damping contributes to the overall damping of the YIG film and plays stronger roles as  $d$  is reduced. This interpretation is supported by the increase of  $\alpha$  with a decrease in  $d$  shown in Fig. 4.7(c). (3) The 3.5-nm-thick film shows a much lower  $4\pi M_{\text{ff}}$  and a much larger  $\Delta H_{\text{pp}}$  than the 7 – 26 nm films. This might indicate that such optimized sputtering and annealing control parameters given above are not appropriate to the growth of ultrathin YIG films. (4) The 89-nm-thick and 214-nm-thick films show relatively low  $4\pi M_{\text{eff}}$  values, as shown in Fig. 4.7(a). Although not shown, the films also show some small pin holes on the surfaces. These results indicate that the above-described processes might also be inappropriate for the growth of relatively thick films. Nevertheless, the 89-nm and 214-nm films both show a  $\Delta H_{\text{pp}}$  value of less than 7 Oe. In addition, if one compares the data presented by squares in Fig. 4.7(c) to the data shown in Fig. 4.6(f), one can see that the film annealed at 800 °C shows not only a smaller  $\Delta H_0$  but also a smaller  $\alpha$  than the film annealed at 750 °C. This indicates that annealing at 800 °C is more preferable than annealing at 750 °C.

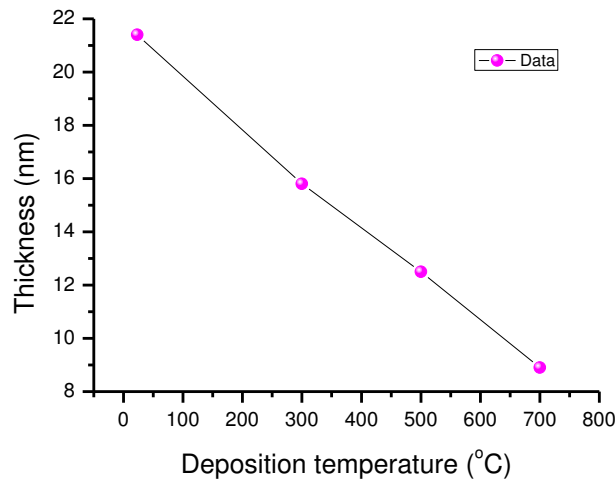


Figure 4.8. Thickness vs. deposition temperature for a deposition time period of 5 min. All other parameters are the same as those in Table 4.3.

Figure 4.8 presents the thickness vs. deposition temperature data. As the deposition temperature increases, the film thickness decreases. For higher temperatures, the kinetic energy of gas atoms and ions in the plasma is higher, which results in more frequent collisions with target atoms and deters the deposition process.

Table 4.4. Fabrication parameters for sputtering YIG films with varied argon gas pressures.

<b>Sputtering</b>	Target to substrate	6.8 cm
	Substrate temperature	23 °C
	Ar pressure	10 - 40 mTorr
	Ar flow	4 sccm
	Sputtering power	75 W
	Sputtering time	30 min
<b>Annealing</b>	O <sub>2</sub> pressure	1.12 Torr
	Annealing temperature	750 °C
	Annealing time	4 hr
	Cooling rate	1 °C/min

Another fabrication parameter discussed is the argon pressure during the deposition. Table 4.4 shows the fabrication parameters. The optimized annealing temperature 800 °C is used. All parameters including the sputtering time are fixed except for the argon pressure. Table 4.5 presents the data of five YIG thin films prepared at different argon pressures.

Table 4.5. Effects of the Ar pressure in sputtering on the properties of YIG thin films.

Ar pressure (mTorr)	Film thickness (nm)	Surface roughness (nm)	$4\pi M_s$ (G)	$\alpha (\times 10^{-5})$
10	39.7	0.10±0.01	1550	20.3±3.2
20	23.4	0.09±0.01	1720	12.5±0.4
25	22.3	0.13±0.05	1770	8.58±0.21
30	19.7	0.10±0.01	1790	28.1±0.5
40	19.5	0.23±0.02	1720	30.7±2.3

Several results are evident from the data in Table 4.5. (1) When the deposition time is the same, the film thickness decreases with an increase in the argon pressure. Such a change is strong particularly for relatively low argon pressures. For higher argon pressure, collisions between target atoms and gas atoms/ions are more frequent, leading to a decrease of the kinetic energy of incident particles as well as a slow deposition processes. (2) Except for the thickest film, all the films show a very small surface roughness, which is only 0.1 nm. (3) Except for the thinnest film, all the films show a saturation induction very close to the value for YIG bulk materials. For the thinnest film, as the argon pressure is low, collisions between gas atoms/ions and target atoms are less frequent, which may lead to the transfer of excessive kinetic energies of incident atoms to the substrates. As analyzed in Section 2.2, when the argon pressure is decreased, it makes the kinetic energy of incident particles increase by decreasing collision probability. In this situation, the deposition rate is increased. But the quality of the YIG thin film may become low because the thin film as well as the surface atoms of the substrate might be punched and/or dissociated by incident particles with such excessive energy. A further decrease in the argon pressure ( $\sim 5$  mTorr) will lead to etching and dissociation phenomena with incident particles of a kinetic energy higher than the critical one. Materials of the target can barely be deposited. (4) The Gilbert damping constant vs. argon pressure response shows an overall dip behavior and indicates the existence of an optimal argon pressure which is about 25 mTorr. This agrees with the discussed observations. The film obtained at the lowest Ar pressure has a saturation induction largely different from the bulk value. The film obtained at the highest Ar pressure has a relatively large surface roughness. Besides, the films obtained at mediate argon pressures have a saturation induction much closer to the bulk value and are also smoother. (5) The films deposited at 20, 25, 30, and 40 mTorr have slightly different thicknesses but very

different  $\alpha$  values. This indicates that the argon pressure-caused thickness change is not the dominant reason for the  $\alpha$  change shown in Table 4.5. Rather, it is the change of the film microstructure properties with the argon pressure that is responsible for the  $\alpha$  change. These results show the critical role of the argon pressure in the sputtering growth of YIG thin films.

### 4.3 High-quality YIG nano films developed by sputtering techniques

This section reports on the results of sputtering growth of high-quality YIG films with a damping substantially smaller than that in previously sputtered films.

Table 4.6. The optimized fabrication parameters for the 22.3-nm-thick YIG film.

<b>Sputtering</b>	Target to substrate	6.8 cm
	Substrate temperature	23 °C
	Ar pressure	25 mTorr
	Ar flow	4 sccm
	Sputtering power	75 W
	Sputtering time	30 min
<b>Annealing</b>	O <sub>2</sub> pressure	1.12 Torr
	Annealing temperature	800 °C
	Annealing time	4 hr
	Cooling rate	1 °C/min

Table 4.6 gives the fabrication parameters optimized through the work described in Sections 4.1 and 4.2. As discussed previously, room temperature deposition, a smaller argon flow rate, a moderate argon pressure, and high annealing temperature are critical for high-quality YIG film development, all reflected in Table 4.6.

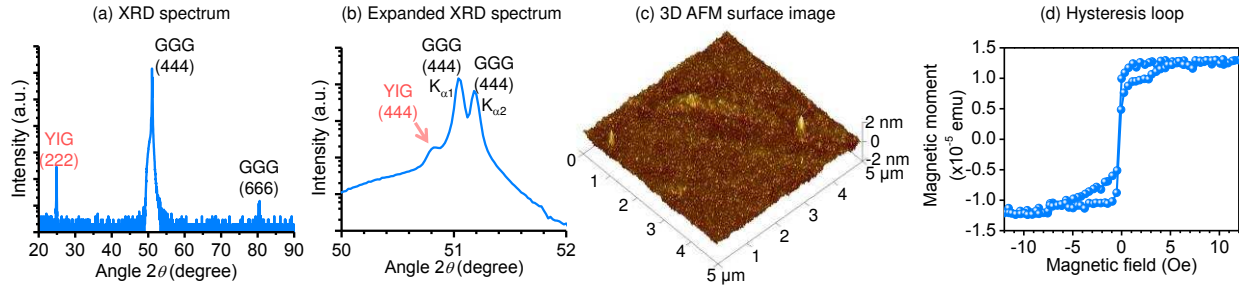


Figure 4.9. Properties of the 22.3-nm-thick YIG film fabricated by sputtering. (a) shows an XRD spectrum, and (b) shows the same spectrum in an expanded angle scale. (c) presents an AFM surface image. (d) gives a hysteresis loop measured with an in-plane magnetic field by a superconducting quantum interference device (SQUID).

Figure 4.9 presents the XRD, AFM, and SQUID data of a YIG film prepared at an argon pressure of 25 mTorr and other control parameters listed in Table 4.6. The film has a thickness of 22.3 nm, which was determined via the XRR analysis. Figure 4.9(a) shows an XRD spectrum of the film, while Fig. 4.9(b) shows the same spectrum in an expanded angle scale. The data confirm the existence of the YIG phase in the sample and also indicate the (111) orientation of the film. The data show no evidences for the existence of any additional phases. Figure 4.9(c) gives an AFM surface image of the film, which indicates that the film surface is uniform and smooth. Additional AFM data indicate that the film has an rms surface roughness of  $0.13 \pm 0.05$  nm. Figure 4.9(d) shows the SQUID data measured with a magnetic field applied in the film plane. The data indicate a very small coercivity, which is 0.42 Oe. The data also indicate  $4\pi M_{\text{eff}} = 1795 \pm 18$  G, which is only 2.5% larger than the value for bulk YIG crystals (1750 G). The above results together clearly indicate that the film has high quality and may thereby show a low damping constant. The damping properties of the film are presented below.

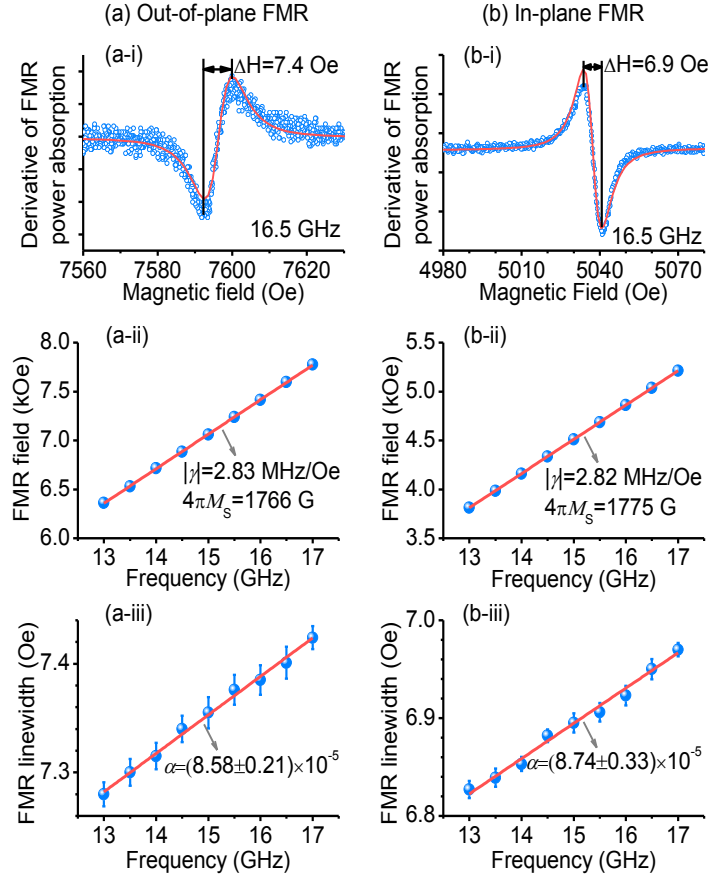


Figure 4.10. FMR data obtained with the same YIG film cited in Fig. 4.9. The left and right columns show the FMR data measured with a static magnetic field applied perpendicular to and in the plane of the YIG film, respectively.

Figure 4.10 presents the FMR data obtained with the same film discussed above. The graphs on the left show the FMR data obtained with an out-of-plane magnetic field. In Fig. 4.10(a-i), the circles give an FMR profile measured at 16.5 GHz, while the curve shows a fit to the derivative of a Lorentzian trial function. The fitting yielded  $\Delta H_{pp} = 7.40 \pm 0.01$  Oe, as indicated. The fitting also yielded the FMR field ( $H_{FMR}$ ), although it is not indicated in the graph. Similar fitting was carried out to other FMR profiles, and such fitting yielded all the  $H_{FMR}$  and  $\Delta H_{pp}$  data presented in this section. In Fig. 4.10(a-ii), the dots present the FMR fields at different frequencies  $f$ , while the line shows a fit to Eq. 3.32(a). One can see that the fitting is almost perfect. The fitting gave  $|\gamma| = 2.83 \pm 0.01$  MHz/Oe and  $4\pi M_{eff} = 1766 \pm 16$  G, whose rationalizations are provided below.

Figure 4.10(a-iii) presents  $\Delta H_{pp}$  as a function of  $f$ . The dots show the data, while the line shows a linear fit to Eq. 3.45. The fitting gave  $\alpha = (8.58 \pm 0.21) \times 10^{-5}$  and  $\Delta H_0 = 6.80 \pm 0.01$  Oe.

The above-described FMR study gave three important parameters of the YIG film:  $|\gamma|$ ,  $4\pi M_{\text{eff}}$ , and  $\alpha$ . To confirm these parameters, FMR measurements were also carried out for the field-in-plane configuration. The main data are presented in the right column of Fig. 4.10, in the exactly same format as in the left column. The curve in Fig. 4.10(b-ii) is a fit to Eq. (3.32(b)). One sees an almost perfect fitting, as in Fig. 4.10(a-ii). The fitting gave  $|\gamma| = 2.817 \pm 0.001$  MHz/Oe and  $4\pi M_{\text{eff}} = 1775 \pm 8$  G. These values agree very well with those obtained for the out-of-plane configuration, with the differences less than 1%. The line in Fig. 4.10(b-iii) is a linear fit to Eq. 3.45. The fitting yielded  $\alpha = (8.74 \pm 0.33) \times 10^{-5}$  and  $\Delta H_0 = 6.35 \pm 0.02$  Oe. This  $\alpha$  value is very close to and thereby confirms the damping constant obtained from the out-of-plane FMR study. Note that the fits shown in Fig. 4.10(a-ii), (a-iii), (b-ii), and (b-iii) are all least squares fits.

Three important points should be emphasized. First,  $\alpha = (8.58 \pm 0.21) \times 10^{-5}$ , which was obtained for the out-of-plane configuration, is about 10 times smaller than the damping constant of previously sputtered YIG films<sup>11</sup> and is about 3 times smaller than that of PLD YIG films reported previously.<sup>10,77</sup> Second, the  $\alpha$  value for the in-plane configuration is slightly larger, which is most likely due to two-magnon scattering (TMS). The difference, however, is very small (less than 2%), which indicates that the TMS process in the film is very weak at least at room temperature. Note that the TMS process is allowed in a magnetic film when it is magnetized with an in-plane magnetic field but is prohibited when the magnetic field is

---

<sup>77</sup> O. d'Allivy Kelly, A. Anane, R. Bernard, J. Ben Youssef, C. Hahn, A.H. Molpeceres, C. Carrétéro, E. Jacquet, C. Deranlot, P. Bortolotti, R. Lebourgeois, J. -C. Mage, G. de Loubens, O. Klein, V. Cros, and A. Fert, *Appl. Phys. Lett.* **103**, 082408 (2013).

out-of-plane.<sup>74,78</sup> Finally,  $|\gamma| = 2.83 \pm 0.01$  MHz/Oe is very close to the standard value; and  $4\pi M_{\text{eff}} = 1766 \pm 16$  G agrees almost perfectly with the value for YIG bulk materials. In brief, it is evident from the data in Figs. 4.9 and 4.10 that the film has high quality in terms of both structural, static magnetic, and high-frequency magnetic properties. Note that, although the in-plane FMR yielded  $4\pi M_{\text{eff}}$  value is close to the out-of-plane yielded value, the  $4\pi M_S$  value obtained with the SQUID measurements is a little large (about 1.6%). Possible reasons for this are the error of the film thickness or surface area measurement and the existence of a small uniaxial anisotropy field.

## 4.4 Summary

The work in this chapter demonstrates the sputtering growth of high-quality YIG nano films and reveals their FMR properties, including details on the optimization of the fabrication process. The films in the 7–26 nm thickness range showed a surface roughness of 0.1–0.4 nm, a standard gyromagnetic ratio, a saturation magnetization very close to the YIG bulk value, and an FMR linewidth comparable to values obtained in PLD films. Dependence of YIG film properties on sputtering processes is discussed from several aspects. The best film, which was deposited at the optimal argon pressure and is 22.3 nm thick, showed a surface roughness of  $0.13 \pm 0.05$  nm,  $|\gamma| = 2.83 \pm 0.01$  MHz/Oe,  $4\pi M_{\text{eff}} = 1766 \pm 16$  G, and  $\alpha = (8.58 \pm 0.21) \times 10^{-5}$ . The demonstration in this chapter is of great technological significance as sputtering is a widely applied PVD technique. It should also be emphasized that the low-damping nm-thick YIG films demonstrated make possible nano-patterning of YIG films and development of YIG-based devices.

---

<sup>78</sup> P. Krivosik, N. Mo, S. Kalarickal, and C. E. Patton, J. Appl. Phys. **101**, 083901 (2007).

# CHAPTER 5

## ROLE OF DAMPING IN SPIN SEEBECK EFFECT IN YTTRIUM IRON GARNET THIN FILMS

### 5.1 Introduction – the spin Seebeck effect and theoretical models

The spin Seebeck effect (SSE) refers to the generation of a spin voltage in a ferromagnet (FM) due to a temperature gradient. This spin voltage can produce a pure spin current into a normal metal (NM) that is in contact with the ferromagnet. The SSE was first discovered in ferromagnetic metals,<sup>14,15,16</sup> but not long after was also observed in magnetic insulators<sup>2,17-21</sup> and semiconductors.<sup>22,23</sup> The experiments usually utilize a FM/NM bi-layered hetero-structure with the magnetization in the FM layer saturated in-plane and often take a longitudinal configuration in which a temperature gradient is established across the thickness of the FM/NM structure.

Various theoretical models have been proposed to interpret the SSE,<sup>2,3,16,17,23-27</sup> although a complete understanding of the effect has not been realized yet. Among the early models, the one attracting slightly more interest is the so-called magnon-driven SSE model proposed in Ref. [3]. More recent models include those proposed in Refs. [24-27]. Although proposed separately, these recent models all involve magnon flows across the FM thickness and emphasize the bulk origin of the SSE. The bulk origin has been supported by SSE experiments using FM films of different thicknesses.<sup>25,27</sup> The four SSE models mentioned above all engage magnetic damping in the FM film as a critical ingredient of the SSE in very different ways, as summarized below.

The magnon-driven SSE model was developed on the basis of the stochastic Gilbert equation.<sup>3</sup> The essence of this model is that the magnon subsystem in an FM can become thermalized internally before it equilibrates with the phonon subsystem. As a result, the spatial distribution of the magnon temperature  $T_m$  in the FM deviates from that of the phonon temperature  $T_p$ , although the average of  $T_m$  may be the same as that of  $T_p$ . This temperature distribution difference can further result in a difference between  $T_m$  in the FM and the electron temperature  $T_e$  in a neighboring NM at the interface and a corresponding pure spin current in the NM. This model yields an analytical expression for the spin current pumped from the FM to the NM. The expression involves the damping constant  $\alpha$  in a rather complicated manner, but the general trend is that the spin current increases monotonically as  $\alpha$  decreases.

In the study of Hoffman *et al.*<sup>24</sup>, on the other hand, the origin of the SSE was analyzed using the stochastic Landau-Lifshitz theory. According to the model in Ref. [24], the magnons in the FM film establish a non-equilibrium steady state by coupling with phonons in the FM via bulk damping and with electrons in the neighboring NM via interfacial spin pumping. The analysis identified several characteristic length scales that governed the SSE strength, and for all of those scales the SSE coefficient depends on  $\alpha$ , though in different manners. In the case of a  $\text{Y}_3\text{Fe}_5\text{O}_{12}$  (YIG) film thinner than 100 nm, the model suggests that the SSE coefficient is proportional to  $\alpha$ , which is opposite to the above-mentioned expectation of the model in Ref. [3].

In contrast to Xiao *et al.*<sup>3</sup> and Hoffman *et al.*<sup>24</sup>, in the study of Rezende *et al.*,<sup>25</sup> the SSE phenomenon was studied through microscopic calculations using the Boltzmann equation of the magnons. In the model of Rezende *et al.*,<sup>25</sup> the temperature gradient leads to the generation of the magnons in the bulk of the FM, and the magnon spin current into the NM is needed to ensure the continuity of the spin flow at the FM/NM interface. Different from the models in Xiao *et al.*<sup>3</sup> and

Hoffman *et al.*<sup>24</sup>, this model assumes that the magnon and phonon systems in the FM share the same temperature as demonstrated in a slightly earlier experimental study.<sup>79</sup> As in Ref. [3], in Ref. [25] the analytical expression for the spin current also involves  $\alpha$  in a very complicated manner, but the main point of the model is that the spin current into the NM increases with a decrease in the magnon relaxation rate, while the latter increases with an increase in  $\alpha$ .

Lastly, in the studies of Ritzmann *et al.*<sup>26</sup> and Kehlberger *et al.*<sup>27</sup>, the SSE was examined by numerical simulations that took into account the linear dependence of the SSE strength on  $T_m - T_p$  in the FM near the interface<sup>3</sup> and considered the decay of  $T_m - T_p$  with a certain characteristic length scale from the interface into the bulk of the FM. The simulations show that in the presence of a spatial temperature step in the FM, a magnon flow can arise from the hot side to the cold side, and the length of the magnon propagation is inversely proportional to  $\alpha$ . Although no explicit analytical expression for the dependence of the spin current or the SSE coefficient on  $\alpha$  was given, the simulation results revealed an increase in the SSE strength with a decrease in  $\alpha$ .

Despite the above-discussed theoretical aspects, however, there have been no experiments on the actual effects of the damping on the SSE so far, to the best of our knowledge. There was an experimental investigation on the SSE that used a large number of diverse garnet ferrites exhibiting different damping properties.<sup>80</sup> However, those materials did not allow for the study of the roles of  $\alpha$  in the SSE because they had significantly different static magnetic properties.

This chapter reports on the role of the damping on the SSE in  $Y_3Fe_5O_{12}$  (YIG) thin films. The experiments used YIG films grown on  $Gd_3Ga_5O_{12}$  (GGG) substrates by sputtering.<sup>11,12</sup> The films showed very similar structural and static magnetic properties but rather different  $\alpha$  values,

---

<sup>79</sup> M. Agrawal, V. I. Vasyuchka, A. A. Serga, A. D. Krenowska, G. A. Melkov, and B. Hillebrands, Phys. Rev. Lett. 111, 107204 (2013).

<sup>80</sup> K. Uchida, T. Nonak, T. Kikkawa, Y. Kajiwara, and E. Saitoh, Phys. Rev. B **87**, 104412 (2013).

resulting from careful control of fabrication conditions. To probe the strength of the SSE, a Pt capping layer was grown on each YIG sample. During the SSE measurements, the temperature at the Pt side of the sample was kept constant, while that at the GGG side was varied to realize a temperature difference ( $\Delta T$ ) across the sample thickness. Upon the presence of  $\Delta T$ , the SSE takes place and produces a pure spin current in the Pt layer. Via the inverse spin Hall effect (ISHE),<sup>81,82,83</sup> the spin current then produces an electric voltage ( $V$ ) across one of the lateral dimensions of the Pt layer. The SSE-produced voltage  $V$  was measured as a function of  $\Delta T$ . The data show that the slope of the  $V$  vs.  $\Delta T$  response increases with a decrease in  $\alpha$ . This indicates that the smaller the damping is, the stronger the SSE is, which is qualitatively consistent with the theoretical models in previous works<sup>3,25-27</sup>. Furthermore, the SSE coefficient versus  $\alpha$  response shows almost linear behavior, which was not predicted explicitly in previous works<sup>3,25-27</sup>. The experiments also indicate that the SSE strength shows no notable correlations with the enhanced damping due to spin pumping at the YIG/Pt interface. This can be understood in the frame of the models described by Xiao *et al.*<sup>3</sup> and Kehlberger *et al.*<sup>27</sup>.

## 5.2 Properties of the YIG and YIG/Pt samples

The  $\text{Y}_3\text{Fe}_5\text{O}_{12}$  (YIG) thin films were grown on 0.5-mm-thick, single-crystal, (111)-oriented  $\text{Gd}_3\text{Ga}_5\text{O}_{12}$  (GGG) substrates by RF sputtering at room temperature first and were then annealed in-situ at high temperature in oxygen. Among the various sputtering and annealing control parameters, the most critical parameters for the control of YIG film quality include the argon pressure and the argon flow rate during the sputtering process, the annealing temperature, and the

---

<sup>81</sup> J. E. Hirsch, Phys. Rev. Lett. **83**, 1834-1837 (1999).

<sup>82</sup> S. O. Valenzuela and M. Tinkham, Nature **442**,176 (2006).

<sup>83</sup> A. Hoffmann, IEEE Trans. Magn. **49**, 5172 (2013).

annealing time, as discussed in Chapter 4. For the fabrication of the six YIG thin film samples considered in the SSE study, these four parameters have been carefully chosen so that the YIG samples exhibited very different damping but very similar structural and static magnetic properties (except the surface morphology, as discussed below). Table 5.1 lists the corresponding parameters used for the fabrication of those six samples. The other control parameters which are not listed in the table are very close to those described in Ref. [12]. For given control parameters, the YIG films from different deposition runs show very similar quality as long as the GGG substrates exhibit the same quality.

Table 5.1. Major control parameters for YIG thin film fabrication.

Sample #	Ar pressure (mTorr)	Ar flow rate (sccm)	Annealing temperature(°C)	Annealing time (hr)
1	20	4	800	4
2	20	4	800	3
3	20	4	800	2
4	20	4	800	1
5	25	4	800	4
6	30	4	800	4

The YIG thin films fabricated by sputtering was 10 mm by 10 mm squares. They were then cut into smaller pieces. One of those YIG pieces (about 3 mm by 10 mm) was used for the deposition of a Pt capping layer, and the resultant YIG/Pt sample was then used for the SSE measurements. The other YIG pieces (about 3 mm by 3 mm) were used, directly or after deposition of 5 nm Pt, for characterization, which included X-ray diffraction (XRD), X-ray rocking curve, X-ray photoelectron spectroscopy (XPS), atomic force microscopy (AFM), and ferromagnetic resonance (FMR) measurements. The Pt capping layers were grown by DC sputtering at room temperature with a thickness of about 5 nm.

## 5.2.1 Crystalline and structural properties

X-ray diffraction (XRD), X-ray rocking curve, X-ray photoelectron spectroscopy (XPS), and atomic force microscopy (AFM) measurements were carried out to characterize the crystalline and structural properties of five of the six YIG samples considered in this chapter. Sample #2 was damaged during an ultra-sonic cleaning process, but it is fortunate that the static magnetic and damping properties of sample #2 had been measured previously and had been found to be close to those of sample #1, as shown later in Table 5.3.

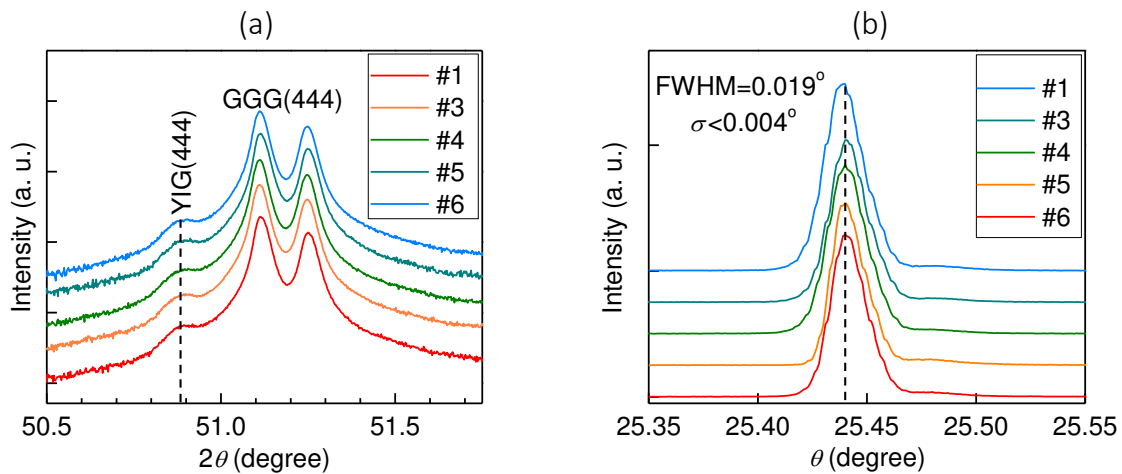


Figure 5.1. XRD data for five YIG thin film samples. (a) XRD spectra. (b) Rocking curves of the YIG (444) peak. The vertical dashed lines indicate the positions of the YIG (444) peaks.

Figure 5.1 presents the XRD data for the five samples. Fig. 5.1(a) presents the XRD spectra, and Fig. 5.1(b) gives the rocking curves for the YIG (444) peaks shown in (a). Figure 5.1(b) also gives the averaged full width at half maximum (FWHM) and corresponding standard deviation ( $\sigma$ ) of the curves. It is evident from the data in Fig. 5.1 that the YIG peaks all appear at the same position (see the vertical dashed lines) and exhibit similar amplitudes and similar linewidths ( $\sigma < 0.004^\circ$ ). These results together clearly indicate that the YIG films in the five samples have similar crystalline properties. Note that the appearance of the two GGG (444) peaks in Fig. 5.1(a) results from the coexistence of the  $K_{\alpha 1}$  and  $K_{\alpha 2}$  components of the Cu X-ray source.

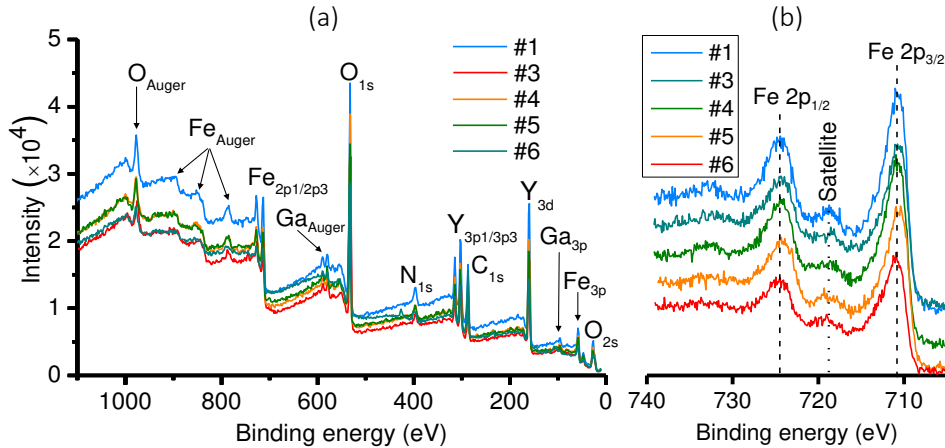


Figure 5.2. XPS data for five YIG thin film samples. (a) Full XPS spectra. (b) XPS profiles in a narrow binding energy range showing the peaks for the Fe 2p states.

Figure 5.2 gives the XPS data for the five samples. Figure 5.2(a) gives the full XPS spectra, with all the main peaks identified, and Fig. 5.2(b) presents the spectra in a narrower binding energy range to show the XPS peaks for the Fe 2p states. In Fig. 5.2(a), in addition to the expected Fe, O, and Y peaks, the Ga peaks are from the GGG substrate, the C peaks result from organic compounds and CO<sub>2</sub> absorbed on the sample surface, and the N peaks probably come from N<sub>2</sub> absorbed on the sample surface. No additional peaks are notable in the spectra, indicating the pure YIG phase in the films. In Fig. 5.2(b), the two major peaks correspond to the Fe 2p<sub>1/2</sub> and Fe 2p<sub>3/2</sub> states, and the appearance of the satellite peaks in-between the two major peaks is a strong evidence for the presence of Fe<sup>3+</sup> only in the YIG films (no Fe<sup>2+</sup>).<sup>84,85</sup>

<sup>84</sup> T. Yamashita, P. Hayes, *Appl. Surf. Sci.* **254**, 2441 (2008).

<sup>85</sup> Y. Zhang, J. Xie, L. Deng, L. Bi, *IEEE Trans. Magn.* **51**, 2503604 (2015).

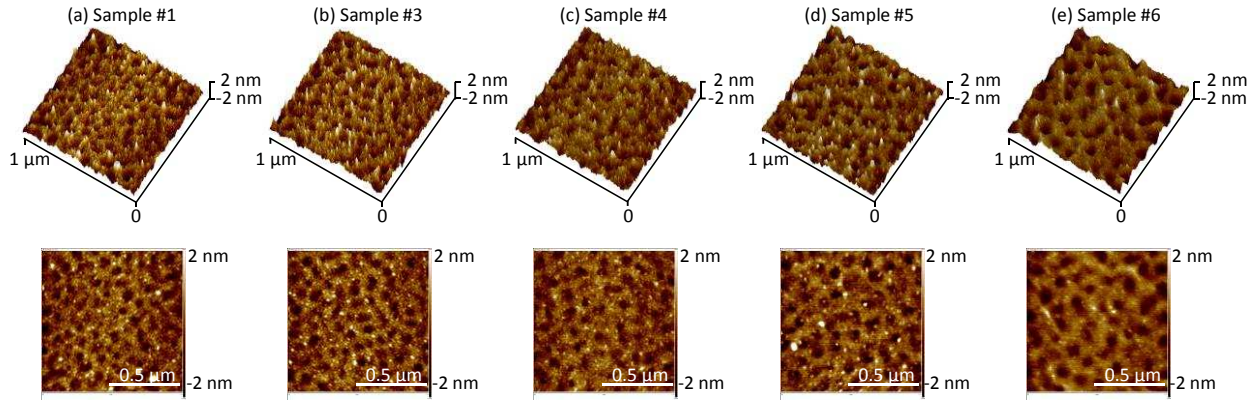


Figure 5.3. AFM surface images of five YIG thin films samples. The first row shows 3D images, while the second row shows the 2D views of the images in the first row.

The AFM surface images of the five YIG samples are presented in Fig. 5.3. The first row gives the 3D images, while the second row gives the 2D views of the 3D images in the first row. The AFM analysis-yielded rms surface roughness values are given in Table 5.2, where the first and second rows list the roughness values for the YIG film samples and the YIG/Pt samples, respectively. The corresponding errors, which are not provided in the table, are either  $\pm 0.01$  nm or less. One can see from the AFM images that the YIG films show surface textures, from finer to bigger as one goes from the left to right. Despite the difference in the surface morphology, however, all the films show very similar roughness values, with the standard deviations of  $\sigma = 0.04$  nm for bare YIG films and  $\sigma = 0.01$  nm for YIG/Pt films.

Table 5.2. Surface rms roughness (nm) of bare YIG and YIG/Pt film samples.

	Sample #1	Sample #3	Sample #4	Sample #5	Sample #6	Average	Standard deviation
YIG	0.51	0.52	0.46	0.54	0.45	0.50	0.04
YIG/Pt	0.14	0.13	0.11	0.14	0.13	0.13	0.01

## 5.2.2 Magnetic properties

The static and dynamical magnetic properties of the bare YIG film and YIG/Pt samples were determined through comprehensive ferromagnetic resonance (FMR) measurements and subsequent data analyses. Figure 5.4 gives the representative FMR data and the numerical fits.

From Fig. 5.4(c)-(f), one can see that the  $|\gamma|$ ,  $4\pi M_{\text{eff}}$ , and  $\alpha$  values obtained for the field-in-plane configuration are almost the same as those obtained for the field-out-of-plane configuration. What's more, this is true for both the samples. This consistency clearly shows the reliability of the FMR results obtained with either field configuration. Furthermore, the consistency of the  $\alpha$  values indicates that the contribution of two-magnon scattering to the  $\alpha$  values is negligible in the sputtered YIG films, as reported previously.<sup>12</sup> In the case that two-magnon scattering occurs, one would expect that the  $\alpha$  values measured with in-plane fields are notably larger than those measured with out-of-plane fields.<sup>74,78</sup> It should be noted that the  $4\pi M_{\text{eff}}$  values presented here may include a perpendicular anisotropy field contribution, but this contribution, if present, is expected to be small, considering the facts that the YIG films have very weak magnetocrystalline anisotropy<sup>37,86</sup> and minimal strain-induced anisotropy due to almost perfect lattice matching with the GGG substrates and the high-temperature annealing process. In addition, none of the previous works on YIG thin films reported the presence of notable perpendicular anisotropy in the films.<sup>10-12,77,87</sup>

---

<sup>86</sup> M. Wu and A. Hoffmann, Recent Advances in Magnetic Insulators – From Spintronics to Microwave Applications (Solid State Physics Vol. **64**, Academic Press, Burlington, 2013, 432 pages).

<sup>87</sup> C. Tang, M. Aldosary, Z. Jiang, H. Chang, B. Madon, K. Chan, M. Wu, J. E. Garay, and J. Shi, Appl. Phys. Lett. **108**, 102403 (2016).

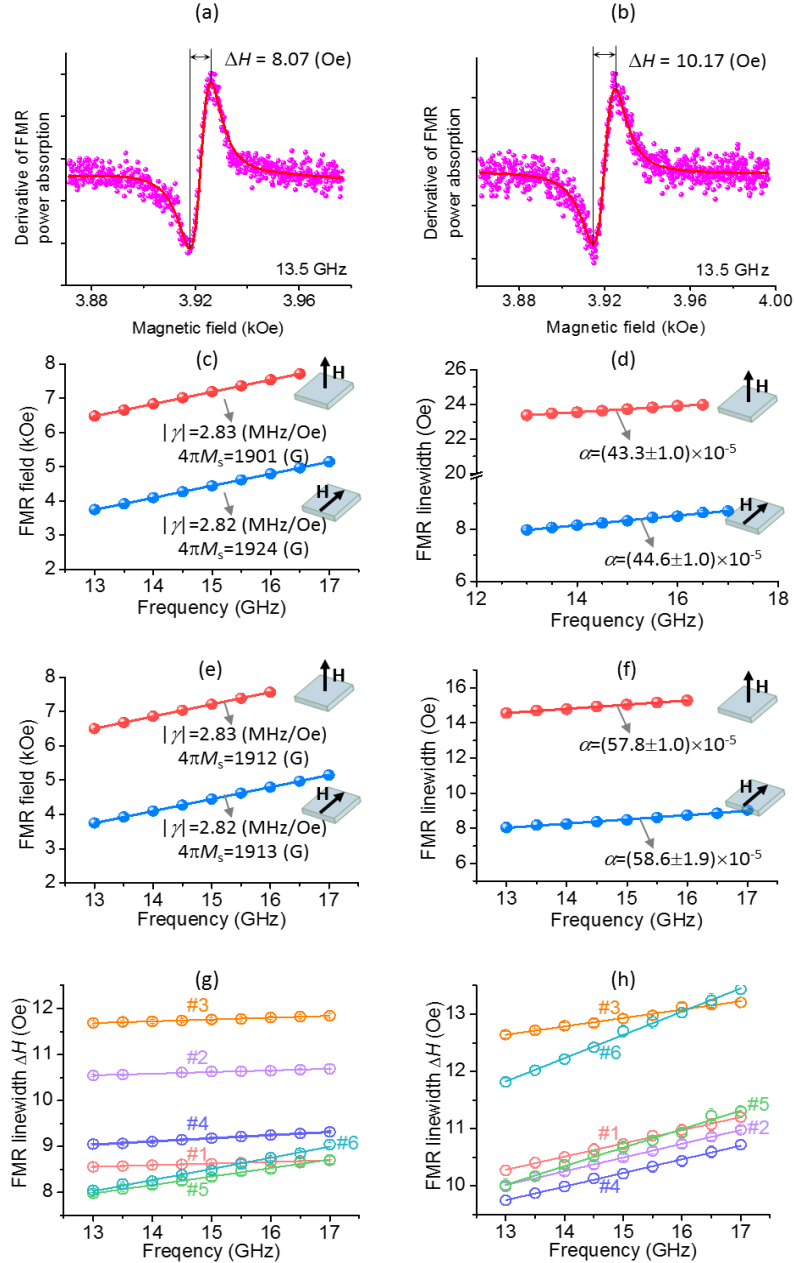


Figure 5.4. FMR properties of bare YIG thin film samples and YIG/Pt bi-layered samples. (a) and (b) show FMR profiles for bare YIG thin film sample #5 before and after the growth of a 5-nm-thick Pt capping layer, respectively. The symbols show the data, while the curves are fits to a Lorentzian trial function. (c) and (d) show the FMR field and linewidth, respectively, as a function of frequency for two different magnetic field ( $\mathbf{H}$ ) configurations for bare YIG thin film sample #5. The symbols show the data, and the lines show the fits to Eq. (3.32) and Eq. (3.45) for (c) and (d) respectively. (e) and (f) present the data in the same format as in (c) and (d) for bare YIG thin film sample #6. (g) presents the FMR linewidth data (symbols) and numerical fits (lines) for six bare YIG thin film samples, while (h) presents the data and fits for the corresponding YIG films after the growth of a 5-nm-thick Pt capping layer. The error bars in (g) and (h) represent the standard error from the Lorentzian fitting function.

Note that for both the samples the inhomogeneous line broadening  $\Delta H_0$  obtained for the field-out-of-plane configuration is larger than that for the in-plane configuration. There are two reasons for this result. First, inhomogeneous line broadening in materials with weak anisotropy is usually more pronounced for the out-of-plane configuration than for the in-plane configuration, as discussed previously in Ref. [88]. Second, the samples used in the out-of-plane measurements had larger dimensions than those used in the in-plane measurements; and in general the larger the sample dimensions are, the more the inhomogeneity contributes to FMR line broadening.

Figure 5.4(g) presents the peak-to-peak linewidth  $\Delta H$  vs.  $f$  data for six bare YIG film samples, as indicated. As in Fig. 5.4(d) and (f), the dots show the  $\Delta H$  data and the lines show the numerical fits with Eq. 3.45. One can see that all the six sets of data can be fitted very well. The fitting-yielded damping values, termed as  $\alpha_{\text{YIG}}$ , are listed in Table 5.3 and are discussed shortly. The fitting-yielded  $\Delta H_0$  value for sample #3 is notably larger than the values for other samples, but this difference speaks nothing about the damping, as  $\Delta H_0$  does not represent loss but results from sample inhomogeneity-caused linewidth increase.

Figure 5.4(h) shows the  $\Delta H$  vs.  $f$  data, in the same format as in Fig. 5.4(g), for the YIG samples after the deposition of a 5-nm-thick Pt capping layer. One can see that the growth of a Pt capping layer not only enhances the linewidth values but also results in notable increases in the slopes. As in Fig. 5.4(g), all the six sets of data in graph (h) can be fitted very well. The fitting-yielded damping values, termed as  $\alpha_{\text{YIG/Pt}}$ , are given in Table 5.3. Note that the data in graphs (g) and (h) were all measured with in-plane magnetic fields.

Table 5.3 summarizes the magnetic properties as well as the dimensions of the six YIG thin film samples without Pt capping layers in rows 2-5 and those of the samples after the growth of a

---

<sup>88</sup> L. Lu, Z. Wang, G. Mead, C. Kaiser, Q. Leng, and M. Wu, Appl. Phys. Lett. **105**, 012405 (2014).

Pt capping layer in rows 6-10. Row 2 gives the thicknesses ( $d$ ) of the YIG films which were determined based on the growth rate and the sputtering time. The YIG growth rate was calibrated by thickness measurements using X-ray reflection and spectral ellipsometry techniques.<sup>89,90</sup> The  $|\gamma|$ ,  $4\pi M_{\text{eff}}$ , and  $\alpha_{\text{YIG}}$  values in rows 3-5 were obtained via numerically fitting the FMR data, as is shown in Fig. 5.4(c)-(f). Rows 6, 7, and 8 present the strip length ( $L$ ), strip width ( $w$ ), and Pt resistance ( $R_{\text{Pt}}$ ) data of the YIG/Pt strip samples, which were indeed the same samples used in the spin Seebeck effect (SSE) measurements. For the damping data in rows 9 and 10, the FMR measurements used smaller samples, which were squares with sides in the 2-4 mm range.

Table 5.3. Properties of six YIG thin film samples before and after the growth of a 5-nm Pt capping layer.

	Sample #1	Sample #2	Sample #3	Sample #4	Sample #5	Sample #6	Average	Standard deviation
$d$ (nm)	23.4	23.4	23.4	23.4	19.7	22.3	22.6	1.4
$ \gamma $ (MHz/Oe)	2.825	2.824	2.816	2.816	2.817	2.820	2.820	0.004
$4\pi M_{\text{eff}}$ (G)	1820	1956	1757	1827	1924	1913	1866	70
$\alpha_{\text{YIG}}$ ( $\times 10^{-5}$ )	$8.5 \pm 0.2$	$8.7 \pm 0.5$	$9.4 \pm 0.3$	$16.5 \pm 0.3$	$45 \pm 1$	$59 \pm 2$	-	-
$L$ (mm)	9.18	9.60	8.94	9.38	8.94	8.97	9.17	0.27
$w$ (mm)	3.53	3.29	2.74	3.20	2.64	2.65	-	-
$R_{\text{Pt}} \cdot w$ ( $\Omega \cdot \text{m}$ )	1.37	1.11	1.21	1.37	1.24	1.23	1.26	0.10
$\alpha_{\text{YIG/Pt}}$ ( $\times 10^{-5}$ )	$55.8 \pm 0.8$	$58.4 \pm 0.8$	$35 \pm 1$	$58 \pm 1$	$77 \pm 2$	$99 \pm 2$	-	-
$\alpha_{\text{sp}}$ ( $\times 10^{-5}$ ) ( $\alpha_{\text{sp}} = \alpha_{\text{YIG/Pt}} - \alpha_{\text{YIG}}$ )	47.3	49.7	25.6	41.5	32	40	39.4	8.4

It is evident from Table 5.3 that the six YIG films have very similar thicknesses (standard deviation  $\sigma = 1.4$  nm), almost equal  $|\gamma|$  values ( $\sigma = 0.004$  MHz/Oe), and comparable  $4\pi M_{\text{eff}}$  values ( $\sigma = 70$  G), but their  $\alpha_{\text{YIG}}$  values differ by a factor of about 7. Since magnon-electron scattering does not occur in insulators, two-magnon scattering is negligible as indicated by the FMR data in graphs (d) and (f) in Fig. 5.4, three-magnon scattering is prohibited as the FMR

<sup>89</sup> E. Jakubisova-Liskova, S. Visnovsky, H. Chang, and M. Wu, J. Appl. Phys. **117**, 17B702 (2015).

<sup>90</sup> E. Jakubisova-Liskova, S. Visnovsky, H. Chang, and M. Wu, Appl. Phys. Lett. **108**, 082403 (2016).

frequency is relatively high, and four-magnon scattering is expected to be weak due to low microwave power (3 dBm) used in the FMR measurements, one can conclude that the damping in the YIG films originates mainly from magnon-phonon relaxation. Note that the magnon-phonon relaxation in a magnetic material is realized through magnon-phonon scattering in which a magnon is annihilated, and some phonons are created and perhaps others annihilated.<sup>37</sup> Via this scattering, the energy of the magnons dissipates into the lattice of the material. The magnon-phonon relaxation is an intrinsic, universal relaxation process, and is usually non-trivial in magnetic insulators but over-dominated by magnon-electron scattering in ferromagnetic metals. Considering the facts that the six YIG films exhibit very similar structural and static magnetic properties but show very different damping, it can be concluded that the films constitute a good system for exploring the role of damping in the SSE. It should be noted that the average of the six  $4\pi M_{\text{eff}}$  values given in Table 5.3 is 1866 G, and the corresponding standard deviation is 70 G, indicating that the  $4\pi M_{\text{eff}}$  values are comparable. This fact is important for the determination of the roles of the damping in the SSE because the SSE strength varies with  $4\pi M_{\text{eff}}$  as demonstrated by previous experimental studies.<sup>80</sup>

After the growth of a Pt capping layer, however, the damping in the YIG film also contains a contribution due to spin pumping from the YIG film to the Pt layer. As a result, the damping constant consists of two components, namely,  $\alpha_{\text{YIG/Pt}} = \alpha_{\text{YIG}} + \alpha_{\text{sp}}$ .  $\alpha_{\text{YIG}}$  describes the contribution from the intrinsic damping in the bulk of the YIG, while  $\alpha_{\text{sp}}$  describes the interfacial coupling between the magnons in the YIG film and the electrons in the Pt layer. The magnon-electron coupling at the YIG/Pt interface is realized through the s-d exchange interaction, where “s” refers to conduction electrons in the Pt layer and “d” refers to localized electrons in the YIG

film.<sup>91</sup> Such s-d exchange interaction may serve as an interface pinning, modify the magnetization along thickness direction, and lead to FMR field shift as indicated by Eq. 3.31 and Sec. 3.3. However, such FMR field shift is very small (<15 Oe) and is irrelevant with the SSE experiment. It is fortunate that these two components,  $\alpha_{\text{YIG}}$  and  $\alpha_{\text{sp}}$ , can be separated unambiguously, as shown in Table 5.3, and this facilitates the examination of the effects of each damping component on the SSE, as discussed later. Note that the magnons in the YIG film are also coupled to the phonons in the Pt layer, but the contribution of this coupling to the damping is expected to be much weaker than that of the magnon-electron coupling. In addition to  $\alpha_{\text{sp}}$ , the growth of the Pt capping layer might also lead to an enhancement in the surface imperfection-associated damping in the YIG film. However, this damping should be much smaller than  $\alpha_{\text{sp}}$ , as is shown by previous experimental studies on the damping in YIG/Cu and YIG/Cu/Pt layered samples.<sup>56</sup>

Several additional points should be made regarding the data presented in Table 5.3.

- (1) The  $|\gamma|$  values are all close to the standard value (2.8 MHz/Oe), indicating that the YIG films are of high quality.
- (2) All the samples had a  $4\pi M_{\text{eff}}$  value larger than the bulk value (1750 G). Possible reasons for this deviation include that there might exist weak anisotropy in the films,<sup>37,86</sup> and the films might be slightly off-stoichiometric.<sup>56</sup> The standard deviation of  $4\pi M_{\text{eff}}$ , however, is only 3.8% of the bulk value. This indicates the comparability of the  $4\pi M_{\text{eff}}$  values.
- (3) The products of  $R_{\text{Pt}}W$  are comparable. Considering that the samples had similar lengths, this means that the Pt layers should have very similar thicknesses. Since the Pt resistivity

---

<sup>91</sup> S. Takahashi, E. Saitoh, and S. Maekawa, J. Phys. Conf. Ser. **200**, 062030 (2010).

increases sharply with a decrease in the Pt thickness over the 1-10 nm range,<sup>92</sup> a small change in the thickness would lead to a big change in  $R_{\text{Pt} \times \text{W}}$ .

(4)  $\alpha_{\text{sp}}$  changes from sample to sample, which is likely due to the YIG surface quality (such as, the texture)-associated difference in the quality of the YIG/Pt interface. However, the range of the  $\alpha_{\text{sp}}$  variation is significantly narrower than that of  $\alpha_{\text{YIG}}$ . Also, this variation does not significantly influence the comparison of the SSE efficient across different samples, although it does affect the absolute amplitudes of the SSE-produced ISHE voltage signals.

(5)  $\alpha_{\text{YIG}}$  for sample #1 represents the lowest damping value reported so far for YIG films with a thickness of about 20 nm.<sup>93</sup> It is also the lowest damping reported ever for any magnetic thin films with a thickness in the nanometer range (<100 nm).

The samples described above constitute a good material system for testing the role of the damping on the SSE in YIG thin films. There are two reasons. First, the damping constants in the YIG films differ by as large as a factor of 7, as shown by the FMR measurements. Second, except the surface morphology the other properties are either very close or comparable for the different YIG films, as listed below

- 1) The film thicknesses are all close to 22.6 nm, with  $\sigma = 1.4$  nm.
- 2) The surface roughness values are all close to 0.50 nm, with  $\sigma = 0.04$  nm.
- 3) The films were grown on almost identical substrates, all being 0.50 mm thick.
- 4) The films have similar crystalline properties, as shown by the XRD data.
- 5) The films have  $\text{Fe}^{3+}$  ions only (no  $\text{Fe}^{2+}$ ), as shown by the XPS data.
- 6) The  $4\pi M_{\text{eff}}$  values are close to each other ( $\sigma = 70$  G) and is only 3.8% of the bulk value.

---

<sup>92</sup> J. S. Agustsson, U. B. Arnalds, A. S. Ingason, K B. Gylfason, K. Johnsen S. Olafsson, and J. T. Gudmundsson, J. Phys. Conf. Ser. **100**, 082006 (2008).

<sup>93</sup> B. M. Howe, S. Emori, H. -M. Heon, T. M. Oxholm, J. G. Jones, K. Mahalingam, Y. Zhuang, N. X. Sun, and G. J. Brown, IEEE Magn. Lett. **6**, 3500504 (2015).

7) The  $|\gamma|$  values are almost equal to each other, with  $\sigma = 0.004$  MHz/Oe, and are all close to the standard value.

It is important to highlight that the damping in the YIG films in this work originates mainly from magnon-phonon scattering, which is an intrinsic relaxation process. This is because

- Magnon-electron scattering does not occur in insulators.
- Two-magnon scattering is negligible as indicated by comparing the FMR data measured with in-plane and out-of-plane fields.
- Three-magnon scattering is prohibited as the FMR frequency is relatively high.
- Four-magnon scattering is expected to be weak as the microwave power used in the FMR measurements is relatively low (3 dBm).

It should be noted that the damping discussed above measures the relaxations of the uniform mode in the YIG films, while the SSE involves non-uniform spin-wave modes. However, it is expected that the damping of spin waves varies between the six YIG films in the same trend as the damping value determined by the FMR measurements. This is because the spin-wave dispersion is given for a particular film and a particular external magnetic field, while for a given dispersion the spin-wave damping generally increases with the damping of the uniform mode.<sup>35</sup> Based on the discussions above, one can conclude that the magnon-phonon scattering in the six YIG film samples has different strength. It is likely that this difference results from the difference in the microstructure properties of the YIG films. The YIG films show very similar XRD and XPS results as well as very comparable surface roughness as discussed above, but the surface morphology differs for different films as indicated by the AFM measurements. Also, there exists a correlation between the YIG surface texture and the damping constant. It is believed that the YIG films with different surface textures exhibit dissimilar granular properties,

while the dissimilarity in the surface morphology and grain properties gives rise to a difference in the level of magnon-phonon coupling. The fact that the films show different surface morphology is because they were prepared under different sputtering and annealing conditions.

### 5.3 Spin Seebeck measurements

Turn now to the SSE experiments on the YIG/Pt samples. Figure 5.5(a) shows a schematic diagram of the experimental setup. During the SSE measurement, an external field of about 930 Oe was applied in-plane and perpendicular to the length of the YIG/Pt strip. The temperature at the Pt side of the YIG/Pt sample,  $T_{Pt}$ , was kept constant, while temperature at the GGG side of the sample,  $T_{GGG}$ , was varied. This was realized by placing a Peltier device on the Pt side of the sample, inserting a thermal couple in-between the Peltier device and the sample to measure  $T_{Pt}$ ,

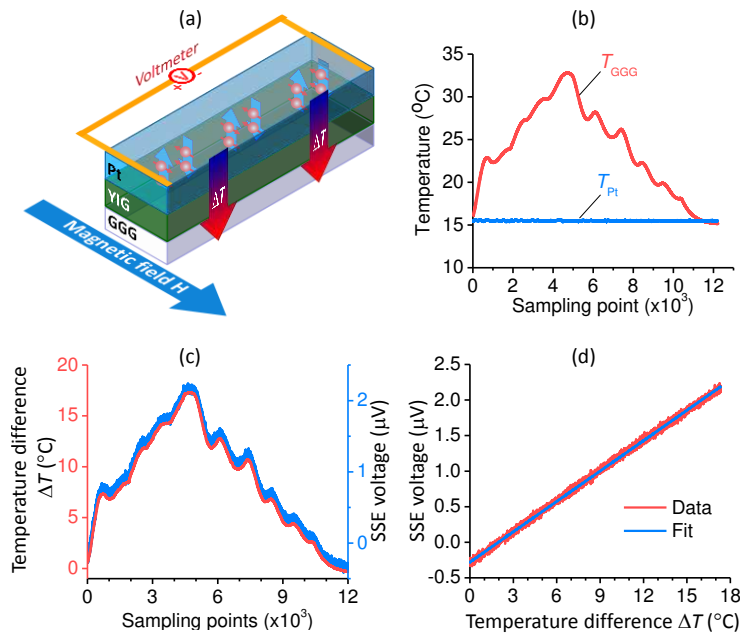


Figure 5.5. SSE measurements. (a) shows a schematic of the experimental setup. (b)-(d) give the data obtained with YIG/Pt sample #1. (b) presents the temperatures on the Pt and GGG sides of the sample,  $T_{Pt}$  and  $T_{GGG}$ . (c) presents  $\Delta T (=T_{GGG}-T_{Pt})$  and the corresponding voltage signal  $V$ . The horizontal axes in (b) and (c) show sampling points, and 1000 points correspond to a period of 4 minutes. (d) shows the  $V$  vs.  $\Delta T$  response plotted using the data in (c). The thin blue line in (d) shows a linear fit.

and utilizing a computer to take the feedback from the couple to control the Peltier device. A second Peltier device was placed on the GGG side of the sample to vary its temperature,  $T_{GGG}$ , which was probed by another thermal couple inserted in-between the Peltier device and the GGG substrate. When the difference  $\Delta T = T_{GGG} - T_{Pt}$  is non-zero, the SSE occurs in the YIG and produces a pure spin current flowing into the Pt. The spin current then gives rise to a measurable voltage  $V$  across the length of the Pt strip via the ISHE.<sup>81-83</sup> Note that the purpose of keeping  $T_{Pt}$  constant is to minimize the change of the average temperature of the YIG and thereby to avoid the effects due to the change of the absolute temperature. The other purpose is to minimize the change of the possible temperature gradient along the length of the Pt strip during the SSE voltage  $V_{SSE}$  vs.  $\Delta T$  ( $T_{GGG} - T_{Pt}$ ) measurements. Such temperature gradients, if present, give rise to non-zero  $V_{SSE}$  offsets in the  $V_{SSE}$  vs.  $\Delta T$  plots.

Figures 5.5(b), (c), & (d) give SSE data obtained with YIG/Pt sample #1. Figure 2(b) presents the  $T_{Pt}$  and  $T_{GGG}$  data, while Fig. 2(c) presents  $\Delta T$  (left axis) and the corresponding  $V$  data (right axis). For the data shown in Fig. 5.5(b) & (c), the horizontal axis is equivalent to the time where the sampling period was about 240 ms. During the SSE measurements, the data acquisition was suspended whenever  $T_{Pt}$  deviated away from  $15.5 \pm 0.1$  °C. For this reason, the time recorded in the raw data was not continuous, and for better presentation the axis was named as “sampling points” where 1000 points correspond to a time period of about 4 minutes. One can see that during the measurements  $T_{Pt}$  was kept constant at 15.5 °C,  $T_{GGG}$  was varied over a range of about 15-33 °C, and  $V$  changed in almost the same manner as  $\Delta T$ . These results indicate that the voltage signal is associated with the temperature gradient in the YIG, rather than the absolute temperature of the YIG or the Pt. Note that one can consider that the average temperature in the YIG was almost constant just as  $T_{Pt}$ , based on the fact that the GGG substrate (0.5 mm) is

considerably thicker than the YIG film ( $\sim 20$  nm). Figure 5.5(d) plots  $V$  as a function of  $\Delta T$ , using the data in Fig. 5.4(g). The red coarse line consists of the experimental data points, and the blue thin line shows a fit. One can see that the  $V$  vs.  $\Delta T$  response is almost perfectly linear. This linear behavior is expected by all the four SSE models described in the introduction.<sup>3,24,25,27</sup>

Several additional notes should be made regarding the data shown in Fig. 5.5. First, it should be mentioned that reversing the magnetic field direction resulted in a flip in the voltage sign, as shown in Fig. 5.6 and discussed below. This is the same as reported previously.<sup>17,21</sup> It is because the direction of the magnetization in the YIG film dictates the polarization direction of the SSE-produced spin current in the Pt layer. Second, the data in Fig. 5.5(d) do not show any hysteresis or loop behavior in response to the change of  $\Delta T$  from  $0$  °C to about  $17$  °C first and then back to  $0$  °C. This indicates that the GGG side of the sample reached a quasi-equilibrium during the SSE measurements. Finally, the measured SSE voltage might contain a small contribution from the anomalous Nernst effect in the Pt layer. Such a contribution is expected to be negligible in comparison with SSE signals, as demonstrated by a recent experimental study.<sup>94</sup>

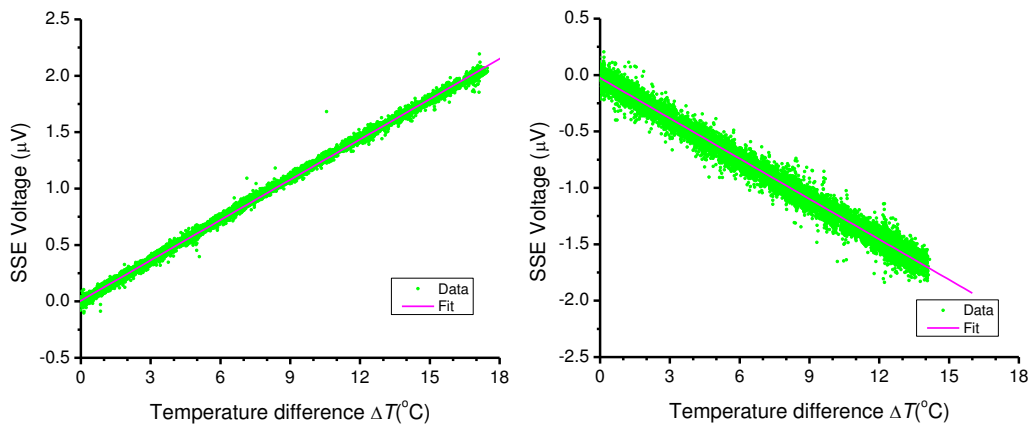


Figure 5.6. Effects of the magnetic field direction on the SSE. The left and right graphs show the SSE voltage vs. temperature difference data obtained under opposite magnetic fields on an YIG(30 nm)/Pt(2.5 nm) sample. The green dots show the experimental data, and the purple lines show linear fits.

<sup>94</sup> B. F. Miao, S. Y. Huang, D. Qu, and C. L. Chien, AIP Adv. **6**, 015018 (2016).

Fig. 5.6 shows the SSE data for two opposite the magnetic field directions. When the direction of the magnetic field was reversed, the voltage  $V_{\text{SSE}}$  flipped its sign. This is consistent with the theoretical expectation in which the direction of the magnetization vector in the YIG layer dictates the polarization of the SSE-produced spin current in the Pt layer, and the reversal of the magnetization direction results in a flip in the spin-current polarization and a corresponding change in the sign of  $V_{\text{SSE}}$ . This effect is demonstrated by the data shown in Fig. 5.6, where the left and right graphs present the SSE data obtained with opposite external magnetic fields. Several results are evident in Fig. 5.6. First, the data can be fitted very well, confirming the linear behavior shown by the data in Fig. 5.5 (d). Second, it is very clear that a flip in the field direction leads to a flip in the sign of  $V_{\text{SSE}}$ , as discussed above. Third, in spite of the sign change the absolute values of the two slopes perfectly match each other, indicating that the reverse of the field direction does not affect the SSE strength, as expected. Note that the fitting-yielded slopes for the left and right graphs are  $119.08 \pm 0.04$  nV/K and  $-119.22 \pm 0.10$  nV/K, respectively. Finally, it should be mentioned that the data in Fig. 5.6 were measured after the experimental setup was carefully arranged to minimize the  $V_{\text{SSE}}$  offsets at  $\Delta T = 0$ . The fitting-yielded offsets for the left and right graphs are  $6.79 \pm 0.38$  nV and  $-25.86 \pm 0.80$  nV, respectively. These offsets are one or two orders of magnitude smaller than those shown in Fig. 5.5(d). They also differ significantly from each other, and this is because the samples were re-positioned and the nano-voltmeter was reconnected between the two measurements.

## 5.4 Role of damping on the SSE

Figure 5.7 presents the key results of this chapter. Fig. 5.7(a) presents the SSE-produced  $V$  as a function of  $\Delta T$  for six YIG/Pt samples, as indicated. Figure 5.7(b) presents the linear fits to the data in Fig. 5.7 (a). In Fig. 5.7 (b) the y-axis intercepts are all removed for a better

presentation. Those intercepts are independent of  $\Delta T$  and are therefore not associated with the SSE. They might result from the conventional Seebeck effect-produced voltage in response to a

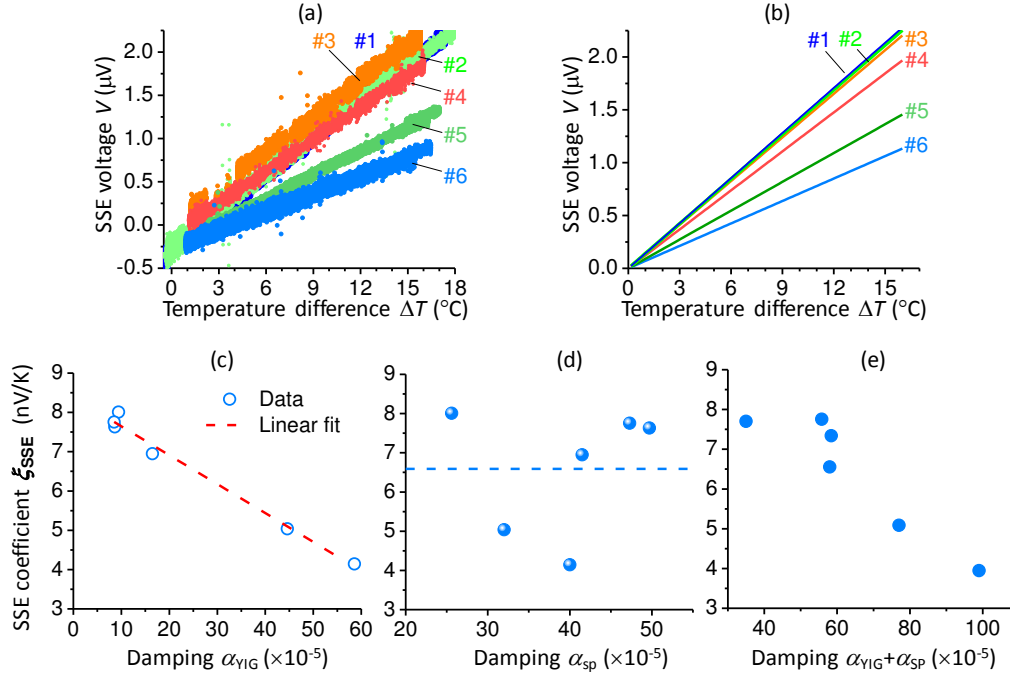


Figure 5.7. Effects of damping in the SSE. (a) shows the SSE-produced voltage as a function of  $\Delta T$  ( $=T_{\text{GGG}}-T_{\text{Pt}}$ ) measured on six different YIG/Pt samples. (b) shows the linear fits to the data in (a). (c), (d), and (e) give the SSE coefficient, which is defined by Eq. 5.1, as a function of  $\alpha_{\text{YIG}}$ ,  $\alpha_{\text{sp}}$ , and  $\alpha_{\text{YIG}}+\alpha_{\text{sp}}$ , respectively.

possible temperature gradient along the Pt length and small voltage offsets in the voltmeter. One can significantly reduce those voltage intercepts by carefully arranging the experimental setup, as is shown in Fig. 5.6 of Sec. 5.3. If one takes  $D$  as the sample thickness and  $L$  as the distance between the two electrodes (see Fig. 5.5(a)) and defines<sup>95</sup>

$$\xi_{\text{SSE}} = \frac{(V/L)}{(\Delta T/D)} = \frac{V}{\Delta T} \frac{D}{L} \quad (5.1)$$

as the geometry-free SSE coefficient, one can then use the slope of the  $V$  vs.  $\Delta T$  lines in Fig. 5.7(b) to determine the  $\xi_{\text{SSE}}$  values for different samples and thereby examine how  $\xi_{\text{SSE}}$  varies

<sup>95</sup> A. Sola, M. Kuepferling, V. Basso, M. Pasquale, T. Kikkawa, K. Uchida, and E. Saitoh, J. Appl. Phys. **117**, 17C510 (2015).

with the damping by plotting  $\xi_{\text{SSE}}$  as a function of  $\alpha_{\text{YIG}}$ ,  $\alpha_{\text{sp}}$ , or  $\alpha_{\text{YIG}} + \alpha_{\text{sp}}$ . Such plots are presented in Figs. 5.7(c), 5.7(d), and 5.7(e).

It is evident from the data in Fig. 5.7(c) that  $\xi_{\text{SSE}}$  increases with a decrease in  $\alpha_{\text{YIG}}$ , indicating that the SSE is stronger if the damping is weaker. This result is qualitatively consistent with the theoretical models proposed in Refs. [3] and [25] and simulation results presented in Refs. [26] and [27]. The underlying physics is that the damping in the YIG films originates mainly from magnon-phonon scattering as discussed above; the weaker the magnons are coupled to the phonons, the more the magnon temperature  $T_{\text{m}}$  deviates from the phonon temperature  $T_{\text{p}}$  at the YIG/Pt interface, according to the model proposed in Ref. [3]. Note that previous work has demonstrated a good agreement between the simulations using this model and the experiments using YIG/Pt heterostructures.<sup>96</sup> In the terminology described in Refs. [25-27], the underlying physics is that the weaker the damping is, the more the magnons propagate from the bulk to the interface and contribute to the SSE signal. Further, the data in Fig. 5.7(c) also indicate that the  $\xi_{\text{SSE}}$  vs.  $\alpha_{\text{YIG}}$  response shows quasi-linear behavior for the given damping range, as suggested by the red dashed line. Understanding of this quasi-linear response calls for new theoretical studies.

In a stark contrast, the data in Fig. 5.7(d) do not show any obvious correlations between  $\xi_{\text{SSE}}$  and  $\alpha_{\text{sp}}$ . This can be understood in the frame of the SSE models described in Refs. [3] and [27]. Specifically,  $\alpha_{\text{sp}}$  plays two roles in the process in which the SSE in the YIG produces spin currents in the Pt. On one hand, a larger  $\alpha_{\text{sp}}$  value indicates a more efficient spin transfer at the YIG/Pt interface,<sup>5</sup> and one should therefore expect larger spin currents in the Pt in samples with larger  $\alpha_{\text{sp}}$ . On the other hand, the spin transfer at the interface at the same time causes a decrease in the difference between  $T_{\text{m}}$  in the YIG and  $T_{\text{e}}$  in the Pt near the interface, resulting in a weaker

---

<sup>96</sup> M. Schreier, A. Kamra, M. Weiler, J. Xiao, G. E. W. Bauer, R. Gross, and S. T. B. Goennenwein, Phys. Rev. B **88**, 094410 (2013).

SSE. One can see that these two roles are opposite, and as a result  $\xi_{\text{SSE}}$  does not show an explicit dependence on  $\alpha_{\text{sp}}$ . Note that the blue dashed line in Fig. 5.7(d) indicates the average  $\xi_{\text{SSE}}$ .

Considering that some of the previous theoretical analyses involved the total damping in the FM,<sup>3,24</sup> in Fig. 5.7(e)  $\xi_{\text{SSE}}$  is plotted as a function of  $\alpha_{\text{YIG}} + \alpha_{\text{sp}}$ . One can see that the overall trend is  $\xi_{\text{SSE}}$  increases with a decrease  $\alpha_{\text{YIG}} + \alpha_{\text{sp}}$ . This trend results from the facts that  $\xi_{\text{SSE}}$  clearly increases with decreasing  $\alpha_{\text{YIG}}$  but shows no explicit correlations with  $\alpha_{\text{sp}}$ , as discussed above.

## 5.5 Summary

The effects of the intrinsic damping in the YIG bulk ( $\alpha_{\text{YIG}}$ ) and the enhanced damping due to interfacial spin pumping ( $\alpha_{\text{sp}}$ ) on the SSE in the YIG/Pt bi-layered structures have been studied experimentally. The data show that smaller damping  $\alpha_{\text{YIG}}$  gives stronger SSE. This observation is consistent with some existing theoretical models.<sup>3,25-27</sup> The SSE coefficient vs.  $\alpha_{\text{YIG}}$  response is almost linear and was not predicted explicitly by previous models. The data also show no explicit correlations between the SSE strength and  $\alpha_{\text{sp}}$ , which can be interpreted using the terminology of two existing models.<sup>3,27</sup> One can expect similar results in other magnetic insulator/NM heterostructures. The results, however, might be different in ferromagnetic metal/NM heterostructures, due to the facts that (1) in ferromagnetic metals magnon-electron scattering plays critical roles in the intrinsic damping<sup>36,97,98</sup> and (2) the spin transfer at a ferromagnetic metal/NM interface is much more efficient than that at a magnetic insulator/NM interface.<sup>99,100</sup>

---

<sup>97</sup> J. Kuneš and V. Kamberský, Phys. Rev. B **65**, 212411 (2002).

<sup>98</sup> K. Gilmore, Y. U. Idzerda, and M. D. Stiles, Phys. Rev. Lett. **99**, 027204 (2007).

<sup>99</sup> R. Urban, G. Woltersdorf, and B. Heinrich, Phys. Rev. Lett. **87**, 217204 (2011).

<sup>100</sup> Y. Tserkovnyak, A. Brataas, and G. E. W. Bauer, Phys. Rev. Lett. **88**, 117601 (2002).

# CHAPTER 6

## SPUTTERING GROWTH OF $\text{Y}_3\text{Fe}_5\text{O}_{12}$ ON PLATINUM LAYERS AND SPIN TRANSFER AT $\text{Y}_3\text{Fe}_5\text{O}_{12}/\text{Pt}$ INTERFACES

### 6.1 Motivation

As mentioned previously, recently there is a strong interest in studying  $\text{Y}_3\text{Fe}_5\text{O}_{12}$  (YIG)-based spintronics, and this interest is mainly driven by the fact that YIG materials have a damping constant lower than any other magnetic materials. In terms of the Gilbert damping, the damping constant ( $\alpha$ ) in YIG materials is found to be  $\alpha \approx 3 \times 10^{-5}$ , which is two orders of magnitude lower than that in conventional ferromagnetic metals.<sup>37</sup> Apart from the low damping feature, YIG materials are also electrically insulating, shunting no current when an electric current flows in a neighboring normal metal (NM) or topological insulator (TI) layer.

The majority of the previous studies on YIG spintronics utilized YIG films that were grown on single-crystal  $\text{Gd}_3\text{Ga}_5\text{O}_{12}$  (GGG) substrates first and then capped with either a thin NM layer<sup>2,7,8,101,102,103,104,105,106</sup> or a thin TI layer<sup>107,108</sup>. The use of the GGG substrates is crucial in

---

<sup>101</sup> G. L. da Silva, L. H. Vilela-leão, S. M. Rezende, and A. Azevedo, *J. Appl. Phys.* **111**, 07C513 (2012).

<sup>102</sup> P. Pirro, T. Brächer, A. V. Chumak, B. Lägél, C. Dubs, O. Surzhenko, P. Gönert, B. Leven, and B. Hillebrands, *Appl. Phys. Lett.* **104**, 012402 (2014).

<sup>103</sup> J. Flipse, F. K. Dejene, D. Wagenaar, G. E. W. Bauer, J. Ben Youssef, and B. J. van Wees, *Phys. Rev. Lett.* **113**, 027601 (2014).

terms of realizing high-quality YIG films, because GGG not only has a crystalline structure almost perfectly matching that of YIG but is also extremely stable at high temperature in oxygen that is the condition needed for YIG crystallization. The growth of the NM or TI capping layer on the top of the YIG, on the other hand, is fairly easy to achieve and usually does not alter the properties of the YIG layer except enhancing the damping via spin pumping.

This chapter discusses the feasibility of growing high-quality YIG thin films on Pt thin films. It is technically challenging to grow high-quality YIG films on metallic films, and possible issues include the oxidation and peeling-off of the metallic layer, interfacial diffusion, and formation of pin-holes in the films during the growth or post-annealing process. In this work a unique sputtering process was developed that successfully resolved these issues.

The feasibility demonstrated in this work is of great significance because it enables the fabrication of sandwich-like NM/YIG/NM or NM/YIG/TI structures. Such tri-layered structures will facilitate various interesting fundamental studies as well as device developments where, for example, one can use the top NM or TI layer as a writing layer to induce precession dynamics, domain wall motion, or even magnetization reversal in the middle YIG layer and use the bottom NM layer as a reading layer to probe the magnetization status in the YIG layer. In fact, in 2016 Pt/YIG/Pt sandwich structures have been used, independently by Wu *et al.*<sup>109</sup> and Li *et al.*<sup>110</sup>, to

---

<sup>104</sup> M. Collet, X. de Milly, O. d'Allivy Kelly, V. V. Naletov, R. Bernard, P. Bortolotti, J. Ben Youssef, V. E. Demidov, S. O. Demokritov, J. L. Prieto, M. Muñoz, V. Cros, A. Anane, G. de Loubens, and O. Klein, *Nat. Commun.* **7**, 10377 (2016).

<sup>105</sup> M. B. Jungfleisch, W. Zhang, J. Sklenar, J. Ding, W. Jiang, H. Chang, F. Y. Fradin, J. E. Pearson, J. B. Ketterson, V. Novosad, M. Wu, and A. Hoffmann, *Phys. Rev. Lett.* **116**, 057601 (2016).

<sup>106</sup> K. Ganzhorn, S. Klingler, T. Wimmer, S. Geprägs, R. Gross, H. Huebl, and S. T. B. Goennenwein, *Appl. Phys. Lett.* **109**, 022405 (2016).

<sup>107</sup> Y. Fan, P. Upadhyaya, X. Kou, M. Lang, S. Takei, Z. Wang, J. Tang, L. He, L. -T. Chang, M. Montazeri, G. Yu, W. Jiang, T. Nie, R. N. Schwartz, Y. Tserkovnyak, and K. L. Wang, *Nat. Materials*, **13**, 699 (2014).

<sup>108</sup> Z. Jiang, C. -Z. Chang, M. R. Masir, C. Tang, Y. Xu, J. S. Moodera, A. H. MacDonald, and J. Shi, *Nat. Commun.* **7**, 11458 (2016).

<sup>109</sup> H. Wu, C. H. Wan, X. Zhang, Z. H. Yuan, Q. T. Zhang, J. Y. Qin, H. X. Wei, X. F. Han, and S. Zhang, *Phys. Rev. B* **93**, 060403 (2016).

demonstrate for the first time magnon-mediated electric current drag, a phenomenon predicted by Zhang *et al.* in 2012.<sup>111</sup> However, despite the intriguing physics which those works demonstrated, the YIG layers in the structures exhibited relatively low quality. Specifically, in the work by Li *et al.* the YIG layers had a relatively low resistivity and underwent current leakage at room temperature (RT)<sup>110</sup>, and in the work by Wu *et al.* the YIG layers showed a large peak-to-peak ferromagnetic resonance (FMR) linewidth ( $\Delta H$ ), about 358 Oe at 9 GHz.<sup>109</sup>

## 6.2 Samples fabrication and characterization

This section presents the use of an optimized sputtering process to grow YIG/Pt bi-layers on GGG substrates that show high quality in terms of the FMR linewidth, damping, and electric resistivity in the top YIG layer. Control experiments are also discussed.

### 6.2.1 High-quality YIG/Pt/GGG thin film samples by optimized development process

The YIG(58 nm)/Pt(12 nm) sample was prepared using the optimized sputtering and annealing parameters listed in Table 6.1. The films were grown on 0.5-mm-thick, (111)-oriented, single-crystal GGG substrates. In this structure, the YIG layer showed  $\Delta H = 8 - 9$  Oe over 13-18 GHz, which is considerably smaller than the  $\Delta H$  value cited above,<sup>109</sup> and a damping constant less than  $4.7 \times 10^{-4}$ , which is comparable to the  $\alpha$  value in YIG films grown on GGG substrates by pulsed laser deposition (PLD).<sup>10,77,93,112</sup>

---

<sup>110</sup> J. Li, Y. Xu, M. Aldosary, C. Tang, Z. Lin, S. Zhang, R. Lake, and J. Shi, Nat. Commun. **7**, 10858 (2016).

<sup>111</sup> S. S. -L. Zhang and S. Zhang, Phys. Rev. Lett. **109**, 096603 (2012).

<sup>112</sup> M. C. Onbasli, A. Kehlberger, D. H. Kim, G. Jakob, M. Kläui, A. V. Chumak, B. Hillebrands, and C. A. Ross, APL Mater. **2**, 106102 (2014).

Table 6.1. Main steps and major control parameters for the fabrication of the YIG(58 nm)/Pt(12 nm)/GGG(0.5 mm) sample.

Steps	Major control parameters	
	1 <sup>st</sup> Pt deposition	Ar pressure
Ar flow		3 sccm
Substrate temperature		400 °C
Sputtering power (DC)		60 W
Sputtering time		25 s
2 <sup>nd</sup> Pt deposition	Ar pressure	3 mTorr
	Ar flow	3 sccm
	Substrate temperature	25 °C
	Sputtering power (DC)	60 W
	Sputtering time	47 s
YIG deposition	Ar pressure	20 mTorr
	Ar flow	4 sccm
	Substrate temperature	25 °C
	Sputtering power (RF)	75 W
	Sputtering time	60 min
1 <sup>st</sup> annealing	O <sub>2</sub> pressure	1.1 Torr
	Annealing temperature	650 °C
	Annealing time	60 min
2 <sup>nd</sup> annealing	O <sub>2</sub> pressure	1.1 Torr
	Annealing temperature	700 °C
	Annealing time	30 min

There are three major procedures: (i) Pt deposition by DC sputtering, (ii) YIG deposition by RF sputtering at RT, and (iii) post-annealing at high temperatures. For the Pt deposition, the GGG substrate temperature plays a rather critical role. The Pt layers deposited at RT exhibit smooth surfaces but encompass large stress, and stress releasing during the later annealing process often produces bumps and spikes on the surface of the top YIG layer. On the other hand,

deposition at higher temperatures can yield Pt films with much less stress, but such films are usually granular and exhibit very rough surfaces that affect the subsequent YIG deposition and prevent the realization of high-quality YIG/Pt interfaces. For this reason, a two-step Pt growth process is taken, in which one deposits a thin Pt layer at 400 °C first and then deposits further by RT sputtering. The first step serves to grow a thin Pt layer with relatively low stress and strong adhesion to the substrate, while the second ensures a relatively smooth surface needed by the subsequent YIG deposition. The Pt growth is followed by the deposition of an amorphous YIG layer by RT sputtering and then two distinct annealing steps. The first annealing is done at a relatively low temperature (650 °C) for a relatively long time (60 min), mainly serving to release the stress in the structure. The second is carried out at a higher temperature (700 °C) required for YIG crystallization for a relatively short time period (30 min) that is just sufficiently long for YIG crystallization. The other parameters not listed are the same as those described in Ref. [12].

Figures 6.1 gives representative data that show the structural and morphologic properties of the YIG(58 nm)/Pt(12 nm)/GGG(0.5 mm) sample. Figures 6.1(a) and 6.1(b) present two high-angle annular dark-field (HAADF) scanning transmission electron microscopy (STEM) images of the sample cross-section using different scales, as indicated. The STEM measurements used an FEI Titan G2 60–300 S/TEM system equipped with a Schottky X-FEG gun and operated at 200 kV.

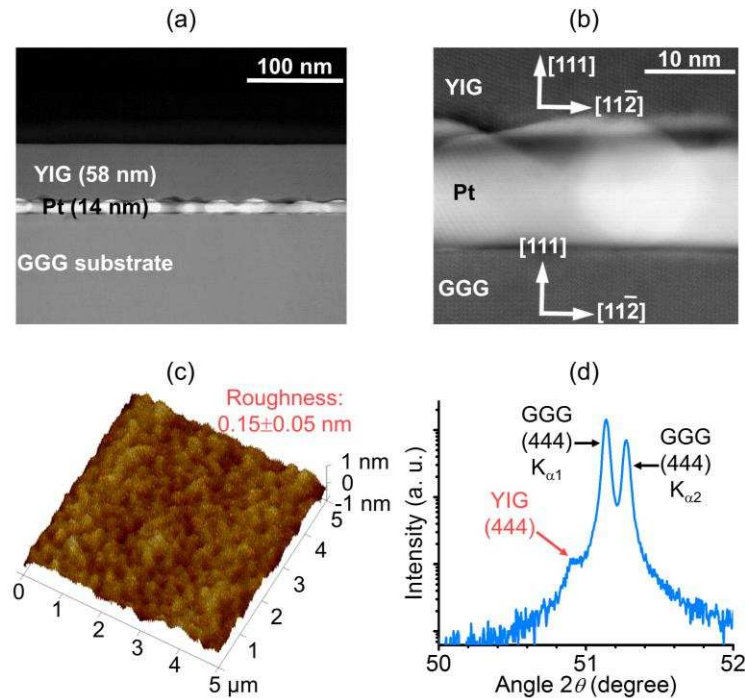


Figure. 6.1. Structural and morphologic properties of YIG(58 nm)/Pt(12 nm)/GGG(0.5 mm). (a) HAADF-STEM cross-section image. (b) HAADF-STEM cross-section image with a scale 10 times bigger than that in (a). (c) AFM surface image. (d) XRD spectrum with a  $2\theta$  range from 50 to 52 degrees. No significant peak is shown outside of this angle range.

Figures 6.1(c) and 6.1(d) show an atomic force microscopy (AFM) surface image and an X-ray diffraction (XRD) spectrum of the sample, respectively. The STEM images in Figs. 6.1(a) and 6.1(b) clearly indicate that the Pt layer manifests itself as a film with a smooth bottom surface and a rough top surface. The further analysis indicates that the Pt grains have an average lateral size of about 27 nm. In spite of the polycrystalline nature of the Pt layer and the rough Pt/YIG interface, however, the YIG layer is crystallized and exhibits a (111) orientation, as shown in Figs. 6.1(b) and 6.1(d), and the top surface of the YIG layer is very smooth, as shown in Figs. 6.1(a) and 6.1(c). Several notes should be made. First, prior to the annealing, the YIG film is amorphous as it is deposited at RT. The above results indicate that during the annealing the YIG film is well self-crystallized even though the bottom Pt layer is polycrystalline. This is similar with the previous work on Bi-doped YIG films, where amorphous films coated on glass

substrates become crystalline with a specific crystal orientation after the annealing.<sup>113</sup> the formation of the (111) texture is probably because the YIG lattice has a face-center-cubic structure in which the (111) plane is the most closely packed, and the (111) film has the lowest surface energy. Second, the analysis of the AFM data indicates that the YIG film surface has a rms roughness of about  $0.15 \pm 0.05$  nm. Third, the two-step Pt deposition process and the two annealing steps described above played important roles in the realization of the smooth YIG surface, and the latter is critical for achieving a high-quality interface if an additional NM or TI layer is grown on the top of the YIG layer. The necessity of the two-step Pt deposition as well as annealing processes are discussed along with control experiments in the next subsection.

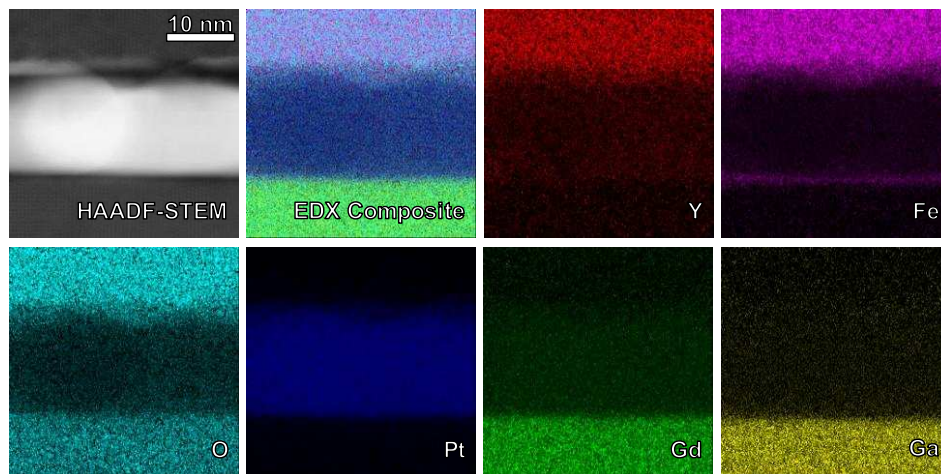


Figure 6.2. HAADF-STEM image (top-left) and corresponding EDX compositional maps. The composite intensity (atomic %) for individual-element maps has been rescaled for visibility.

Figure 6.2 presents the cross-section compositional maps measured with energy-dispersive X-ray spectroscopy (EDX). Except the one for Fe, the EDX maps all indicate very clear boundaries between the layers, suggesting very weak interfacial diffusion. In particular, the maps indicate that Pt, Ga, and Gd are all absent in the YIG layer, which is important for the realization of a high-quality YIG layer. Surprisingly, Fe is clearly present at the GGG/Pt interface, possibly

<sup>113</sup> A. Kirihaara, K. Uchida, Y. Kajiwara, M. Ishiba, Y. Nakamura, T. Manako, E. Saitoh, and S. Yoroazu, *Nature Mater.* **11**, 686 – 689 (2012).

due to the diffusion of Fe from the YIG layer through the Pt layer during the annealing. It is fortunate that the presence of Fe at the GGG/Pt interface does not affect the spin transfer across the Pt/YIG interface, although it may lead to Fe deficiency in the YIG film and prevent the realization of a YIG film with perfect quality. It will not play roles in the study of spin effects in Pt/YIG/NM or Pt/YIG/TI, if such tri-layered structures are fabricated. In addition to the EDX maps, EDX line scans across the 5 nm depth of the YIG film were also obtained. The data, presented in Fig. 6.3, indicate an atomic Y/Fe ratio of 3/5, which is the same as expected. The EDX results together with the XRD results shown in Fig. 6.1(d) confirm the composition of the YIG film and the absence of other oxide phases in the sample.

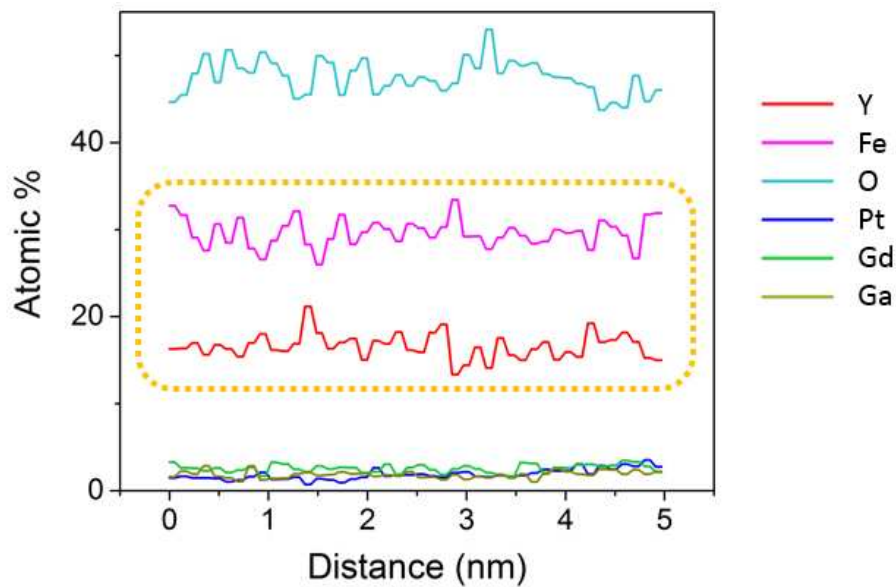


Figure 6.3. EDX data of the YIG/Pt/GGG sample which were measured across the randomly sampled 5 nm depth of the YIG layer. The horizontal axis shows the depth of the detection with 0 marking the top surface of the YIG layer. The vertical axis indicates atomic percentages.

Turn now to the magnetic properties of the YIG layer. Figure 6.4 presents the magnetic hysteresis responses measured by a vibrating sample magnetometer (VSM) using different fields, as indicated. The analysis of the data in Fig. 6.4(a) yields a coercivity of  $H_c \approx 20$  Oe and a saturation induction of  $4\pi M_s \approx 1.37$  kG. The analysis of the data in Fig. 6.4(b) indicates

$4\pi M_s \approx 1.575$  kG and a saturation field of about 1.518 kG. These values are compared with the corresponding values from the FMR and spin pumping measurements shortly.

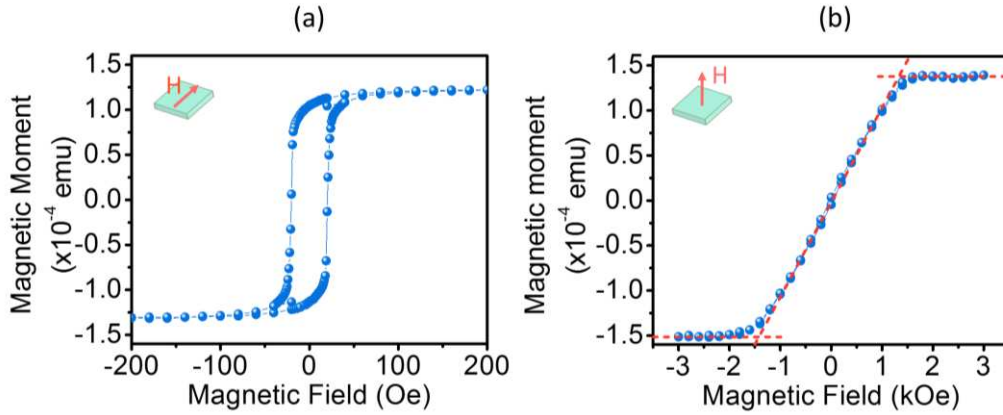


Figure 6.4. Static magnetic properties. (a) and (b) show the hysteresis loops measured by a vibrating sample magnetometer using different fields, as indicated. The sample size is 5 mm by 4 mm. The dashed lines in (b) indicates how the saturation field is determined.

Figure 6.5 presents FMR data measured with shorted  $X$ -band and  $K_u$ -band waveguide. Figures. 6.5(a) and (b) give the derivatives of the FMR power absorption for in-plane and out-of-plane fields, respectively. The circles show the data, while the red curves show the Lorentzian fits. The Lorentzian fitting-yielded FMR field ( $H_{\text{FMR}}$ ) and  $\Delta H$  data are presented in Figs. 6.5(c)-(f). In Figs. 6.5(c) and (d), the symbols show  $H_{\text{FMR}}$  as a function of frequency ( $f$ ), while the lines show the fits to the Kittel equations Eqs. 3.32 (b) & (a) for the field-in-plane and field-out-of-plane configurations, respectively. The  $|\gamma|$  and  $4\pi M_{\text{eff}}$  values indicated in Figs. 6.5(c) and (d) were obtained from the fitting. One can see that the two  $|\gamma|$  values are very close to each other, and they are also both close to the standard value (2.8 MHz/Oe).

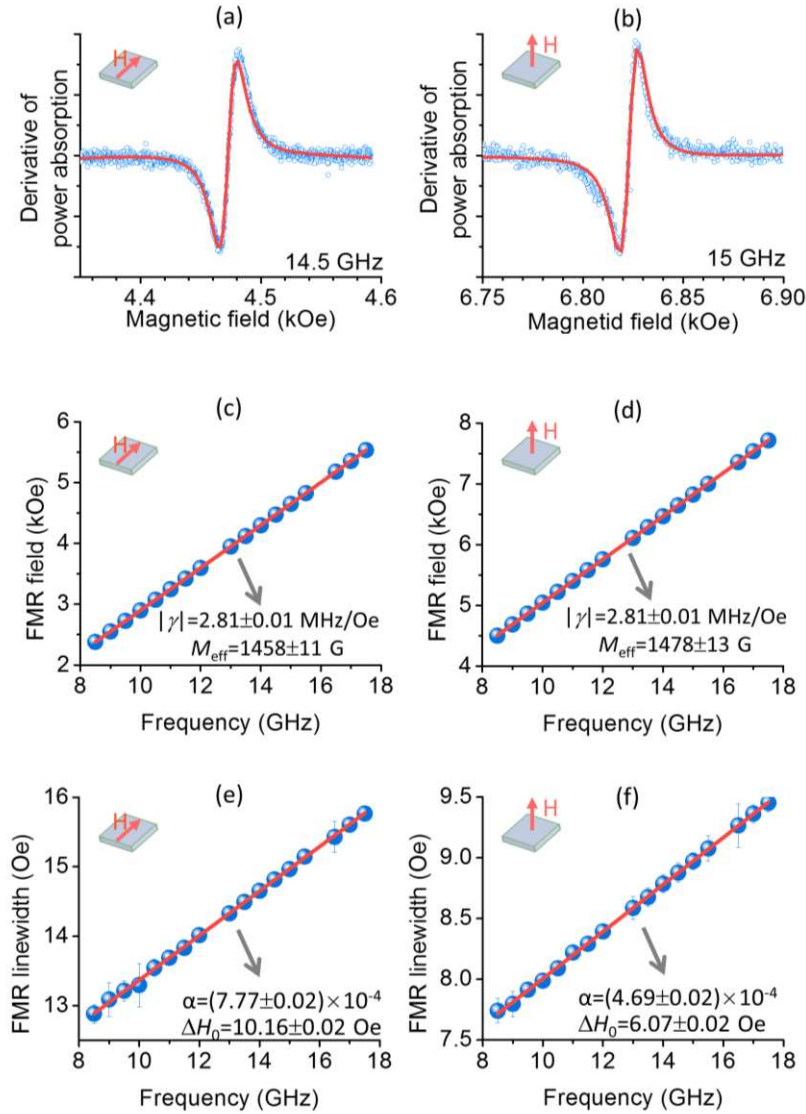


Figure 6.5. FMR properties. (a) and (b) present the FMR profiles measured with in-plane and out-of-plane fields, respectively. The circles show the data and the curves show the Lorentzian fits. (c) and (d) plot the Lorentzian fitting-yielded FMR field as a function of the frequency for two different field configurations, as indicated. (e) and (f) present the fitting-yielded FMR linewidth as a function of the frequency for different fields, as indicated. In (c)-(f), the symbols show the data, while the lines show the fits.

In Figs. 6.5(e) and 6.5(f), the symbols show  $\Delta H$  as a function of  $f$ , and the lines show fits to Eq. (3.45). The fitting-produced  $\alpha$  and  $\Delta H_0$  values are also given in Figs. 6.5(e) and 6.5(f). The data indicate three important results. First, the linewidth values are slightly larger than those of the films grown on GGG substrates<sup>10,12,77,93,112</sup> but are substantially smaller than the value

reported for the YIG films grown on Pt (about 358 Oe at 9 GHz).<sup>109</sup> Second, the  $\Delta H$  vs.  $f$  response in Fig. 6.5(e) show linear behavior over the entire frequency range, indicating that the two-magnon scattering is weak if it presents in the YIG film.<sup>74,75</sup> Third, the  $\alpha$  value for the field-in-plane configuration is notably larger than that for the field-out-of-plane configuration. This difference is mainly from the difference in spin pumping for the two field configurations. Previous theoretical work has showed that in ferromagnet/ non-magnetic metal bi-layers spin pumping-produced damping exhibits an anisotropic nature, being larger for in-plane fields than for out-of-plane fields.<sup>114</sup> Finally, considering that the damping constant of  $(4.69 \pm 0.03) \times 10^{-4}$  given in Fig. 6.5(f) contains a contribution from spin pumping, one can conclude that the actual damping of the YIG film should be smaller than  $(4.69 \pm 0.03) \times 10^{-4}$  and is therefore comparable to that of the YIG films grown on GGG substrates by PLD. The low  $\alpha$  values reported previously for the PLD films include  $2.3 \times 10^{-4}$ ,<sup>10,77</sup>  $2.2 \times 10^{-4}$ ,<sup>112</sup> and  $1.8 \times 10^{-4}$ .<sup>93</sup>

## 6.2.2 Discussion of the two-step Pt deposition and two-step annealing processes

In order to elaborate the necessity of the two-step Pt deposition process and the physics behind it, two control experiments were conducted and the results are shown as follows. We found that a Pt layer grown at 400 °C is a granular film, which will result in the YIG film deposited on the top also being granular after the annealing, as shown in the AFM image in Fig. 6.6(a). On the other hand, if the Pt and YIG layers are both deposited at room temperature, there will be high spikes after the annealing process, indicating a drastic stress release process. Those large spikes can be seen in Fig. 6.6(b).

---

<sup>114</sup> K. Chen and S. Zhang, Phys. Rev. Lett. **114**, 126602 (2015).

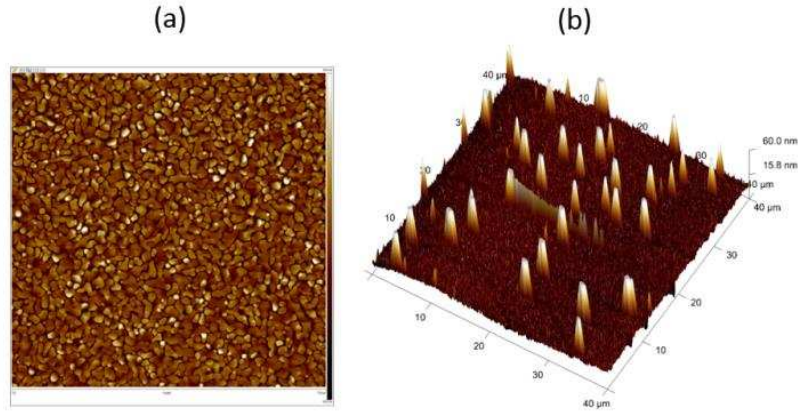


Figure 6.6. AFM surface morphology of (a) a Pt/GGG thin film sample deposited at 400 °C with no further annealing. (b) AFM surface image of a YIG/Pt/GGG sample with both the Pt and YIG layers deposited at room temperature and then annealed at 700 °C. The scan areas for (a) and (b) are 5 by 5  $\mu\text{m}^2$  and 40 by 40  $\mu\text{m}^2$ , respectively. The corresponding scale heights are -20 nm – 20 nm and -20 nm – 60 nm, respectively.

For this reason, we use a 2-step method to grow the Pt layer in order to make it easier to release stress and at the same time show a relatively smooth surface. We deposit a thin Pt layer at 400 °C first and then deposit further by RT sputtering. The first step serves to grow a thin Pt layer with relatively low stress and strong adhesion to the substrate, while the second ensures a relatively smooth surface needed by the subsequent YIG deposition. Based on the Pt growth rate and time, we estimated that the first and second Pt layers are 3 nm and 11 nm thick, respectively.

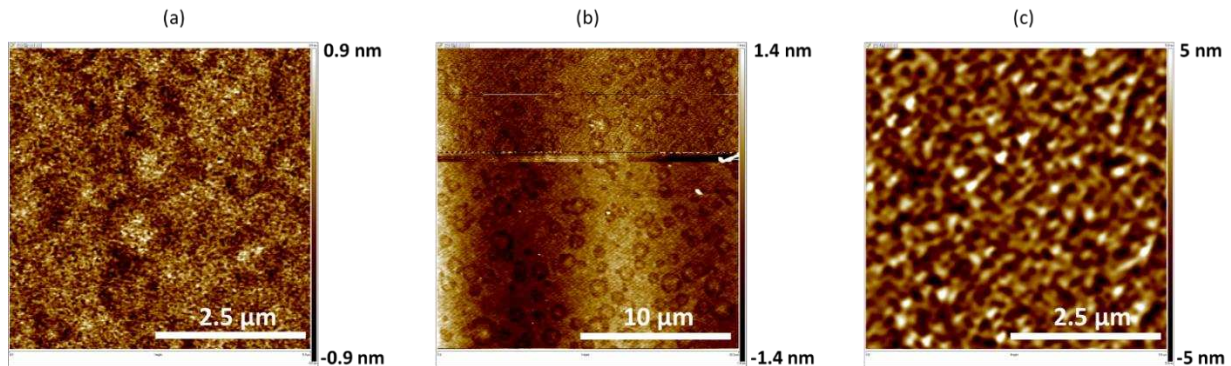


Figure 6.7. AFM surface images of YIG/Pt/GGG thin film samples prepared using different annealing parameters. (a) 650 °C for 90 min, (b) 700 °C for 30 min, and (c) 700 °C for 90 min.

Figure 6.7 shows the surface morphology of YIG/Pt/GGG samples fabricated using different annealing processes. If the sample is only annealed at a low temperature for relatively long time,

the sample surface can be smooth (see graph (a)) but the YIG layer cannot be crystallized and no FMR signal is detected. If the sample is directly annealed at a high temperature, the sample surface becomes pretty rough. For example, as shown in graph (b), bubble-like patterns form after annealing at 700 °C only for 30 minutes; the sample surface becomes even rougher if the sample is annealed at 700 °C for an even longer time (90 minutes), as shown in graph (c). These results indicate that the only possible understanding of the 2-step annealing process is that the Pt layer needs to firstly release the stress that is developed due to the thermal coefficient difference of the different layers, and at the same time the YIG film is relatively stable and maintains its smooth surface. After the stress is totally released in the Pt, the Pt layer becomes relatively stable and the temperature can be increased to crystallize the YIG film, which is the second annealing process.

### **6.3 Spin pumping at YIG/Pt interfaces**

The magnetic properties presented above clearly indicate that the YIG film grown on the Pt film exhibits high quality. They, however, do not speak for the quality of the YIG/Pt interface in terms of spin transfers. In this section spin pumping experiments were carried out to examine the interface quality. During the measurements, one drives the magnetization precession in the YIG by placing an end-shortened microstrip line on the top of the YIG film and feeding it with a microwave signal. The precession in the YIG layer pumps a spin current into the Pt layer that flows across the Pt thickness and produces an electrical voltage across the Pt lateral dimension via the inverse spin Hall effect (ISHE).<sup>83</sup>

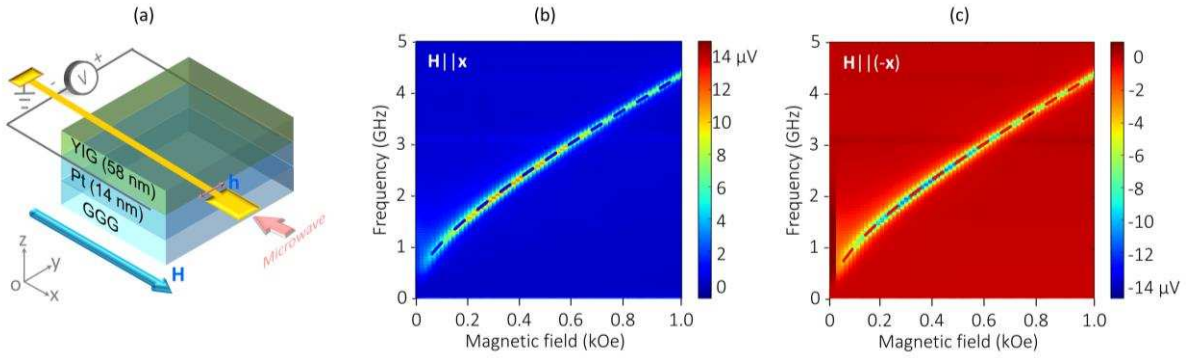


Figure 6.8. Spin pumping measurements. (a) Experimental setup. (b) and (c) present the spin pumping-produced electrical voltage (color) measured across the Pt length as a function of the external field (horizontal axis) and the microwave frequency (vertical axis) for different field directions, as indicated. The dashed curves show the fits to Eq. (3.32(b)).

Figure 6.8 presents the spin pumping data. Figure 6.8(a) sketches the experimental setup. Figure 6.8(b) presents a spin pumping signal map where the horizontal axis shows the strength of an external field applied along the  $+x$  direction, the vertical axis shows the frequency of the microwave signal applied to the microstrip line, and the color shows the ISHE voltage ( $V_{\text{ISHE}}$ ) measured across the Pt length (along the  $y$  axis). The blue dashed curve shows a fit to Eq. (3.32(b)), and the fitting used  $|\gamma| = 2.8 \text{ MHz/Oe}$  and took  $4\pi M_{\text{eff}}$  as the fitting parameter. Figure 6.8(c) shows the  $V_{\text{ISHE}}$  data measured in the same way as those shown in Fig. 6.8(b) except that the field was in an opposite direction (along the  $-x$  direction). As the blue dashed curve in Fig. 6.8(b), the red dashed curve in Fig. 6.8(c) also shows a fit to Eq. (3.32(b)). For both the measurements, the sample is 5.5 mm long and 2.5 mm wide, the microstrip line is 3.0 mm long and 50  $\mu\text{m}$  wide and has a nominal impedance of 50  $\Omega$ , and the microwave power applied to the microstrip line is about 100 mW.

Several results are evident from the data in Fig. 6.8. First, the  $V_{\text{ISHE}}$  signals are strong, indicating that the interface allows for efficient spin transfers. The signal strength is close to those measured with Pt/YIG/GGG samples. For example, measurements using a similar

experimental configurations yielded  $V_{\text{ISHE}}=10\text{-}50 \mu\text{V}$  for a Pt(8 nm)/YIG(20 nm)/GGG(0.5 mm) sample and  $V_{\text{ISHE}}\approx 24 \mu\text{V}$  for a Pt(14 nm)/YIG(58 nm)/GGG(0.5 mm) sample. Second, the reverse of the field direction leads to a flip in the voltage sign. This is consistent with the fact that in spin pumping the direction of the magnetization in the magnetic layer dictates the polarization of the spin current pumped into the non-magnetic layer.<sup>1,105</sup> Third, the voltage signal is the strongest at about 2 GHz, and this is true for both the field directions. It is known that the amplitude of the ISHE voltage is proportional to the strength of the spin current in the Pt, while the latter is proportional to  $\sin^2\theta$ , where  $\theta$  is the angle of the magnetization precession in the YIG (assuming a circular precession).<sup>115</sup> In the low-damping and small-angle approximations, the Gilbert equation yields

$$\sin\theta = \frac{1}{\alpha} \frac{f}{f^2 + [|\gamma|(H + 4\pi M_s)]^2} |\gamma| h \quad (6.1)$$

where  $h$  is the amplitude of the RF magnetic field and the field  $H$  changes with the frequency  $f$  according to the Kittel equation. Thus, one can write the peak voltage amplitude  $V_{\text{ISHE}}$  as a function of  $f$  as

$$V_{\text{ISHE}}(f) = C \frac{1}{\alpha^2} \left\{ \frac{f}{f^2 + [|\gamma|(H + 4\pi M_s)]^2} \right\}^2 \quad (6.2)$$

where  $C$  scales with the microwave power  $h^2$ , the spin mixing conductance at the interface, and the spin Hall angle in Pt. The frequency dependence of  $V_{\text{ISHE}}$  on  $f$  is not monotonic and it shows a maxima at 2 GHz.  $V_{\text{ISHE}}$  decreases as  $f$  is shifted away from the corresponding maxima. Lastly, the frequencies of the strongest voltage signals can be fitted nicely with Eq. (3.32(b)), as shown by the dashed curves in Figs. 6.8(b) and 6.8(c), indicating that the spin pumping is mainly associated with the quasi-FMR modes in the portion of the YIG film right beneath the microstrip

---

<sup>115</sup> O. Mosendz, V. Vlaminck, J. E. Pearson, F. Y. Fradin, G. E. W. Bauer, S. D. Bader, and A. Hoffmann, Phys. Rev. B, **82**, 214403, (2010).

line. The fitting yields  $4\pi M_{\text{eff}} = 1487$  G for the data in Fig. 6.8(b) and  $4\pi M_{\text{eff}} = 1486$  G for those in Fig. 6.8(c).

The spin mixing conductance is an important metric for spin transfer efficiency at YIG/Pt interfaces. For an estimate of spin mixing conductance on the YIG/Pt/GGG sample, it is assumed that the spin pumping process causes a damping enhancement in the YIG for the field-in-plane configuration but does not for the field out-of-plane configuration. Thus, for the out-of-plane configuration, the measured damping constant is approximately equal to the actual damping in the YIG film, namely,  $\alpha_{\perp} \approx \alpha_0$ . Then, the spin pumping-induced damping in the in-plane configuration can be estimated as  $\alpha_{\text{SP}} \approx \alpha_{//} - \alpha_0 \approx \alpha_{//} - \alpha_{\perp} = 0.000777 - 0.000469 = 0.000308$ . The spin mixing conductance can then be evaluated as

$$g_{\uparrow\downarrow} \approx \alpha_{\text{SP}} \frac{4\pi M_s}{g\mu_B} d_{\text{YIG}} = 3.08 \times 10^{-4} \frac{1546}{2.0 \times 9.274 \times 10^{-21}} \times 58 \times 10^{-7} \text{ cm}^{-2} \approx 1.5 \times 10^{14} \text{ cm}^{-2}$$

This value is comparable to the values reported previously for Pt/YIG/GGG samples, including

- $1.3 \times 10^{14} \text{ cm}^{-2}$  (experimental), Appl. Phys. Lett. **103**, 092404 (2013)
- $6.9 \times 10^{14} \text{ cm}^{-2}$  (experimental), Appl. Phys. Lett. **110**, 062402 (2017)
- $5 \times 10^{14} \text{ cm}^{-2}$  (theoretical), Phys. Rev. B **87**, 144411 (2013)

Note that the above-estimated spin mixing conductance is an underestimate because the damping in the out-of-plane configuration may also include a weak spin pumping contribution.<sup>114</sup>

Finally, several points should be made about the quality of the YIG film. First, the above-mentioned six saturation induction values obtained from the VSM, FMR, and spin pumping measurements are all within  $1.47 \pm 0.10$  kG, so they are reasonably close to each other. The small difference between those values may result from the VSM calibration error, the error in the YIG sample volume estimation, the slight misalignment of the fields in the FMR and spin pumping

measurements, and the presence of weak crystalline anisotropy in the YIG film, among other. Second, the similarity of those values suggests that there is no notable anisotropy in the YIG film. Note that the crystalline anisotropy field in single-crystal YIG bulk materials is usually several tens of Oe. Third, the average value 1.47 kG is about 16% lower than the well accepted bulk value (1.75 kG), and the reason for this big discrepancy is still unknown. The EDX analysis indicates that the YIG film has the right composition, but it is worth to confirm this using more sensitive techniques. Fourth, the RT electrical resistance measurements on a 120- $\mu\text{m}$ -long, 30- $\mu\text{m}$ -wide Hall bar structure made of a Pt(3.0 nm)/YIG(58.0 nm)/Pt(12.0 nm)/GGG(0.5 mm) sample (Sec. 6.4) indicate that the YIG film has a resistivity higher than  $1.4 \times 10^9 \Omega \cdot \text{m}$  at RT, indicating the electrical insulating nature of the YIG film. For a comparison, for the Pt/YIG/Pt structure reported in Ref. [110] the resistivity is significantly lower, about  $9.6 \times 10^5 \Omega \cdot \text{m}$  at 300 K and  $1.9 \times 10^7 \Omega \cdot \text{m}$  at 250 K. Finally, it is believed that it is possible to grow YIG thin films with similar quality on other metals rather than Pt as long as they have comparable or higher melting temperatures and have thermal expansion coefficients close to those of the substrate and the YIG.

## 6.4 Magnon-mediated current drag

The quality of the YIG/Pt interface in terms of spin transfers presented above clearly indicate that the YIG film grown on the Pt film exhibits high quality. In this section experiments on the magnon-mediated current drag effect were carried out to further examine the interface quality. A YIG(58 nm)/Pt(14 nm)/GGG sample is prepared with the fabrication method mentioned in Table 6.1. A 3-nm-thick top Pt layer is then deposited at room temperature.

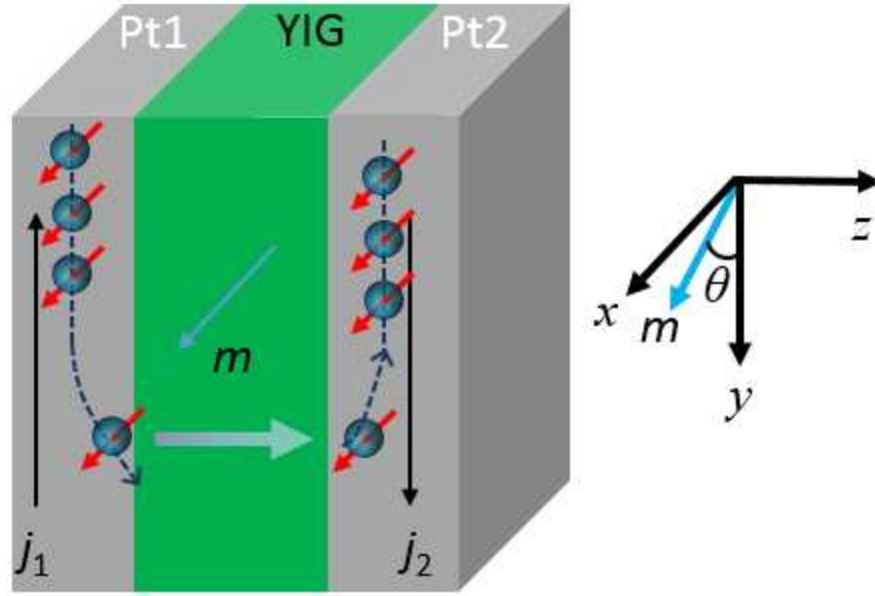


Figure 6.9. Schematic for magnon-mediated current drag effects. The  $x$  and  $y$  axes in the film plane are perpendicular and parallel to the current density respectively. The  $z$  axis is perpendicular to the film plane.

Figure 6.9 shows a schematic diagram for magnon-mediated current drag effects predicted by Zhang *et al.*<sup>111</sup> The ferromagnetic layer is magnetized along a direction indicated in Fig. 6.9. An electric current (density  $j_1$ ) flowing through the first nm-thick Pt layer Pt (left) will generate a transverse spin current via the spin Hall effect into the ferromagnetic YIG insulator layer with identical spin polarizations. Angular momenta are transferred at the Pt/YIG interface and carried by magnon/spin waves in the YIG. They are then transferred to the other YIG/Pt interface through spin-wave propagation and cause an angular momentum transfer again at the right interface to polarize spins of free electrons in the second Pt layer (right). The polarized electrons then diffuse along the thickness direction and generate a transverse electromotive force along the  $j_2$  direction as indicated in Fig. 6.9.

About this magnon-mediated current drag effect, three points should be emphasized. First, the direction of the output electric current  $j_2$  is always opposite to the input current  $j_1$ . Second, the magnitude of  $j_2$  is dependent on the direction of magnetization in the YIG layer. For the case of the magnetization perpendicular to the direction of  $j_1$ , the output magnitude is maximum,

while for the case of the magnetization parallel to  $j_1$ , the output magnitude is minimum and the current is suppressed. Third, the predicted efficiency  $\eta=j_2/j_1$  is approximately  $10^{-5}$  for a nm-thick YIG layer.

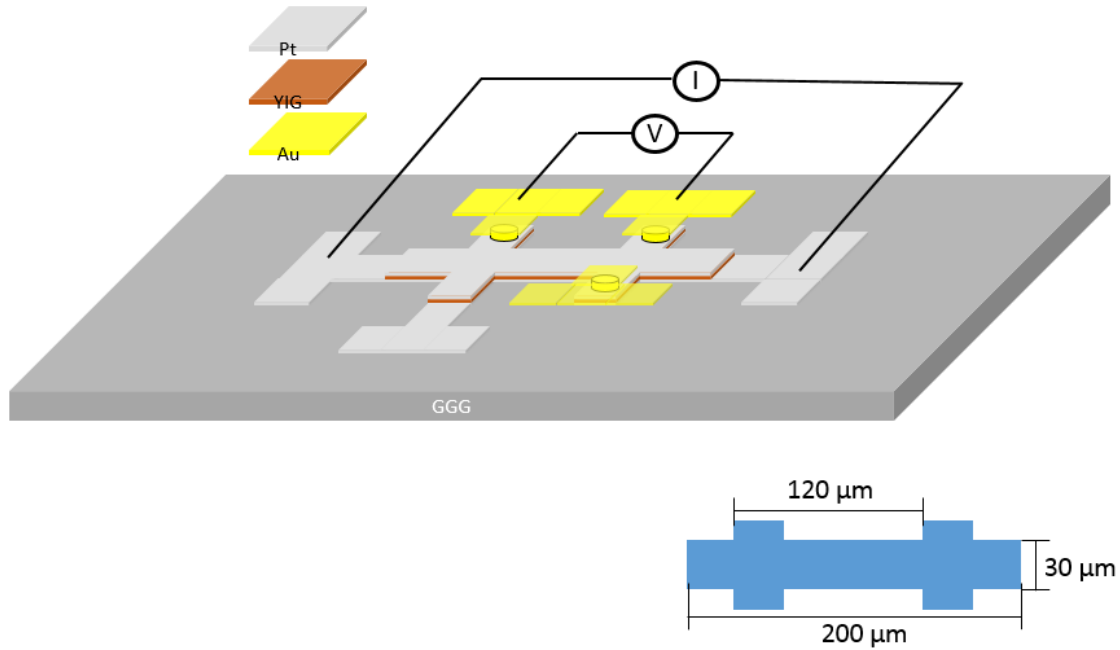


Figure 6.10. Patterned Pt/YIG/Pt sandwiched structure for magnon-mediated current drag measurements.

Figure 6.10 presents the patterned nanostructures for electric measurements. The bottom Pt layer (14 nm) is patterned with three T-shape electrodes extended out to bond to a current source, which is for the application of an electric current. The middle YIG layer (58 nm) is patterned with the lateral dimensions indicated in the bottom of Fig. 6.10. The top Pt layer (3 nm) is patterned to cover the YIG layer and extend three gold electrodes out for voltage detection. The thicknesses of the three layers are confirmed by TEM cross section imaging measurements.



Figure 6.11. A top view of the patterned Pt/YIG/Pt structure taken with an optical microscope.

Figure 6.11 shows the top view of the patterned Pt/YIG/Pt structure. The top two gold wires connect the top Pt layer to a voltage detector. The two side wires connect the bottom Pt layer to a current source. The YIG layer is magnetized to saturation by a constant magnetic field with a magnitude of 1 kOe.

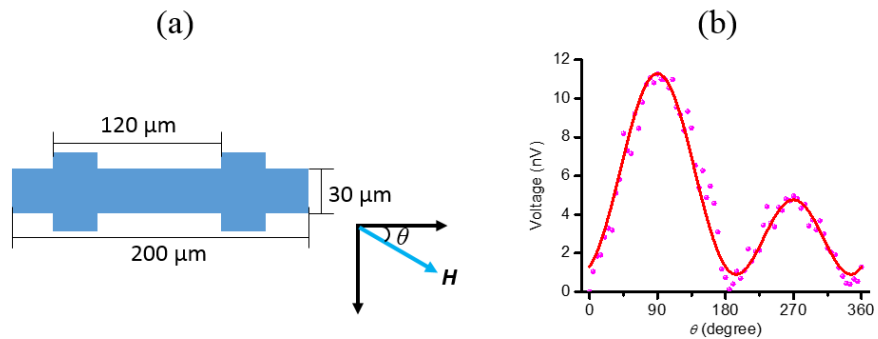


Figure 6.12. Magnon-mediated current drag measurements. (a) The top view of the patterned YIG layer and the angle between the external field and the horizontal direction. (b) The voltage data detected at 350 K using an input electric current of 10 mA. The dots show the data, while the red curve shows the fit.

Figure 6.12 shows the data of the magnon-mediated current drag measurements. Graph (a) shows the top view of the patterned structure and the field angle. Graph (b) shows the angle dependent voltage signal measured at 350 K using an input electric current of 10 mA. Three

points should be mentioned. First, the output voltage signal is maximum at 90 °C and 270 °C and suppressed at 0 °C and 180 °C. This is consistent with the theoretical prediction.<sup>111</sup> Second, though not shown here, the direction of the output electric current is opposite to the direction of the input electric current. Third, the voltage reaches 11 nV at 90 °C and 4 nV at 270 °C which is not equal. This is different from what the theory predicted and can be accounted by the spin Seebeck effect. A temperature gradient is generated through the thickness direction of the sandwiched structure due to the Joule heating of the bottom input electric current. Thus an unavoidable spin Seebeck signal is generated and superimposed onto the voltage signal of the magnon-mediated current drag effect. The angle dependences of the spin Seebeck signal and the magnon-mediated current drag signal are different and can be separated by fitting with

$$V = V_0 + V_{\text{SSE}} \sin \theta + V_{\text{Drag}} \sin^2 \theta \quad (6.3)$$

where  $V$  is the voltage signal measured,  $V_0$  is a constant background voltage signal,  $V_{\text{SSE}}$  is the magnitude of the voltage produced by the spin Seebeck effect, and  $V_{\text{Drag}}$  is the signal due to the magnon-mediated current drag effect. The fitting in Fig. 6.12(b) yields 3.26 nV for the SSE and 6.73 nV for the magnon-mediated current drag effect. The efficiency of this drag effect is then

$$\eta = \frac{j_2}{j_1} = \frac{I_2}{I_1} \frac{w_1 t_1}{w_2 t_2} = 2.1 \times 10^{-6}$$

The efficiency is on the same order of magnitude with the one reported by Li *et al*<sup>110</sup>, and both are one order of magnitude smaller than that predicted by Zhang *et al*<sup>111</sup>. This result may indicate that the more factors than those in in Ref [111] should be considered. It should be noted that the sandwiched Pt/YIG/Pt structure used here has a better quality than that used in Ref. [110], but the efficiencies are on the same order of magnitude. It indicates that the low efficiency may be irrelevant with the sample quality and other factors should be considered in the future.

## 6.5 Summary

In summary, this chapter demonstrates the sputtering growth of a Pt/YIG structure where the Pt layer was grown first and the YIG layer was then deposited on the top. The YIG layer shows well-oriented (111) texture, a surface roughness of 0.15 nm, and a damping constant less than  $4.7 \times 10^{-4}$ , and the YIG/Pt interface allows for efficient spin transfers as confirmed by the spin pumping and magnon-mediated current drag measurements. This demonstration indicates the feasibility of fabricating high-quality NM/YIG/NM tri-layered structures for new physics studies.

# CHAPTER 7

## SUMMARY AND OUTLOOK

The Experimental investigation and research have been carried out on high-quality yttrium iron garnet nanometer-thick film development on gadolinium gallium garnet insulator substrates as well as platinum metallic layers through magnetron sputtering techniques. Multiple methods were utilized for related thin film sample characterization on surface morphology, static and dynamic properties, microstructure as well as stoichiometry analysis. Besides, effects of multiple deposition parameters in sputtering techniques on thin film quality were investigated. Role of damping in spin Seebeck effect in the magnetic layer is investigated experimentally for the first time.

The last decade witnesses the increasing interest of utilizing yttrium iron garnet thin films in spintronics – related study and applications. The research topics and arguments in this dissertation provide a good reference for magnetic thin film development under annealing with magnetron sputtering techniques. Topics that are relevant to the studies in this dissertation and/or of great interest for future study may include the following:

- (1) Yttrium iron garnet thin film development on more metallic layers (Ta, W) or substrates (SiO<sub>2</sub>, sapphire)
- (2) Correlation between damping properties and microstructures of yttrium iron garnet
- (3) Nano patterning and applications to yttrium iron garnet based devices

# APPENDIX

## A. Derivation of Paschen's law

The objective of this appendix is to derive Paschen's law<sup>47</sup> and elucidate the mechanism of plasma ignition and the conditions for it to sustain for interested readers, though similar derivations exist in many textbooks.

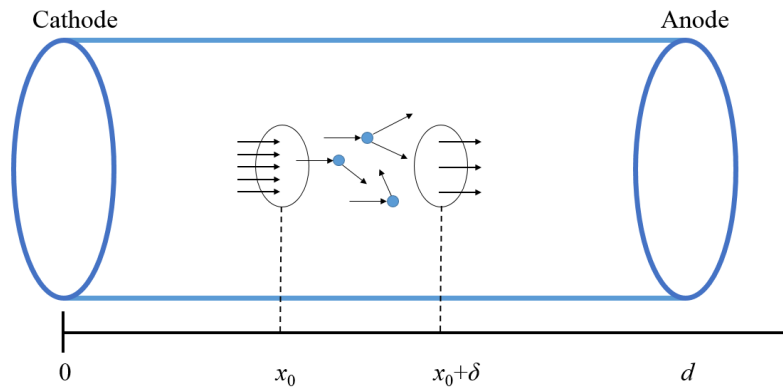


Figure A.1. Cartoon for the gas filled in a cylinder-like container. The blue dots show the neutral gas particle. The arrows indicate the flow direction of free electrons and scattering processes.

Assume gas (like argon, helium, neon, air) is sealed in a cylinder with a cathode and an anode at  $x=0$  and  $x=d$  respectively, as is shown in Fig. A.1. The use of the cylindrical shape here is to simplify the calculation and focus only on the physical process but not trivial algebra. If a voltage is applied and strong enough, an avalanche process will be triggered and the gas will breakdown and form plasma.

Initial ions are created with ionizing radiation, like cosmic rays. An original ionization event produce an ion pair, the positive ion and a free electron. The positive ion will fly to the cathode while the free electron will be accelerated under a big voltage towards the anode. If the electric field is strong enough, the free electron can gain sufficient energy to collide with and ionize a

neutral particle. This process will generate a new positive ion and a new free electron. The new free electron repeat the process and cause a chain reaction called Townsend avalanche. The number of collisions grows exponentially. Finally, all free electrons, if no supplement, will reach the anode and it cannot be sustained. In reality, however, there is supplement from the cathode. The ionized positive particles will also be accelerated and collide with the cathode. Due to its relatively big mass, there is a big chance that the ion will free an electron from the cathode. This process is called secondary emission. These secondary electrons are supplement to the free electrons and is critical for sustaining the plasma.

Assume that there is no current leaving or entering the vessel except through the electrodes. The continuity condition results in

$$j(0) = j(d) \quad (\text{A.1})$$

where  $j$  is the current density. Assuming a single ion species, like argon. Eq. A.1 can be rewritten as

$$j_e(0) + j_i(0) = j_e(d) + j_i(d) \quad (\text{A.2})$$

where subscripts  $e$  and  $i$  are for electrons and ions respectively. The increase of electron current density,  $j_e(x)$ , after passing a distance  $dx$ , is

$$dj_e(x) = j_e(x)\alpha dx$$

and  $\alpha$  is the ionization rate per unit length. The integration gives

$$j_e(x) = j_e(0)e^{\alpha x} \quad (\text{A.3})$$

In the cylindrical container there is no input of ions from the anode, so

$$j_i(d) = 0 \quad (\text{A.4})$$

Substituting Eq. A.3 and A.4 into Eq. A.2 results in

$$j_i(0) = j_e(0)(e^{\alpha d} - 1) \quad (\text{A.5})$$

Define  $\gamma$  as the probability of an ion releasing a secondary electron, then

$$\gamma = j_e(0) / j_i(0) \quad (\text{A.6})$$

Substitute Eq. A.6 into Eq. A.5 and we have

$$\alpha d = \ln(1 + 1/\gamma) \quad (\text{A.7})$$

Eq. A.7 is the first main results in this appendix. The ionization rate  $\alpha$  is not a measurable parameter and we have to connect it with the physical parameters that are easy to measure.

In statistical physics, we have

$$\lambda = \frac{1}{\sigma n} = \frac{k_B T}{\sigma p} \quad (\text{A.8})$$

where  $\lambda$  is the mean free path of a free electron,  $\sigma$  is the cross-section of the collision between a neutral particle and the electron.  $k_B$  is the Boltzmann constant.  $T$  is the temperature of the gas and  $p$  is the pressure.  $1/\lambda$  reflects the rate of collisions with a neutral particle per unit length along the cylindrical container. Once collided, the free electron will be lost. The change of the number of free electrons after travelling a distance  $dx$  is

$$dn_{free}(x) = -n_{free}(x) \frac{dx}{\lambda}$$

where  $n_{free}(x)$  is the number of free electrons at position  $x$ . Integrated, we have

$$\frac{n_{free}(x_0 + \delta)}{n_{free}(x_0)} = e^{-\delta/\lambda} \quad (\text{A.9})$$

where  $\delta$  is a small distance. The right-hand side of Eq. A.9 is independent of  $x_0$ . So at any point, the probability that a free electron has travelled a distance of at least  $\delta$  without collision is

$$P(\text{distance traveled} \geq \delta) = e^{-\delta/\lambda}$$

If each individual electron is sufficiently energetic, every collision will ionize the neutral particle so that

$$\alpha = \frac{1}{\lambda}$$

But this is not generally true. Only a portion of these electrons can ionize neutral particles.

Assume  $U_I$  is the minimum energy of a free electron to ionize a neutral particle, we have

$$\alpha = \frac{P(\text{electron with energy} \geq U_I)}{\lambda} \quad (\text{A.10})$$

Since the electric field accelerates the electrons, we have

$$\lambda_I = \frac{U_I d}{eV}$$

where  $\lambda_I$  is the minimum distance for an electron to gain  $U_I$ ,  $d$  is the length of the cylindrical container, and  $V$  is the electric potential between the electrodes. Here a uniform electric field distribution is assumed. Then, Eqn. (10) can be rewritten as

$$\alpha = \frac{P(\text{distance traveled} \geq \lambda_I)}{\lambda} = \frac{e^{-\lambda_I/\lambda}}{\lambda} \quad (\text{A.11})$$

Combine Eq. A.7, A.8, and A.11, we have

$$\ln(\ln(1+1/\gamma)) - \ln(Apd) = -\frac{Bpd}{V}$$

where  $A = \sigma/k_B T$  and  $B = U_I \sigma / e k_B T$ . Since  $V$  represents the voltage where breakdown just happens, we add a subscript BD and rearrange the equation above,

$$V_{BD} = \frac{Bpd}{\ln(Apd) - \ln(\ln(1+1/\gamma))} \quad (\text{A.12})$$

This is the Paschen's law.

## B. Derivation of one-dimensional model for atom deposition and dissociation

The objective of this appendix is to qualitatively explain the trapping and dissociation process of incident particles to substrates through a simple but effective one-dimensional chain model under harmonic approximation. For details and more discussion, please refer to Ref [49].

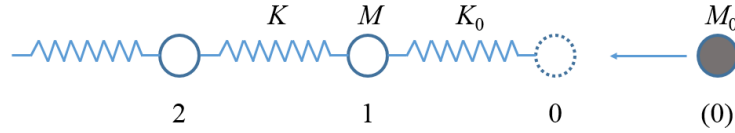


Figure B.1. Cartoon of one-dimensional linear chain model. The hollow spheres represent lattice particles in crystals and the shaded one represents the incident particle.

The schematic of the model is shown in Fig. B.1. The hollow spheres represent the ions (mass  $M$ ) in the crystal of substrates and they interact with the nearest neighbor through harmonic oscillation (force constant  $K$ ). The shaded sphere represents an incident atom with mass  $M_0$ . When the incident particle (0) arrives at position 0, it starts to interact with the first lattice particle and such interaction is described by a harmonic potential with a force constant  $K_0$  and an initial velocity  $\dot{r}_0(0)$ . The location of any particle  $n$  is indicated by the displacement  $r_n$  from its equilibrium position. The equations of motion, from Newton's second law, are

$$\begin{cases} M_0 \ddot{r}_0(t) = -K_0[r_0(t) - r_1(t)] & \text{(B.1)} \\ M_0 \ddot{r}_1(t) = K_0[r_0(t) - r_1(t)] - K[r_1(t) - r_2(t)] & \text{(B.2)} \\ M_0 \ddot{r}_n(t) = K[r_{n-1}(t) - 2r_n(t) + r_{n+1}(t)] & \text{(B.3)} \end{cases}$$

For simplicity, some variables and transformation are introduced as follows.

Mass ratio :  $\mu = M_0 / M$

Force constant ratio :  $\beta = K_0 / K$

Debye frequency :  $\omega_0 = 2\sqrt{K / M}$

Dimensionless time :  $\tau = \omega_0 t$

Relative displacement of neighboring particles from equilibrium :  $x_{2m+1}(\tau) = r_m(\tau) - r_{m+1}(\tau)$

Twice of the velocity of particle m :  $x_{2m}(\tau) = 2\dot{r}_m(\tau)$

Thus, we have

$$\frac{d\tau}{dt} = 2\sqrt{K / M}$$

$$\ddot{r}_0(t) = \frac{d^2 r_0}{dt^2} = \frac{d}{dt} \left( \frac{dr_0}{dt} \right) = \frac{d}{dt} \left( \frac{dr_0}{d\tau} \frac{d\tau}{dt} \right) = 2\sqrt{\frac{K}{M}} \frac{d}{dt} \left( \frac{dr_0}{d\tau} \right) = 2\sqrt{\frac{K}{M}} \ddot{r}_0(\tau) \frac{d\tau}{dt} = 4 \frac{K}{M} \ddot{r}_0(\tau)$$

By inserting all the equations above into Eq. B.1-3, one gets

$$\begin{cases} \dot{x}_0(\tau) = -\frac{\beta}{2\mu} x_1(\tau) \\ \dot{x}_2(\tau) = \frac{\beta}{2} x_1(\tau) - \frac{1}{2} x_3(\tau) \\ \dot{x}_{2n}(\tau) = \frac{1}{2} [x_{2n-1}(\tau) - x_{2n+1}(\tau)] \end{cases}$$

It seems that the RHS of the last equation above is only valid for even integers  $2n$ . However, based on the transformation relation,

$$\dot{x}_{2n+1}(\tau) = \dot{r}_n(\tau) - \dot{r}_{n+1}(\tau) = \frac{1}{2} [x_{2n}(\tau) - x_{2n+2}(\tau)]$$

So it is true for all integers but 0 and 2. Finally, the equations of motion, after transformation, are

$$\begin{cases} \dot{x}_0(\tau) = -\frac{\beta}{2\mu} x_1(\tau) \end{cases} \quad (\text{B.4})$$

$$\begin{cases} \dot{x}_2(\tau) = \frac{\beta}{2} x_1(\tau) - \frac{1}{2} x_3(\tau) \end{cases} \quad (\text{B.5})$$

$$\begin{cases} \dot{x}_n(\tau) = \frac{1}{2} [x_{n-1}(\tau) - x_{n+1}(\tau)] \quad n \neq 0, 2 \end{cases} \quad (\text{B.6})$$

The interest is on the relative displacement  $x_1(\tau)$  and velocity  $\dot{x}_1(\tau)$  between the incident

particle and the first particle in the chain as well as the absolute velocity of the incident particle  $x_0(\tau)$  evolved with time. With these solution, the connection between the kinetic energy of the incident particle, energy loss as well as trapping and dissociation conditions could be figured out. The next goal is to find a solution (analytical or serial) of  $x_1(\tau)$  and  $x_0(\tau)$ .

The first step is to find the differential equation which only contains  $x_1(\tau)$ . Differentiation of Eq. B.6 for  $n=1$  gives

$$\ddot{x}_1(\tau) = \frac{1}{2}\dot{x}_0(\tau) - \frac{1}{2}\dot{x}_2(\tau) = \frac{1}{2}\left(-\frac{\beta}{2\mu}\right)x_1(\tau) - \frac{1}{2}\left(\frac{\beta}{2}x_1(\tau) - \frac{1}{2}x_3(\tau)\right), \text{ or}$$

$$\ddot{x}_1(\tau) = -\frac{1}{4}\gamma x_1(\tau) + \frac{1}{4}x_3(\tau) \quad (\text{B.7})$$

where  $\gamma = \beta \frac{1+\mu}{\mu}$ . Now the problem is to remove  $x_3(\tau)$  from Eq. (B.7). Here the generating function method, introduced by Schrödinger<sup>116</sup> and by Rubin<sup>117</sup> is used to determine  $x_3(\tau)$  in terms of  $x_1(\tau)$  and the initial conditions.

The generating function is defined as

$$G(\rho, \tau) = \sum_{n \geq 1} x_n(\tau) \rho^n \quad (\text{B.8})$$

And the derivative of  $G(\rho, \tau)$  with respect to  $\tau$  is

$$\frac{\partial G(\rho, \tau)}{\partial \tau} = \sum_{n \geq 1} \dot{x}_n(\tau) \rho^n = \frac{1}{2} \sum_{\substack{n \geq 1 \\ n \neq 2}} [x_{n-1}(\tau) - x_{n+1}(\tau)] \rho^n + \left[\frac{\beta}{2} x_1(\tau) - \frac{1}{2} x_3(\tau)\right] \rho^2 \Rightarrow$$

$$\frac{\partial G(\rho, \tau)}{\partial \tau} = \frac{1}{2} x_0(\tau) \rho + \frac{1}{2} \sum_{n \geq 1} x_n(\tau) \rho^{n+1} - \frac{1}{2} \sum_{n \geq 1} x_n(\tau) \rho^{n-1} + \frac{1}{2} x_1(\tau) + \left[\frac{\beta}{2} x_1(\tau) - \frac{1}{2} x_3(\tau)\right] \rho^2 - \frac{1}{2} x_1(\tau) \rho^2 + \frac{1}{2} x_3(\tau) \rho^2 \Rightarrow$$

<sup>116</sup> E. Schrödinger, ANN. Physik **44**, 916 (1914).

<sup>117</sup> R. J. Rubin, Proceedings of the International Symposium on Transport Processes in Statistical Mechanics, held in Brussels, August 27-31, 1956 (Interscience Publishers, Inc., New York, 1958), p. 155.

$$\begin{aligned}\frac{\partial G(\rho, \tau)}{\partial \tau} &= \frac{1}{2} x_0(\tau) \rho + \frac{1}{2} \rho G(\rho, \tau) - \frac{1}{2\rho} G(\rho, \tau) + \frac{1}{2} x_1(\tau) + \frac{1}{2} (\beta - 1) x_1(\tau) \rho^2 \Rightarrow \\ \frac{\partial G(\rho, \tau)}{\partial \tau} &= \frac{1}{2} (\rho - \frac{1}{\rho}) G(\rho, \tau) + \frac{1}{2} x_0(\tau) \rho + \frac{1}{2} x_1(\tau) + \frac{1}{2} (\beta - 1) x_1(\tau) \rho^2\end{aligned}\quad (\text{B.9})$$

Here Eq. B.4 - 6 and Eq. B.8 are used. The general solution for the differential Eq. B.9 is

$$G(\rho, \tau) = \left\{ \int_0^\tau \left[ \frac{1}{2} x_0(s) \rho + \frac{1}{2} x_1(s) + \frac{1}{2} (\beta - 1) x_1(s) \rho^2 \right] e^{-\frac{1}{2}(\rho - \frac{1}{\rho})s} ds + C \right\} e^{\frac{1}{2}(\rho - \frac{1}{\rho})\tau}$$

Set  $\tau$  to zero, one gets  $C = G(\rho, 0)$ . So

$$G(\rho, \tau) = G(\rho, 0) e^{\frac{1}{2}(\rho - \frac{1}{\rho})\tau} + \frac{1}{2} \int_0^\tau \left[ x_1(s) + x_0(s) \rho - (1 - \beta) x_1(s) \rho^2 \right] e^{\frac{1}{2}(\rho - \frac{1}{\rho})(\tau - s)} ds \quad (\text{B.10})$$

Insert Eq. B.8 and the following series expansion into Eqn. B.10,

$$e^{\frac{1}{2}(\rho - \frac{1}{\rho})\tau} = \sum_{-\infty}^{\infty} J_n(\tau) \rho^n$$

where  $J_n(\tau)$  is the Bessel function. We get

$$\begin{aligned}\sum_{n \geq 1} x_n(\tau) \rho^n &= \left( \sum_{-\infty}^{\infty} J_m(\tau) \rho^m \right) \left( \sum_{k \geq 1} x_k(0) \rho^k \right) + \\ &\frac{1}{2} \int_0^\tau \left( \sum_{-\infty}^{\infty} J_q(\tau - s) \rho^q \right) \left[ x_1(s) + x_0(s) \rho - (1 - \beta) x_1(s) \rho^2 \right] ds\end{aligned}\quad (\text{B.11})$$

By comparing the coefficients of  $\rho^{2n+1}$  on the LHS and RHS of the Eq. B.11, we have

$$\begin{aligned}x_{2n+1}(\tau) &= \sum_{m \geq 1} x_m(0) J_{m-(2n+1)}(\tau) \cdot (-1)^{m-(2n+1)} + \\ &\frac{1}{2} \int_0^\tau \left[ J_{2n+1}(\tau - s) x_1(s) + J_{2n}(\tau - s) x_0(s) - (1 - \beta) J_{2n-1}(\tau - s) x_1(s) \right] ds\end{aligned}\quad (\text{B.12})$$

By comparing the coefficients of  $\rho^{-2n+1}$  on the LHS and RHS of Eq. B.11, we have

$$0 = \sum_{m \geq 1} x_m(0) J_{-(2n+1)-m}(\tau) + \frac{1}{2} \int_0^\tau \left[ J_{-2n+1}(\tau - s) x_1(s) + J_{-2n}(\tau - s) x_0(s) - (1 - \beta) J_{-2n-1}(\tau - s) x_1(s) \right] ds$$

The equation above could be simplified with the following properties of Bessel functions,

$$J_n(\tau) = \begin{cases} J_{-n}(-\tau) & \text{for } n \text{ even} \\ -J_{-n}(-\tau) & \text{for } n \text{ odd} \end{cases}$$

After simplification, we have

$$0 = \sum_{m \geq 1} x_m(0) J_{m+(2n-1)}(\tau) \cdot (-1)^{(-2n+1)-m} - \frac{1}{2} \int_0^\tau [-J_{2n-1}(\tau-s)x_1(s) + J_{2n}(\tau-s)x_0(s) + (1-\beta)J_{2n+1}(\tau-s)x_1(s)] ds \quad (\text{B.13})$$

By adding up the LHS and RHS of Eq. B.12 and 13 respectively, one gets

$$x_{2n+1}(\tau) = \sum_{m \geq 1} x_m(0) [J_{m+2n-1}(\tau) - J_{m-(2n+1)}(\tau)] \cdot (-1)^m + \frac{1}{2} \int_0^\tau \beta [J_{2n-1}(\tau-s) + J_{2n+1}(\tau-s)] x_1(s) ds \quad (\text{B.14})$$

Remember that for Bessel functions, we have the following recurrence relation

$$J_{\nu-1}(z) + J_{\nu+1}(z) = \frac{2\nu}{z} J_\nu(z)$$

Equation B.14 can be simplified as

$$x_{2n+1}(\tau) = \frac{\beta}{2} \int_0^\tau \frac{4n}{s} J_{2n}(s) x_1(\tau-s) ds - \sum_{m \geq 2} x_m(0) [J_{m-(2n+1)}(\tau) - J_{m+2n-1}(\tau)] \cdot (-1)^m \quad (\text{B.15})$$

Set  $n=1$ , we have

$$x_3(\tau) = 2\beta \int_0^\tau \frac{J_2(s)}{s} x_1(\tau-s) ds - \sum_{m \geq 2} x_m(0) [J_{m-3}(\tau) - J_{m+1}(\tau)] \cdot (-1)^m \quad (\text{B.16})$$

Now  $x_3(\tau)$  is represented by solely the variable  $x_1(\tau)$ . And the final differential equation for

$x_1(\tau)$ , by substituting Eq. B.16 into Eq. B.7, is

$$\ddot{x}_1(\tau) = -\frac{1}{4} \gamma x_1(\tau) + \frac{\beta}{2} \int_0^\tau \frac{J_2(s)}{s} x_1(\tau-s) ds - \sum_{m \geq 2} x_m(0) [J_{m-3}(\tau) - J_{m+1}(\tau)] \cdot (-1)^m \quad (\text{B.17})$$

If the lattice is initially at rest, then  $x_m(0) = 0$  for  $m > 1$ , the sum in Eq. B.17 is zero and

$$\ddot{x}_1(\tau) = -\frac{1}{4}\gamma x_1(\tau) + \frac{\beta}{2} \int_0^\tau \frac{J_2(s)}{s} x_1(\tau - s) ds \quad (\text{B.18})$$

The next step is to solve this differential-integral function Eq. B.18 for  $x_1(\tau)$ . Since there are Bessel functions in Eq. B.18, it is convenient to expand the solution as follows,

$$x_1(\tau) = x_1(0) \sum_{n \geq 0} a_{2n} J_{2n}(\tau) + 2\dot{x}_1(0) \sum_{n \geq 0} a_{2n+1} J_{2n+1}(\tau) \quad (\text{B.19})$$

By substituting the series expansion Eq. B.19 into Eq. B.18, one gets

$$\begin{aligned} x_1(0) \sum_{n \geq 0} a_{2n} \ddot{J}_{2n}(\tau) + 2\dot{x}_1(0) \sum_{n \geq 0} a_{2n+1} \ddot{J}_{2n+1}(\tau) = & -\frac{1}{4}\gamma \left[ x_1(0) \sum_{n \geq 0} a_{2n} J_{2n}(\tau) + 2\dot{x}_1(0) \sum_{n \geq 0} a_{2n+1} J_{2n+1}(\tau) \right] + \\ & \frac{\beta}{2} \int_0^\tau \frac{J_2(s)}{s} \left[ x_1(0) \sum_{n \geq 0} a_{2n} J_{2n}(\tau - s) + 2\dot{x}_1(0) \sum_{n \geq 0} a_{2n+1} J_{2n+1}(\tau - s) \right] ds \end{aligned} \quad (\text{B.20})$$

Both sides of Eq. B.20 need to be simplified for coefficients comparison. Note that

$$\begin{aligned} 2\dot{J}_n(z) &= J_{n-1}(z) - J_{n+1}(z) \Rightarrow \\ \ddot{J}_n(\tau) &= \left( \frac{\dot{J}_{n-1}(\tau) - \dot{J}_{n+1}(\tau)}{2} \right) = \frac{1}{4} [J_{n-2}(\tau) - 2J_n(\tau) + J_{n+2}(\tau)] \quad (J_k(\tau) = 0 \text{ if } k < 0) \end{aligned}$$

Then the LHS of Eq. B.20 is simplified as

$$x_1(0) \sum_{n \geq 0} a_{2n} \cdot \frac{1}{4} [J_{2n-2}(\tau) - 2J_{2n}(\tau) + J_{2n+2}(\tau)] + 2\dot{x}_1(0) \sum_{n \geq 0} a_{2n+1} \cdot \frac{1}{4} [J_{2n-2}(\tau) - 2J_{2n+1}(\tau) + J_{2n+3}(\tau)]$$

Note we have the following integral formula

$$\int_0^\tau \frac{J_p(s) J_q(\tau - s)}{s} ds = \frac{J_{p+q}(\tau)}{p} \text{ for } \text{Re}[p] > 0 \text{ and } \text{Re}[q] > -1$$

Then the RHS of Eq. B.20 is

$$-\frac{1}{4}\gamma \left[ x_1(0) \sum_{n \geq 0} a_{2n} J_{2n}(\tau) + 2\dot{x}_1(0) \sum_{n \geq 0} a_{2n+1} J_{2n+1}(\tau) \right] + \frac{\beta}{2} x_1(0) \sum_{n \geq 0} a_{2n} \frac{J_{2n+2}(\tau)}{2} + \beta \dot{x}_1(0) \sum_{n \geq 0} a_{2n+1} \frac{J_{2n+3}(\tau)}{2}$$

With some simply algebra, we have, from Eq. B.20,

$$\begin{aligned} & \frac{x_1(0)}{4} \sum_{n \geq 0} [a_{2n} J_{2n-2}(\tau) + (\gamma - 2)a_{2n} J_{2n}(\tau) + (1 - \beta)a_{2n} J_{2n+2}(\tau)] \\ & + \frac{\dot{x}_1(0)}{2} \sum_{n \geq 0} [a_{2n+1} J_{2n-1}(\tau) + (\gamma - 2)a_{2n+1} J_{2n+1}(\tau) + (1 - \beta)a_{2n+1} J_{2n+3}(\tau)] = 0 \end{aligned}$$

$x_1(\tau)$  and  $\dot{x}_1(\tau)$  are independent, then one gets

$$\begin{aligned} & \sum_{n \geq 0} [a_{2n} J_{2n-2}(\tau) + (\gamma - 2)a_{2n} J_{2n}(\tau) + (1 - \beta)a_{2n} J_{2n+2}(\tau)] = 0 \\ & \sum_{n \geq 0} [a_{2n+1} J_{2n-1}(\tau) + (\gamma - 2)a_{2n+1} J_{2n+1}(\tau) + (1 - \beta)a_{2n+1} J_{2n+3}(\tau)] = 0 \end{aligned}$$

Rearrange  $n$  according to  $J_n(\tau)$ , we have

$$\begin{cases} a_{2n+2} + (\gamma - 2)a_{2n} + (1 - \beta)a_{2n-2} = 0 & \text{for } n > 1 \\ a_{2n+3} + (\gamma - 2)a_{2n+1} + (1 - \beta)a_{2n-1} = 0 & \text{for } n > 0 \end{cases}$$

So the recursion relations for the coefficients are

$$\begin{cases} a_2 + (\gamma - 2)a_0 = 0 & \text{(B.21a)} \\ a_3 + (\gamma - 3)a_1 = 0 & \text{(B.21b)} \\ a_4 + (\gamma - 2)a_2 + (2 - \beta)a_0 = 0 & \text{(B.21c)} \\ a_n + (\gamma - 2)a_{n-2} + (1 - \beta)a_{n-4} = 0 & \text{for } n > 4 \quad \text{(B.21d)} \end{cases}$$

Once the values of  $a_0$  and  $a_1$  are determined, the numerical solution of  $x_1(\tau)$  could be found. Further, the relative displacement from equilibrium for any two adjacent lattice atoms could also be found with Eq. B.15 and the solution of  $x_1(\tau)$ , which is

$$x_{2n+1}(\tau) = \beta \left[ x_1(0) \sum_{m \geq 0} a_{2m} J_{2(m+n)}(\tau) + 2\dot{x}_1(0) \sum_{m \geq 0} a_{2m+1} J_{2(m+n)+1}(\tau) \right] \quad \text{(B.22)}$$

One of the useful quantities is the twice of the velocity of the incident particle,

$$x_0(\tau) = x_0(0) - \frac{\beta}{2\mu} \int_0^\tau x_1(s) ds$$

By substituting the solution of  $x_1(\tau)$  and note that  $x_0(0) = 2\dot{x}_1(0)$ , we have

$$\frac{x_0(\tau)}{x_0(0)} = 1 - \frac{\beta}{\mu} \left[ \frac{x_1(0)}{2\dot{x}_1(0)} \sum_{n \geq 0} \sum_{m \geq 0} a_{2n} J_{2(n+m)+1}(\tau) + \sum_{n \geq 0} \sum_{m \geq 0} a_{2n+1} J_{2(n+m+1)}(\tau) \right] \quad (\text{B.23})$$

Now all the quantities necessary for calculation are determined. The values of  $a_0$  and  $a_1$  need to be determined. These could be acquired by setting  $\tau=0$  in Eq. B.19, we have  $a_0 = 1$ .

Then taking the first derivative of Eq. B.19 and setting  $\tau=0$  leads to  $a_1 = 1$ .

For the specific interest in fabrication of YIG on GGG substrates, though there are compound elements, each individual element in YIG has a smaller atomic mass than that in GGG. Then the mass ratio  $\mu$  interested resides in interval  $[0, 1]$ . The interaction between the incident particle and the ions at the lattice surface should be weaker than that between the lattice ions. The force constant ratio  $\beta$  interested is within  $[0, 1]$ . Mathematically, the series acquired from the recursion relation of Eq. B.21, however, is not always bounded. For  $\mu$  in  $[0, 1]$ , the series will diverge with a bigger  $\beta$  value. Luckily, Eq. B.19 is still valid as each product term of the coefficient and the Bessel function gives a finite value and this series is convergent.

## **C. One dimensional collision model programs for data analysis and graph depiction**

In this appendix, programs of the one-dimensional linear chain atomic collision model are provided for interested readers. Programs are based on Python 3.

#####

#Program 1 for Fig. 2.8 and 2.9 in the main text

```

#####
import numpy                #module for array-type data
from scipy import special   #module containing bessel functions of the first kind
import matplotlib.pyplot as plt #graph drawing package
#####
#global input variables
#####
#N length of series used for calculation
#miu relative mass
#beta relative force constant
#z=2x'1(0)/x1(0), twice the incident particle's velocity scaled to x1(0)
#tao_max the max time of the time interval
#step the time step
N=248
miu=0.25
beta=0.8
z=-1.0 #close to critical value
tao_max=50
step=0.1
tao=numpy.arange(0,tao_max,step) #tao descreted time intervals
Nt=len(tao) #Nt number of descreted tao
numpy.savetxt('tao.txt',tao)
#####

```

```

#function for coefficients calculation
#####

#N length of series used for calculation

#miu relative mass

#beta relative force constant

def coefficients(N,miu,beta):          #input N, miu, beta

    gamma=beta*(1.0+miu)/miu         #calculate gamma

    a=numpy.zeros(N+1)               #generate an array from 0 to N filled with zero

    a[0]=1.0

    a[1]=1.0

    a[2]=a[0]*(2-gamma)

    a[3]=a[1]*(3-gamma)

    a[4]=a[0]*(beta-2)+a[2]*(2-gamma) #calculate a0 to a4

    for i in range(5,N+1):

        a[i]=a[i-4]*(beta-1)+a[i-2]*(2-gamma) #calculate a5 to aN

    return a

a=coefficients(N,miu,beta)

print(a)

#####

#x1(t): relative displacement between the incident and first particles,

#corresponding to x1(t)/x1(0) in the equation.

#####

x1=numpy.zeros(Nt)

```

```

for i in range(Nt):
    j=0
    while 2*j<=N:
        x1[i]+=a[2*j]*special.jn(2*j,tao[i])
        j+=1
    j=0
    while 2*j+1<=N:
        x1[i]+=z*a[2*j+1]*special.jn(2*j+1,tao[i])
        j+=1
numpy.savetxt('x1.txt',x1)

#####
#x3(t): relative displacement between the and first and second particles in
#the lattice, corresponding to x3(t)/x1(0) in the equation.
#####

x3=numpy.zeros(Nt)
for i in range(Nt):
    j=0
    while 2*j<=N:
        x3[i]+=beta*a[2*j]*special.jn(2*j+2,tao[i])
        j+=1
    j=0
    while 2*j+1<=N:
        x3[i]+=beta*z*a[2*j+1]*special.jn(2*j+3,tao[i])

```

```

        j+=1
numpy.savetxt('x3.txt',x3)

#####

#x5(t): relative displacement between the second and third particles in
#the lattice, corresponding to x5(t)/x1(0) in the equation.

#####

x5=numpy.zeros(Nt)
for i in range(Nt):
    j=0
    while 2*j<=N:
        x5[i]+=beta*a[2*j]*special.jn(2*j+4,tao[i])
        j+=1
    j=0
    while 2*j+1<=N:
        x5[i]+=beta*z*a[2*j+1]*special.jn(2*j+5,tao[i])
        j+=1
numpy.savetxt('x5.txt',x5)

#####

#x7(t): relative displacement between the third and fourth particles in
#the lattice, corresponding to x7(t)/x1(0) in the equation.

#####

x7=numpy.zeros(Nt)
for i in range(Nt):

```

```

j=0
while 2*j<=N:
    x7[i]+=beta*a[2*j]*special.jn(2*j+6,tao[i])
    j+=1
j=0
while 2*j+1<=N:
    x7[i]+=beta*z*a[2*j+1]*special.jn(2*j+7,tao[i])
    j+=1

numpy.savetxt('x7.txt',x7)

#####
#x9(t): relative displacement between the fourth and fifth particles in
#the lattice, corresponding to x9(t)/x1(0) in the equation.
#####

x9=numpy.zeros(Nt)
for i in range(Nt):
    j=0
    while 2*j<=N:
        x9[i]+=beta*a[2*j]*special.jn(2*j+8,tao[i])
        j+=1
    j=0
    while 2*j+1<=N:
        x9[i]+=beta*z*a[2*j+1]*special.jn(2*j+9,tao[i])
        j+=1

```

```

numpy.savetxt('x9.txt',x9)

#####

#x'1(t): the first derivative of x1(t)

#####

x11=numpy.zeros(Nt)

for i in range(Nt):

    j=0

    while 2*j<=N:

        x11[i]+=a[2*j]*special.jvp(2*j,tao[i],1)

#jvp(m,x,n), the nth derivative of mth order bessel function of the first kind with respect to x

        j+=1

    j=0

    while 2*j+1<=N:

        x11[i]+=z*a[2*j+1]*special.jvp(2*j+1,tao[i],1)

        j+=1

numpy.savetxt('x'1.txt',x11)

plt.plot(tao,x1,tao,x3,tao,x5,tao,x7,tao,x9)

plt.show()

plt.plot(tao,x1,tao,x11)

plt.show()

#####

#Program 2 for Fig. 2.10.

#####

```

```

import numpy                #module for array-type data
from scipy import special   #module containing bessel functions of the first kind
import matplotlib.pyplot as plt #graph drawing package

#####

#global input variables

#####

#N: initial length of series used for calculatioin

#miu: relative mass

#miu_min: minimum value of miu

#miu_max: maximum value of miu

#step_miu: the miu step

#beta: relative force constant

#beta_min: minimum value of beta

#beta_max: maximum value of beta

#step_beta: the beta step

#z=2x'1(0)/x1(0), twice the incident particle's velocity scaled to x1(0)

#tao_max the max time of the time iterval

#step the time step

N=500

miu_min=0.1

miu_max=1.01

step_miu=0.01

miu=numpy.arange(miu_min,miu_max,step_miu)

```

```

Nmiu=len(miu)                #Nmiu number of descreted miu
beta_min=0.1
beta_max=1.01
step_beta=0.01
beta=numpy.arange(beta_min,beta_max,step_beta)
Nbeta=len(beta)              #Nbeta number of descreted beta
tao_max=50
step=0.2
tao=numpy.arange(0,tao_max,step) #tao descreted time intervals
Nt=len(tao)                  #Nt number of descreted tao
z=numpy.arange(0,-100,-0.5)  #coarse searching area of z
Nz=len(z)

#####
#function for coefficients calculation
#####
#N length of series used for calculatioin
#miu relative mass
#beta relative force constant
def coefficients(N,miu_a,beta_a):    #input N, miu, beta
    gamma_a=beta_a*(1+miu_a)/miu_a #calculate gamma
    b=numpy.zeros(N+1)              #generate an array from 0 to N filled with zero
    b[0]=1
    b[1]=1

```

```

b[2]=b[0]*(2-gamma_a)

b[3]=b[1]*(3-gamma_a)

b[4]=b[0]*(beta_a-2)+b[2]*(2-gamma_a)           #calculate a0 to a4

for i in range(5,N+1):

    b[i]=b[i-4]*(beta_a-1)+b[i-2]*(2-gamma_a)     #calculate a5 to aN

    if abs(b[i])<=0.00001 and i>=200:

        break

    return i,b           #i is the ith coefficient that first smaller than 0.0001.

#####

#File I/O

#####

f=open('critical z with respect to miu and beta.txt','a')

f.write('miu\tbeta\tz(velocity)\ttauo(critical time)\tx1(position)\tx11(velocity)\n')

f.close()

#####

#For each set of (miu,beta), find z that satisfies x1(tc)=0 & x11(tc)=0

#x1(t): relative displacement between the incident and first particles

#x11(t): velocity of x1(t)

#####

for m in range(Nmiu):

    for b in range(Nbeta):

        N_flexible, a=coefficients(N,miu[m],beta[b])

        #coefficients caculation;N_flexible is the number of terms used with accuracy 0.0001

```

```

print('*****')

print('Start:miu=',miu[m],'beta=',beta[b])

print('coefficients calculation done with',N_flexible,'terms')

print('*****')

k=1

while k <= Nz:

    for i in range(1,Nt):

        x11_left=0.0

        x11_right=0.0

        j=0

        while 2*j+1<=N_flexible:

            x11_left+=a[2*j]*special.jvp(2*j,tao[i],1)\

            +z[k]*a[2*j+1]*special.jvp(2*j+1,tao[i],1)

#calculation of two neighboring deivatives in time

            x11_right+=a[2*j]*special.jvp(2*j,tao[i+1],1)\

            +z[k]*a[2*j+1]*special.jvp(2*j+1,tao[i+1],1)

            j+=1

        if x11_left>0 and x11_right<0

#find a coarse interval containing the critical time

            min_interval=tao[i]

            max_interval=tao[i+1]

            q=(min_interval+max_interval)/2.0

            break

        print('timeintervalfound.min_t=',min_interval,\

```

```

max_t='max_interval','z'=z[k])

x11=0

j=0

while 2*j+1<=N_flexible:

    x11+=a[2*j]*special.jvp(2*j,q,1)\
    +z[k]*a[2*j+1]*special.jvp(2*j+1,q,1)

    j+=1

print('x11=',x11)

while abs(x11)>0.0001:

    if x11>0:

        min_interval=q

    elif x11<0:

        max_interval=q

    q=(max_interval+min_interval)/2.0

    j=0

    x11=0

    while 2*j+1<=N_flexible:

        x11+=a[2*j]*special.jvp(2*j,q,1)\
        +z[k]*a[2*j+1]*special.jvp(2*j+1,q,1)

#find the critical time that makes x11==0

    j+=1

x1=0

j=0

```

```

while 2*j+1<=N_flexible:
    x1+=a[2*j]*special.jn(2*j,q)\
    +z[k]*a[2*j+1]*special.jn(2*j+1,q)
    j+=1
if x1-1<0:
    min_z=z[k]
    k+=1
elif x1-1>0:
    max_z=z[k]
#find the z interval that have x1=1 at the critical time
    break
mean_z=(min_z+max_z)/2.0
print('initial mean_z found',mean_z,'\n')
while abs(x1-1)>0.0001:
    for i in range(1,Nt):
        x11_left=0.0
        x11_right=0.0
        j=0
        while 2*j+1<=N_flexible:
            x11_left+=a[2*j]*special.jvp(2*j,tao[i],1)\
            +mean_z*a[2*j+1]*special.jvp(2*j+1,tao[i],1)
#calculation of two neighboring deivatives in time
            x11_right+=a[2*j]*special.jvp(2*j,tao[i+1],1)\

```

```

        +mean_z*a[2*j+1]*special.jvp(2*j+1,tao[i+1],1)
        j+=1
    if x11_left>0 and x11_right<0:
#find a coarse interval containing the critical time
        min_interval=tao[i]
        max_interval=tao[i+1]
        q=(min_interval+max_interval)/2
        break
x11=0
j=0
while 2*j+1<=N_flexible:
    x11+=a[2*j]*special.jvp(2*j,q,1)\
    +mean_z*a[2*j+1]*special.jvp(2*j+1,q,1)
    j+=1
while abs(x11)>0.0001:
    if x11>0:
        min_interval=q
    elif x11<0:
        max_interval=q
    q=(max_interval+min_interval)/2
    j=0
    x11=0
    while 2*j+1<=N_flexible:

```

```

x11+=a[2*j]*special.jvp(2*j,q,1)\
+mean_z*a[2*j+1]*special.jvp(2*j+1,q,1)

#find the critical time that makes x11==0

j+=1

x1=0

j=0

while 2*j+1<=N_flexible:

    x1+=a[2*j]*special.jn(2*j,q)\
+mean_z*a[2*j+1]*special.jn(2*j+1,q)

    j+=1

if x1-1<0:

    min_z=mean_z

elif x1-1>0:

    max_z=mean_z

mean_z=(min_z+max_z)/2

print('results found! miu=',miu[m],'\tbeta=',beta[b],\
\tz=',mean_z,'\ttau=',q,'x1=',x1,'\tx11=',x11)

f=open('critical z with respect to miu and beta.txt','a')

f.write(str(miu[m]))

f.write('\t')

f.write(str(beta[b]))

f.write('\t')

f.write(str(mean_z))

```

```

f.write('\t')
f.write(str(q))
f.write('\t')
f.write(str(x1))
f.write('\t')
f.write(str(x11))
f.write('\n')
f.close()

```

```
f.close()
```

```
input('All calculation done! Press any key.')
```

## D. Derivation of the Green's function tensor of the dipole field

The Maxwell equations and the magneto-static approximation<sup>36</sup> provides

$$\begin{cases} \vec{\nabla} \times \vec{h}_d = 0 \\ \vec{\nabla} \cdot (\vec{h}_d + 4\pi\vec{m}(\xi)e^{-ik_\zeta\zeta}) = 0 \end{cases} \quad \begin{matrix} \text{(D.1a)} \\ \text{(D.1b)} \end{matrix}$$

where  $\vec{h}_d$  is the dipole field acting on the local magnetization  $\vec{m}$ . A spin wave propagating along  $\zeta$  direction with a wavelength  $k_\zeta$  and a single frequency is assumed here. With some simple algebra, Eq. D.1a and D.1b can be combined into the following differential equation

$$\nabla^2 \vec{h}_d = -4\pi\vec{\nabla}(\vec{\nabla} \cdot \vec{m}(\xi)e^{-ik_\zeta\zeta}) \quad \text{(D.2)}$$

All the vectors are in the  $(\zeta, \eta, \xi)$  coordinate system. By decomposing the dipole field along the three directions, three Poisson's equations are acquired from Eq. D.2,

$$\left\{ \begin{array}{l} \nabla^2 h_{d_\xi} = -4\pi \left( \frac{\partial^2 m_\xi(\xi)}{\partial \xi^2} - ik_\xi \frac{\partial m_\xi(\xi)}{\partial \xi} \right) e^{-ik_\xi \zeta} \end{array} \right. \quad (\text{D.3a})$$

$$\left\{ \begin{array}{l} \nabla^2 h_{d_\eta} = 0 \end{array} \right. \quad (\text{D.3b})$$

$$\left\{ \begin{array}{l} \nabla^2 h_{d_\zeta} = -4\pi \left[ -ik_\zeta \left( \frac{\partial m_\xi(\xi)}{\partial \xi} - ik_\xi m_\xi(\xi) \right) \right] e^{-ik_\zeta \zeta} \end{array} \right. \quad (\text{D.3c})$$

where the subscripts indicate vector components in the  $(\xi, \eta, \zeta)$  coordinate system. The solutions for the three Poisson's equations are

$$\left\{ \begin{array}{l} h_{d_\xi} = \iiint_V \frac{1}{|\vec{x} - \vec{x}'|} \left( \frac{\partial^2 m_\xi(\xi')}{\partial \xi'^2} - ik_\xi \frac{\partial m_\xi(\xi')}{\partial \xi'} \right) e^{-ik_\xi \zeta'} d\xi' d\eta' d\zeta' \end{array} \right. \quad (\text{D.4a})$$

$$\left\{ \begin{array}{l} h_{d_\eta} = 0 \end{array} \right. \quad (\text{D.4b})$$

$$\left\{ \begin{array}{l} h_{d_\zeta} = \iiint_V \frac{-ik_\zeta}{|\vec{x} - \vec{x}'|} \left( \frac{\partial m_\xi(\xi')}{\partial \xi'} - ik_\xi m_\xi(\xi') \right) e^{-ik_\zeta \zeta'} d\xi' d\eta' d\zeta' \end{array} \right. \quad (\text{D.4c})$$

$V$  is the volume of the sample and  $\vec{x}$  and  $\vec{x}'$  are position vectors. The dipole field could be written with a clean form after integration,

$$\vec{h}_d(\xi) = \int_{-L/2}^{L/2} \hat{G}_{\xi\eta\zeta}(\xi, \xi') \vec{m}(\xi') d\xi' \quad (\text{D.5})$$

where the tensor of Green's function has the form

$$\hat{G}_{\xi\eta\zeta}(\xi, \xi') = \begin{bmatrix} G_P - \delta(\xi - \xi') & 0 & iG_Q \\ 0 & 0 & 0 \\ iG_Q & 0 & -G_P \end{bmatrix} \quad (\text{D.6})$$

With

$$G_P = \frac{k_\zeta}{2} e^{-k_\zeta |\xi - \xi'|} \quad (\text{D.7a})$$

$$G_Q = G_P \text{sgn}(\xi - \xi') \quad (\text{D.7b})$$

Here  $\delta$  is the Dirac delta function and  $\text{sgn}$  is the sign function. The subscripts indicate the representation form in the  $(\xi, \eta, \zeta)$  coordinate system. One important symmetric property of this Green function components is

$$G_P(\xi, \xi') = G_P(\xi', \xi) \quad (\text{D.8a})$$

$$G_Q(\xi, \xi') = -G_Q(\xi', \xi) \quad (\text{D.8b})$$

## E. The mathematical form of the internal field

Only the external field and demagnetization field from shape anisotropy are considered in calculating the internal field. Thus,

$$\vec{H}_i = \vec{H}_e + \vec{H}_{de} = H_i \hat{z} \quad (\text{E.1})$$

where the demagnetization field is

$$\vec{H}_{de} = -4\pi \begin{pmatrix} N_\xi & 0 & 0 \\ 0 & N_\eta & 0 \\ 0 & 0 & N_\zeta \end{pmatrix} \begin{pmatrix} M_0 \cos \theta \\ M_0 \sin \theta \\ 0 \end{pmatrix} \quad (\text{E.2})$$

For the configuration shown in Fig. 3.1,  $N_\xi=1$ ,  $N_\eta=N_\zeta=0$ . This leads to

$$\vec{H}_{de} = -4\pi M_0 \cos \theta \hat{\xi} \quad (\text{E.3})$$

The internal field is parallel to the saturation magnetization. This means

$$\vec{H}_i \times \vec{M}_0 = \vec{H}_e \times \vec{M}_0 - 4\pi M_0 \cos \theta \hat{\xi} \times \vec{M}_0 = 0 \quad (\text{E.4})$$

With some simple algebra, one can get

$$4\pi M_0 \sin 2\theta = 2H_e \sin(\theta - \theta_e) \quad (\text{E.5})$$

Equation 3.11c can be acquired by checking the  $\zeta$  component of the internal field, external field and demagnetization field. The amplitude of the internal field is

$$\begin{aligned} H_i &= \frac{\vec{H}_i \cdot \vec{M}_0}{|\vec{M}_0|} \\ &= (H_e \cos \theta_e - 4\pi M_0 \cos \theta) \cos \theta + H_e \sin \theta_e \sin \theta \\ &= H_e \cos(\theta - \theta_e) - 4\pi M_0 \cos^2 \theta \end{aligned} \quad (\text{E.6})$$

## F. Linearized precession equation

By inserting Eq. 3.10b into the LHS of Eq. 3.14, one can get

$$\frac{\partial \vec{m}(\xi, \zeta, t)}{\partial t} = i\omega \vec{m}(\xi) e^{i(\omega t - k_\zeta \zeta)} \quad (\text{F.1})$$

For the RHS of Eq. 3.14,

$$\begin{aligned} \nabla^2 \vec{m}(\vec{r}, t) &= \nabla^2 \vec{m}(\xi) e^{i(\omega t - k_\zeta \zeta)} \\ &= [\nabla^2 \vec{m}(\xi)] e^{i(\omega t - k_\zeta \zeta)} + \vec{m}(\xi) \nabla^2 e^{i(\omega t - k_\zeta \zeta)} \\ &= \left( \frac{\partial^2}{\partial \xi^2} - k_\zeta^2 \right) \vec{m}(\xi) e^{i(\omega t - k_\zeta \zeta)} \end{aligned} \quad (\text{F.2})$$

Insert Eq. F.1 and F.2 into Eq. 3.14 as well as the integral form of the dipole field, one can get

$$i\omega \vec{m}(\xi) e^{i(\omega t - k_\zeta \zeta)} = -|\gamma| \left\{ \begin{aligned} &H_i \vec{m}(\xi) e^{i(\omega t - k_\zeta \zeta)} - \\ &M_0 \int_{-L/2}^{L/2} \hat{G}_{xy}(\xi, \xi') \vec{m}(\xi') e^{i(\omega t - k_\zeta \zeta)} d\xi' - \\ &A_{ex} M_0 \left( \frac{\partial^2}{\partial \xi^2} - k_\zeta^2 \right) \vec{m}(\xi) e^{i(\omega t - k_\zeta \zeta)} \end{aligned} \right\} \times \hat{z} \quad (\text{F.3})$$

One thing should be noted that only the precessional components ( $x, y$  components) of the dynamic magnetic moments contribute to the equation and the tensor of the Green's function  $\hat{G}_{xy}$  describing the dipole field should be derived from 3-dimensional tensor into 2-dimensional tensor and from the  $(\xi, \eta, \zeta)$  coordinate system to the  $(x, y, z)$  system. The explicit form of  $\hat{G}_{xy}$  is derived in Appendix I. Dropping the exponential terms on both sides and multiplying with the unit vector of  $z$  direction leads to

$$i\omega\vec{m}(\xi) \times \hat{z} = |\gamma| \left\{ H_i \vec{m}(\xi) - M_0 \int_{-L/2}^{L/2} \hat{G}_{xy}(\xi, \xi') \vec{m}(\xi') d\xi' - A_{ex} M_0 \left( \frac{\partial^2}{\partial \xi^2} - k_\zeta^2 \right) \vec{m}(\xi) \right\} \quad (\text{F.4})$$

The LHS of Eq. F.4 can be simplified as

$$\begin{aligned} i\omega\vec{m}(\xi) \times \hat{z} &= i\omega \left( m^x(\xi) \hat{x} + m^y(\xi) \hat{y} \right) \times \hat{z} \\ &= i\omega \left( -m^x(\xi) \hat{y} + m^y(\xi) \hat{x} \right) \\ &= -i\omega \hat{T} \vec{m}(\xi) \end{aligned} \quad (\text{F.5})$$

where

$$\hat{T} = \begin{bmatrix} 0 & -1 \\ 1 & 0 \end{bmatrix}$$

and the superscripts indicate the vector components in the  $x$  and  $y$  directions. Define

$$\omega_H = |\gamma| H_i, \quad \omega_M = |\gamma| M_0 \quad (\text{F.6})$$

Eq. F4 can be simplified as

$$\left( -A_{ex} \frac{\partial^2}{\partial \xi^2} + A_{ex} k_\zeta^2 + \frac{\omega_H}{\omega_M} \right) \hat{I} \cdot \vec{m}(\xi) = -i \frac{\omega}{\omega_M} \hat{T} \vec{m}(\xi) + \int_{-L/2}^{L/2} \hat{G}_{xy}(\xi, \xi') \vec{m}(\xi') d\xi' \quad (\text{F.7})$$

and  $\hat{I}$  is the  $2 \times 2$  unit matrix.

## G. Solutions for the Sturm-Liouville problem

This section serves as a supplemental material to those who are interested in finding the solutions for the S-L problem. The S-L problem for  $x$  and  $y$  components are independent and similar except for a little difference in the boundary condition. By solving the problem of the  $x$  component and getting the solutions for  $x$  direction first, one can get the solutions of for  $y$  direction by simply replacing  $\cos 2\theta$  with  $\cos^2\theta$ . The problem is readdressed as

$$\begin{cases} \left( -A_{ex} \frac{d^2}{dx^2} + A_{ex} k_\zeta^2 + \frac{\omega_H}{\omega_M} \right) f(x) = Nf(x), & -L/2 \leq x \leq L/2 \\ \left( \frac{d}{dx} + d_1 \cos 2\theta \right) f(x) \Big|_{x=L/2} = 0 \\ \left( -\frac{d}{dx} + d_2 \cos 2\theta \right) f(x) \Big|_{x=-L/2} = 0 \end{cases} \quad (\text{G.1})$$

By solving the ordinary differential Eq. G.1, we can get

$$f_n(x) = A_{n1} \cos(\kappa_n x) + A_{n2} \sin(\kappa_n x) \quad (\text{G.2})$$

where

$$\kappa_n^2 = \frac{N}{A_{ex}} - \frac{\omega_H}{A_{ex} \omega_M} - k_\zeta^2$$

$A_{n1}$  and  $A_{n2}$  are coefficients determined by the boundary conditions. The subscript  $n$  marks the eigenfunction corresponding to the countable eigenvalue  $N$  in Eq. G.1. By inserting Eq. G.2a in the boundary conditions, one can get

$$\begin{cases} -\kappa_n A_{n1} \sin\left(\frac{\kappa_n L}{2}\right) + \kappa_n A_{n2} \cos\left(\frac{\kappa_n L}{2}\right) + d_1 \cos 2\theta \left[ A_{n1} \cos\left(\frac{\kappa_n L}{2}\right) + A_{n2} \sin\left(\frac{\kappa_n L}{2}\right) \right] = 0 \\ \kappa_n A_{n1} \sin\left(-\frac{\kappa_n L}{2}\right) - \kappa_n A_{n2} \cos\left(-\frac{\kappa_n L}{2}\right) + d_2 \cos 2\theta \left[ A_{n1} \cos\left(-\frac{\kappa_n L}{2}\right) + A_{n2} \sin\left(-\frac{\kappa_n L}{2}\right) \right] = 0 \end{cases}$$

Rearrange and one can get

$$\begin{cases} \left[ -\kappa_n \sin\left(\frac{\kappa_n L}{2}\right) + d_1 \cos 2\theta \cos\left(\frac{\kappa_n L}{2}\right) \right] A_{n1} + \left[ \kappa_n \cos\left(\frac{\kappa_n L}{2}\right) + d_1 \cos 2\theta \sin\left(\frac{\kappa_n L}{2}\right) \right] A_{n2} = 0 \\ \left[ -\kappa_n \sin\left(\frac{\kappa_n L}{2}\right) + d_2 \cos 2\theta \cos\left(\frac{\kappa_n L}{2}\right) \right] A_{n1} + \left[ -\kappa_n \cos\left(\frac{\kappa_n L}{2}\right) - d_2 \cos 2\theta \sin\left(\frac{\kappa_n L}{2}\right) \right] A_{n2} = 0 \end{cases}$$

Both equations are valid for arbitrary  $A_{n1}$  and  $A_{n2}$ . So

$$\det \begin{vmatrix} -\kappa_n \sin\left(\frac{\kappa_n L}{2}\right) + d_1 \cos 2\theta \cos\left(\frac{\kappa_n L}{2}\right) & \kappa_n \cos\left(\frac{\kappa_n L}{2}\right) + d_1 \cos 2\theta \sin\left(\frac{\kappa_n L}{2}\right) \\ -\kappa_n \sin\left(\frac{\kappa_n L}{2}\right) + d_2 \cos 2\theta \cos\left(\frac{\kappa_n L}{2}\right) & -\kappa_n \cos\left(\frac{\kappa_n L}{2}\right) - d_2 \cos 2\theta \sin\left(\frac{\kappa_n L}{2}\right) \end{vmatrix} = 0$$

After some simple and tedious algebra, one can get

$$\left[ (\kappa_n)^2 - d_1 d_2 \cos^2 2\theta \right] \tan(\kappa_n L) = \kappa_n (d_1 + d_2) \cos 2\theta \quad (\text{G.3})$$

and the eigenfunctions

$$f_n(x) = A_n \left\{ \cos \left[ \kappa_n \left( x + \frac{L}{2} \right) \right] + \frac{d_2 \cos 2\theta}{\kappa_n} \sin \left[ \kappa_n \left( x + \frac{L}{2} \right) \right] \right\} \quad (\text{G.4})$$

and the eigenvalues

$$N_n = \frac{\omega_H}{\omega_M} + A_{ex} (k_\zeta^2 + \kappa_n^2) \quad (\text{G.5})$$

## H. The amplitude of the eigenfunctions

This section serves as reference for interested readers on the derivation of the amplitude for the eigenfunctions Eq. 3.18b. By substituting Eq. 3.18 into the orthogonality condition Eq. 3.20, one can get

$$\begin{aligned}
& \int_{-L/2}^{L/2} \left[ A_n^p \left\{ \cos \left[ \kappa_n^p \left( \xi + \frac{L}{2} \right) \right] + \frac{d_2^p}{\kappa_n^p} \sin \left[ \kappa_n^p \left( \xi + \frac{L}{2} \right) \right] \right\} \right]^2 d\xi = L \\
(A_n^p)^2 \int_{-L/2}^{L/2} & \left\{ \cos^2 \left[ \kappa_n^p \left( \xi + \frac{L}{2} \right) \right] + \left( \frac{d_2^p}{\kappa_n^p} \right)^2 \sin^2 \left[ \kappa_n^p \left( \xi + \frac{L}{2} \right) \right] + \frac{2d_2^p}{\kappa_n^p} \sin \left[ \kappa_n^p \left( \xi + \frac{L}{2} \right) \right] \cos \left[ \kappa_n^p \left( \xi + \frac{L}{2} \right) \right] \right\} d\xi = L \\
(A_n^p)^2 \int_{-L/2}^{L/2} & \left\{ \frac{1 + \cos \left[ 2\kappa_n^p \left( \xi + \frac{L}{2} \right) \right]}{2} + \left( \frac{d_2^p}{\kappa_n^p} \right)^2 \frac{1 - \cos \left[ 2\kappa_n^p \left( \xi + \frac{L}{2} \right) \right]}{2} + \frac{d_2^p}{\kappa_n^p} \sin \left[ 2\kappa_n^p \left( \xi + \frac{L}{2} \right) \right] \right\} d\xi = L
\end{aligned}$$

After the integration, one can get the expression of the amplitude with the form

$$(A_n^p)^2 = 2 \left\{ \frac{(\kappa_n^p)^2 + (d_2^p)^2}{(\kappa_n^p)^2} + \frac{\sin(\kappa_n^p L)}{\kappa_n^p L} \left[ \frac{(\kappa_n^p)^2 - (d_2^p)^2}{(\kappa_n^p)^2} \cos(\kappa_n^p L) + \frac{2d_2^p}{\kappa_n^p} \sin(\kappa_n^p L) \right] \right\}^{-1} \quad (\text{H.1})$$

## I. Tensor of Green's functions for dipole fields in xy plane

Based on Fig. 3.1, one can write down the transformation matrix of the two sets of coordinate system

$$\hat{T}_t = \begin{pmatrix} \sin \theta & 0 & \cos \theta \\ -\cos \theta \sin \varphi & \cos \varphi & \sin \theta \sin \varphi \\ -\cos \theta \cos \varphi & -\sin \varphi & \sin \theta \cos \varphi \end{pmatrix} \quad (\text{I.1})$$

and the reverse transformation matrix

$$\hat{T}_t^{-1} = \begin{pmatrix} \sin \theta & -\cos \theta \sin \varphi & -\cos \theta \cos \varphi \\ 0 & \cos \varphi & -\sin \varphi \\ \cos \theta & \sin \theta \sin \varphi & \sin \theta \cos \varphi \end{pmatrix} \quad (\text{I.2})$$

The tensor in the  $(x, y, z)$  coordinate system has the form

$$\begin{aligned}
\hat{G}_{xyz}(\xi, \xi') &= \hat{T}_t^{-1} \hat{G}_{\xi\eta\zeta}(\xi, \xi') \hat{T}_t \\
&= \hat{T}_t^{-1} \begin{bmatrix} G_P - \delta(\xi - \xi') & 0 & iG_Q \\ 0 & 0 & 0 \\ iG_Q & 0 & -G_P \end{bmatrix} \hat{T}_t \\
&= \begin{bmatrix} a_{xx} & a_{xy} & a_{xz} \\ a_{yx} & a_{yy} & a_{yz} \\ a_{zx} & a_{zy} & a_{zz} \end{bmatrix}
\end{aligned}$$

By inserting Eq. I.1 and I.2, one can get

$$\begin{aligned}
a_{xx} &= -AG_P + \frac{B}{2}iG_Q - \delta(\xi - \xi')\sin^2\theta \\
a_{xy} &= a_{yx} = \frac{D}{2}iG_Q - CG_P \\
a_{yy} &= -EG_P
\end{aligned}$$

where

$$\begin{aligned}
A &= \cos^2\varphi - (1 + \cos^2\varphi)\sin^2\theta \\
B &= -2\cos\varphi\sin 2\theta \\
C &= \cos\theta\sin\varphi\cos\varphi \\
D &= -2\sin\theta\sin\varphi \\
E &= \sin^2\varphi
\end{aligned}$$

Then the explicit form of the tensor in the  $xy$  plane is

$$\hat{G}_{xy}(\xi, \xi') = \begin{bmatrix} -AG_P + \frac{B}{2}iG_Q - \delta(\xi - \xi')\sin^2\theta & \frac{D}{2}iG_Q - CG_P \\ \frac{D}{2}iG_Q - CG_P & -EG_P \end{bmatrix} \quad (\text{I.3})$$

## J. Simplification of the equation for spinwave amplitude

The equation for spin wave amplitude Eq. 3.24 is rewritten as

$$\begin{aligned}
& \sum_{n'} \left[ m_n^x N_n^x \begin{pmatrix} \Phi_n^x(\xi') \\ 0 \end{pmatrix} + m_n^y N_n^y \begin{pmatrix} 0 \\ \Phi_n^y(\xi') \end{pmatrix} \right] = -i \frac{\omega}{\omega_M} \sum_{n'} \left[ m_n^x \begin{pmatrix} 0 \\ \Phi_n^x(\xi) \end{pmatrix} - m_n^y \begin{pmatrix} \Phi_n^y(\xi') \\ 0 \end{pmatrix} \right] + \\
& \sum_{n'} \int_{-L/2}^{L/2} \left[ m_n^x \begin{pmatrix} -AG_P + \frac{B}{2} iG_Q \\ \frac{D}{2} iG_Q - CG_P \end{pmatrix} \Phi_n^x(\xi) + m_n^y \begin{pmatrix} \frac{D}{2} iG_Q - CG_P \\ -EG_P \end{pmatrix} \Phi_n^y(\xi) \right] d\xi - \sum_{n'} m_n^x \sin^2 \theta \begin{pmatrix} \Phi_n^x(\xi') \\ 0 \end{pmatrix} \quad (\text{J.1})
\end{aligned}$$

Multiplying Eq. J.1 by  $\bar{S}_n^x(\xi')^T = (\Phi_n^x(\xi'), 0)$  and integrating across the thickness, one can get

$$\begin{aligned}
& \sum_{n'} m_n^x N_n^x \frac{1}{L} \int_{-L/2}^{L/2} \Phi_n^x(\xi') \Phi_n^x(\xi) d\xi' = i \frac{\omega}{\omega_M} \sum_{n'} m_n^y \frac{1}{L} \int_{-L/2}^{L/2} \Phi_n^x(\xi') \Phi_n^y(\xi) d\xi' + \\
& \sum_{n'} \frac{1}{L} \int_{-L/2}^{L/2} \int_{-L/2}^{L/2} \left[ m_n^x \Phi_n^x(\xi') \Phi_n^x(\xi) \left( -AG_P + \frac{B}{2} iG_Q \right) + m_n^y \left( \frac{D}{2} iG_Q - CG_P \right) \Phi_n^x(\xi') \Phi_n^y(\xi) \right] d\xi d\xi' - (\text{J.2}) \\
& \sum_{n'} m_n^x \sin^2 \theta \frac{1}{L} \int_{-L/2}^{L/2} \Phi_n^x(\xi') \Phi_n^x(\xi) d\xi'
\end{aligned}$$

For convenience, define

$$\begin{aligned}
P_{nn'}^{pp'}(k_\zeta) &= P_{n'n}^{p'p}(k_\zeta) \equiv \frac{1}{L} \int_{-L/2}^{L/2} \int_{-L/2}^{L/2} G_P(\xi, \xi', k_\zeta) \Phi_n^p(\xi) \Phi_{n'}^{p'}(\xi') d\xi d\xi' \\
Q_{nn'}^{pp'}(k_\zeta) &= -Q_{n'n}^{p'p}(k_\zeta) \equiv \frac{1}{2L} \int_{-L/2}^{L/2} \int_{-L/2}^{L/2} G_Q(\xi, \xi', k_\zeta) \Phi_n^p(\xi) \Phi_{n'}^{p'}(\xi') d\xi d\xi' \\
T_{nn'}^{pp'} &= T_{n'n}^{p'p} \equiv \frac{1}{L} \int_{-L/2}^{L/2} \Phi_n^p(\xi) \Phi_{n'}^{p'}(\xi') d\xi
\end{aligned}$$

It is easy to verify that

$$T_{nn'}^{xx'} = T_{n'n}^{yy'} = 0 \text{ for } n \neq n' \quad T_{nn}^{xx} = T_{nn}^{yy} = 1 \quad \text{and} \quad Q_{nn}^{xx} = Q_{nn}^{yy} = 0$$

By inserting these into Eq. J.2, one can get

$$\begin{aligned} & \left[ \begin{array}{cc} N_n^x + \sin^2 \theta + AP_{nn}^{xx} & CP_{nn}^{xy} - i \left( \frac{\omega}{\omega_M} T_{nn}^{xy} - DQ_{nn}^{xy} \right) \\ 0 & 0 \end{array} \right] \begin{pmatrix} m_n^x \\ m_n^y \end{pmatrix} + \\ & \sum_{n' \neq n} \left[ \begin{array}{cc} AP_{nn'}^{xx} + iBQ_{nn'}^{xx} & CP_{nn'}^{xy} - i \left( \frac{\omega}{\omega_M} T_{nn'}^{xy} - DQ_{nn'}^{xy} \right) \\ 0 & 0 \end{array} \right] \begin{pmatrix} m_{n'}^x \\ m_{n'}^y \end{pmatrix} = 0 \end{aligned} \quad (\text{J.3})$$

Multiply Eq. J.1 by  $\bar{S}_n^y(\xi')^T = (0, \Phi_n^y(\xi'))$  and integrating across the thickness, one can get

$$\begin{aligned} & \sum_{n'} m_{n'}^y N_{n'}^y \frac{1}{L} \int_{-L/2}^{L/2} \Phi_n^y(\xi') \Phi_{n'}^y(\xi') d\xi' = -i \frac{\omega}{\omega_M} \sum_{n'} m_{n'}^x \frac{1}{L} \int_{-L/2}^{L/2} \Phi_n^y(\xi') \Phi_{n'}^x(\xi') d\xi' + \\ & \sum_{n'} \frac{1}{L} \int_{-L/2}^{L/2} \int_{-L/2}^{L/2} \left[ m_{n'}^x \Phi_{n'}^x(\xi) \Phi_n^y(\xi') \left( \frac{D}{2} iG_Q - CG_P \right) - m_{n'}^y \Phi_{n'}^y(\xi) \Phi_n^y(\xi') \right] d\xi d\xi' \end{aligned}$$

This leads to, after some calculation,

$$\left[ \begin{array}{cc} 0 & 0 \\ CP_{nn}^{yx} + i \left( \frac{\omega}{\omega_M} T_{nn}^{yx} + DQ_{nn}^{yx} \right) & N_n^y + EP_{nn}^{yy} \end{array} \right] \begin{pmatrix} m_n^x \\ m_n^y \end{pmatrix} + \sum_{n' \neq n} \left[ \begin{array}{cc} 0 & 0 \\ CP_{nn'}^{yx} + i \left( \frac{\omega}{\omega_M} T_{nn'}^{yx} + DQ_{nn'}^{yx} \right) & EP_{nn'}^{yy} \end{array} \right] \begin{pmatrix} m_{n'}^x \\ m_{n'}^y \end{pmatrix} = 0 \quad (\text{J.4})$$

Combine Eq. J.3 and J.4 into a matrix form and one can get

$$\hat{D}_{nn} \bar{m}_n + \sum_{n' \neq n} \hat{R}_{nn'} \bar{m}_{n'} = 0 \quad (\text{J.5})$$

where

$$\bar{m}_n = \begin{pmatrix} m_n^x \\ m_n^y \end{pmatrix}$$

$$\hat{D}_{nn} = \left[ \begin{array}{cc} N_n^x + \sin^2 \theta + AP_{nn}^{xx} & CP_{nn}^{xy} - i \left( \frac{\omega}{\omega_M} T_{nn}^{xy} - DQ_{nn}^{xy} \right) \\ CP_{nn}^{yx} + i \left( \frac{\omega}{\omega_M} T_{nn}^{yx} + DQ_{nn}^{yx} \right) & N_n^y + EP_{nn}^{yy} \end{array} \right]$$

$$\hat{R}_{m'} = \begin{bmatrix} AP_{m'}^{xx} + iBQ_{m'}^{xx} & CP_{m'}^{xy} - i\left(\frac{\omega}{\omega_M} T_{m'}^{xy} - DQ_{m'}^{xy}\right) \\ CP_{m'}^{yx} + i\left(\frac{\omega}{\omega_M} T_{m'}^{yx} + DQ_{m'}^{yx}\right) & EP_{m'}^{yy} \end{bmatrix}$$

$$P_{m'}^{pp'}(k_\zeta) = P_{n'n}^{p'p}(k_\zeta) = \frac{1}{L} \int_{-L/2}^{L/2} \int_{-L/2}^{L/2} G_P(\xi, \xi', k_\zeta) \Phi_n^p(\xi) \Phi_{n'}^{p'}(\xi') d\xi d\xi'$$

$$Q_{m'}^{pp'}(k_\zeta) = -Q_{n'n}^{p'p}(k_\zeta) = \frac{1}{2L} \int_{-L/2}^{L/2} \int_{-L/2}^{L/2} G_Q(\xi, \xi', k_\zeta) \Phi_n^p(\xi) \Phi_{n'}^{p'}(\xi') d\xi d\xi'$$

$$T_{m'}^{pp'} = T_{n'n}^{p'p} = \frac{1}{L} \int_{-L/2}^{L/2} \Phi_n^p(\xi) \Phi_{n'}^{p'}(\xi') d\xi$$

$$A = \cos^2 \varphi - (1 + \cos^2 \varphi) \sin^2 \theta$$

$$B = -2 \cos \varphi \sin 2\theta$$

$$C = \cos \theta \sin \varphi \cos \varphi$$

$$D = -2 \sin \theta \sin \varphi$$

$$E = \sin^2 \varphi$$

## K. Explicit analytical form of operators $P$ and $Q$

This section serves as detailed derivation of the explicit analytical form of operators  $P_{m'}^{pp'}$  and  $Q_{m'}^{pp'}$  in some special cases.

By substituting Eq. 3.7c and Eq. 3.7d in Eq. 3.26b and Eq. 3.26c, one can get

$$P_{m'}^{pp'}(k_\zeta) = P_{n'n}^{p'p}(k_\zeta) = J_1 + J_2$$

$$Q_{m'}^{pp'}(k_\zeta) = -Q_{n'n}^{p'p}(k_\zeta) = \frac{(J_1 - J_2)}{2}$$

where

$$J_1 = \frac{k_\zeta}{2L} \int_{-L/2}^{L/2} \Phi_n^p(\xi) e^{-k_\zeta \xi} d\xi \int_{-L/2}^{\xi} \Phi_{n'}^{p'}(\xi') e^{k_\zeta \xi'} d\xi'$$

$$J_2 = \frac{k_\zeta}{2L} \int_{-L/2}^{L/2} \Phi_n^p(\xi) e^{k_\zeta \xi} d\xi \int_{\xi}^{L/2} \Phi_{n'}^{p'}(\xi') e^{-k_\zeta \xi'} d\xi'$$

By substituting Eq. 3.18b in the second integral of the expressions for  $J_1$ , one can get

$$\begin{aligned}
J_1 &= \frac{k_\zeta}{2L} \int_{-L/2}^{L/2} \Phi_n^p(\xi) e^{-k_\zeta \xi} d\xi \int_{-L/2}^{\xi} e^{k_\zeta \xi'} A_{n'}^{p'} \left\{ \cos \left[ \kappa_{n'}^{p'} \left( \xi' + \frac{L}{2} \right) \right] + \frac{d_2^{p'}}{\kappa_{n'}^{p'}} \sin \left[ \kappa_{n'}^{p'} \left( \xi' + \frac{L}{2} \right) \right] \right\} d\xi' \\
&= \frac{k_\zeta A_{n'}^{p'}}{2L} \int_{-L/2}^{L/2} \Phi_n^p(\xi) e^{-k_\zeta \xi} d\xi \left\{ \int_{-L/2}^{\xi} e^{k_\zeta \xi'} \cos \left[ \kappa_{n'}^{p'} \left( \xi' + \frac{L}{2} \right) \right] d\xi' + \frac{d_2^{p'}}{\kappa_{n'}^{p'}} \int_{-L/2}^{\xi} e^{k_\zeta \xi'} \sin \left[ \kappa_{n'}^{p'} \left( \xi' + \frac{L}{2} \right) \right] d\xi' \right\}
\end{aligned}$$

With the help of the following two integral formulas,

$$I_1 = \int e^{ax} \cos(bx) dx = \frac{e^{ax}}{a^2 + b^2} [a \cos(bx) + b \sin(bx)]$$

$$I_2 = \int e^{ax} \sin(bx) dx = \frac{e^{ax}}{a^2 + b^2} [a \sin(bx) - b \cos(bx)]$$

one can get

$$\begin{aligned}
J_1 &= \frac{k_\zeta A_{n'}^{p'}}{2L} \int_{-L/2}^{L/2} \Phi_n^p(\xi) e^{-k_\zeta \xi} d\xi \times \left\{ \left. \begin{aligned} &\frac{e^{k_\zeta \xi'}}{k_\zeta^2 + (\kappa_{n'}^{p'})^2} \left[ \kappa_{n'}^{p'} \sin \kappa_{n'}^{p'} \left( \xi' + \frac{L}{2} \right) + k_\zeta \cos \kappa_{n'}^{p'} \left( \xi' + \frac{L}{2} \right) \right] + \\ &\frac{d_2^{p'}}{\kappa_{n'}^{p'}} \frac{e^{k_\zeta \xi'}}{k_\zeta^2 + (\kappa_{n'}^{p'})^2} \left[ k_\zeta \sin \kappa_{n'}^{p'} \left( \xi' + \frac{L}{2} \right) - \kappa_{n'}^{p'} \cos \kappa_{n'}^{p'} \left( \xi' + \frac{L}{2} \right) \right] \end{aligned} \right\} \Bigg|_{\xi' = -L/2}^{\xi' = \xi} \\
&= \frac{k_\zeta A_{n'}^{p'}}{2L (\kappa_{n'}^{p'})^2} \left\{ \begin{aligned} &(d_2^{p'} - k_\zeta) \int_{-L/2}^{L/2} \Phi_n^p(\xi) e^{-k_\zeta (\xi + L/2)} d\xi - (d_2^{p'} - k_\zeta) \int_{-L/2}^{L/2} \Phi_n^p(\xi) \cos \kappa_{n'}^{p'} \left( \xi + \frac{L}{2} \right) d\xi \\ &+ \frac{(\kappa_{n'}^{p'})^2 + d_2^{p'} k_\zeta}{\kappa_{n'}^{p'}} \int_{-L/2}^{L/2} \Phi_n^p(\xi) \sin \kappa_{n'}^{p'} \left( \xi + \frac{L}{2} \right) d\xi \end{aligned} \right\}
\end{aligned}$$

With a similar method applied on  $J_2$ , one can get

$$J_2 = \frac{k_\zeta A_{n'}^{p'}}{2L (\kappa_{n'}^{p'})^2} \left\{ \begin{aligned} &\left[ \frac{(\kappa_{n'}^{p'})^2 - d_2^{p'} k_\zeta}{\kappa_{n'}^{p'}} \sin \kappa_{n'}^{p'} L - (k_\zeta + d_2^{p'}) \cos \kappa_{n'}^{p'} L \right] e^{-k_\zeta L} \int_{-L/2}^{L/2} \Phi_n^p(\xi) e^{k_\zeta (\xi + L/2)} d\xi \\ &+ (k_\zeta + d_2^{p'}) \int_{-L/2}^{L/2} \Phi_n^p(\xi) \cos \kappa_{n'}^{p'} \left( \xi + \frac{L}{2} \right) d\xi - \frac{(\kappa_{n'}^{p'})^2 - d_2^{p'} k_\zeta}{\kappa_{n'}^{p'}} \int_{-L/2}^{L/2} \Phi_n^p(\xi) \sin \kappa_{n'}^{p'} \left( \xi + \frac{L}{2} \right) d\xi \end{aligned} \right\}$$

By repeating the substitution and calculation, one can get the explicit form as

$$J_1 = \frac{k_\zeta A_n^{p'} A_n^p}{2L(k_n^{p'})^2} \left\{ \begin{aligned} & \left[ \frac{(d_2^{p'} - k_\zeta)}{(k_n^p)^2} \left[ e^{-k_\zeta L} \frac{(\kappa_n^p)^2 - d_2^p k_\zeta}{\kappa_n^p} \sin \kappa_n^p L + (d_2^p + k_\zeta) (1 - e^{-k_\zeta L} \cos \kappa_n^p L) \right] - \right. \\ & \left. \frac{(d_2^{p'} - k_\zeta)}{2} \left[ \frac{\sin(\kappa_n^p + \kappa_n^{p'}) L}{\kappa_n^p + \kappa_n^{p'}} + \frac{\sin(\kappa_n^p - \kappa_n^{p'}) L}{\kappa_n^p - \kappa_n^{p'}} - \frac{d_2^p}{\kappa_n^p} \left( \frac{\cos(\kappa_n^p + \kappa_n^{p'}) L - 1}{\kappa_n^p + \kappa_n^{p'}} + \frac{\cos(\kappa_n^p - \kappa_n^{p'}) L - 1}{\kappa_n^p - \kappa_n^{p'}} \right) \right] + \right. \\ & \left. \frac{(\kappa_n^{p'})^2 + d_2^{p'} k_\zeta}{2\kappa_n^{p'}} \left[ \frac{1 - \cos(\kappa_n^p + \kappa_n^{p'}) L}{\kappa_n^p + \kappa_n^{p'}} + \frac{\cos(\kappa_n^p - \kappa_n^{p'}) L - 1}{\kappa_n^p - \kappa_n^{p'}} + \frac{d_2^p}{\kappa_n^p} \left( \frac{\sin(\kappa_n^p - \kappa_n^{p'}) L}{\kappa_n^p - \kappa_n^{p'}} - \frac{\sin(\kappa_n^p + \kappa_n^{p'}) L}{\kappa_n^p + \kappa_n^{p'}} \right) \right] \right\} \\ \\ J_2 = \frac{k_\zeta A_n^{p'} A_n^p}{2L(k_n^{p'})^2} \left\{ \begin{aligned} & \left[ \frac{(\kappa_n^{p'})^2 - d_2^{p'} k_\zeta}{\kappa_n^{p'}} \sin \kappa_n^{p'} L - (k_\zeta + d_2^{p'}) \cos \kappa_n^{p'} L \right] \times \\ & \frac{e^{-k_\zeta L}}{(k_n^p)^2} \left[ e^{k_\zeta L} \frac{(\kappa_n^p)^2 + d_2^p k_\zeta}{\kappa_n^p} \sin \kappa_n^p L + (d_2^p - k_\zeta) (1 - e^{k_\zeta L} \cos \kappa_n^p L) \right] - \\ & \frac{(d_2^{p'} + k_\zeta)}{2} \left[ \frac{\sin(\kappa_n^p + \kappa_n^{p'}) L}{\kappa_n^p + \kappa_n^{p'}} + \frac{\sin(\kappa_n^p - \kappa_n^{p'}) L}{\kappa_n^p - \kappa_n^{p'}} - \frac{d_2^p}{\kappa_n^p} \left( \frac{\cos(\kappa_n^p + \kappa_n^{p'}) L - 1}{\kappa_n^p + \kappa_n^{p'}} + \frac{\cos(\kappa_n^p - \kappa_n^{p'}) L - 1}{\kappa_n^p - \kappa_n^{p'}} \right) \right] - \\ & \left. \frac{(\kappa_n^{p'})^2 - d_2^{p'} k_\zeta}{2\kappa_n^{p'}} \left[ \frac{1 - \cos(\kappa_n^p + \kappa_n^{p'}) L}{\kappa_n^p + \kappa_n^{p'}} + \frac{\cos(\kappa_n^p - \kappa_n^{p'}) L - 1}{\kappa_n^p - \kappa_n^{p'}} + \frac{d_2^p}{\kappa_n^p} \left( \frac{\sin(\kappa_n^p - \kappa_n^{p'}) L}{\kappa_n^p - \kappa_n^{p'}} - \frac{\sin(\kappa_n^p + \kappa_n^{p'}) L}{\kappa_n^p + \kappa_n^{p'}} \right) \right] \right\} \end{aligned} \right.$$

which finalized the task of this section.

Two special cases are discussed below for interested readers. The first case is when both components of the transverse magnetization are pinned uniformly ( $d_1^x = d_1^y \equiv d_1$ ,  $d_2^x = d_2^y \equiv d_2$ ) but different on the top and bottom sides. In this case the explicit forms of P and Q are

$$P_{m'} = \frac{k_\zeta^2}{k_n^2} \delta_{m'} + \frac{k_\zeta A_n A_n'}{2L k_n^2 k_n'} \left\{ \begin{aligned} & \left( k_\zeta^2 - d_2^2 \right) e^{-k_\zeta L} (\cos \kappa_n L + \cos \kappa_n' L) - (k_\zeta^2 - d_2^2) (1 + \cos \kappa_n L \cos \kappa_n' L) + \\ & (k_\zeta - d_2) e^{-k_\zeta L} \left[ (d_2 k_\zeta - \kappa_n^2) \frac{\sin \kappa_n L}{\kappa_n L} + (d_2 k_\zeta - \kappa_n'^2) \frac{\sin \kappa_n' L}{\kappa_n' L} \right] + \\ & \left( \kappa_n^2 \kappa_n'^2 - d_2^2 k_\zeta^2 \right) \frac{\sin \kappa_n L}{\kappa_n L} \frac{\sin \kappa_n' L}{\kappa_n' L} - d_2 k_n^2 \cos \kappa_n' L \frac{\sin \kappa_n L}{\kappa_n L} + d_2 k_n'^2 \cos \kappa_n L \frac{\sin \kappa_n' L}{\kappa_n' L} \end{aligned} \right.$$

$$Q_{m'} = \frac{k_\zeta A_n A_{n'}}{4Lk_n^2 k_{n'}^2} \left\{ \begin{aligned} & \left( k_\zeta^2 - d_2^2 \right) e^{-k_\zeta L} (\cos \kappa_n L - \cos \kappa_{n'} L) + (k_\zeta - d_2) e^{-k_\zeta L} \left[ (d_2 k_\zeta - \kappa_n^2) \frac{\sin \kappa_n L}{\kappa_n L} - (d_2 k_\zeta - \kappa_{n'}^2) \frac{\sin \kappa_{n'} L}{\kappa_{n'} L} \right] \\ & + (k_\zeta - d_2) \left[ (d_2 k_\zeta - \kappa_{n'}^2) \cos \kappa_n L \frac{\sin \kappa_{n'} L}{\kappa_{n'} L} - (d_2 k_\zeta - \kappa_n^2) \cos \kappa_{n'} L \frac{\sin \kappa_n L}{\kappa_n L} \right] + \\ & (1 - \cos \kappa_n L \cos \kappa_{n'} L) \frac{2(k_\zeta^2 d_2^2 + \kappa_n^2 \kappa_{n'}^2) + (\kappa_{n'}^2 + \kappa_n^2)(k_\zeta^2 + d_2^2)}{\kappa_{n'}^2 - \kappa_n^2} - \\ & \frac{\sin \kappa_n L \sin \kappa_{n'} L}{\kappa_n \kappa_{n'} (\kappa_{n'}^2 - \kappa_n^2)} \left[ d_2 k_\zeta (\kappa_{n'}^4 + \kappa_n^4) + (d_2^2 k_\zeta^2 + \kappa_n^2 \kappa_{n'}^2) (\kappa_{n'}^2 + \kappa_n^2) + 2\kappa_n^2 \kappa_{n'}^2 (d_2^2 + k_\zeta^2 - d_2 k_\zeta) \right] \end{aligned} \right\}$$

With  $Q_{mn} = 0$ ,  $T_{mn} = 1$  for uniformly pinned case, the dispersion relations Eq. 3.28 can be simplified as

$$\omega_n^2 = (\omega_H + A_{ex} \omega_M k_n^2) (\omega_H + A_{ex} \omega_M k_n^2 + \omega_M F_m)$$

where

$$F_m = P_m + \sin^2 \theta \left[ 1 - P_m (1 + \cos^2 \varphi) + \omega_M \frac{P_m (1 - P_m) \sin^2 \varphi}{\omega_H + A_{ex} \omega_M k_n^2} \right]$$

The second case is when the two surfaces are totally pinned ( $d_1 = d_2 \rightarrow \infty$ ) or unpinned ( $d_1 = d_2 \rightarrow 0$ ). For the pinned surface, the dynamic component of magnetization is fixed and cannot rotate. This indicates  $d_1 = d_2 \rightarrow \infty$  and leads to

$$\begin{aligned} \kappa_n &\rightarrow \frac{n\pi}{L}, n = 1, 2, 3, \dots \\ A_n &\rightarrow \frac{\sqrt{2} \kappa_n}{d_2} \\ P_{m'} &\rightarrow \frac{k_\zeta^2}{k_{n'}^2} \delta_{m'} + \left( \frac{1 + (-1)^{n+n'}}{2} \right) \frac{k_\zeta^2}{k_n^2} \frac{\kappa_n \kappa_{n'}}{k_n^2} F_n \\ Q_{m'} &\rightarrow \frac{k_\zeta^2}{k_{n'}^2} \left( \frac{1 - (-1)^{n+n'}}{2} \right) \left( \frac{\kappa_n \kappa_{n'}}{\kappa_{n'}^2 - \kappa_n^2} \frac{2}{k_\zeta L} + \frac{\kappa_n \kappa_{n'}}{2k_n^2} F_n \right) \\ F_n &= \frac{2}{k_\zeta L} \left[ 1 - (-1)^n e^{-k_\zeta L} \right] \end{aligned}$$

For totally unpinned surface, the dynamic component of magnetization can rotate freely, which means  $d_1 = d_2 \rightarrow 0$  and leads to

$$\begin{aligned}
\kappa_n &\rightarrow \frac{n\pi}{L}, n = 0,1,2,\dots \\
A_n &\rightarrow \frac{2}{1 + \delta_{0n}} \\
P_{nn'} &\rightarrow \frac{k_\zeta^2}{k_{n'}^2} \delta_{nn'} - \left( \frac{1 + (-1)^{n+n'}}{2} \right) \left( \frac{1}{\sqrt{(1 + \delta_{0n})(1 + \delta_{0n'})}} \right) \frac{k_\zeta^4}{k_n^2 k_{n'}^2} F_n \\
Q_{nn'} &\rightarrow \frac{k_\zeta^2}{k_{n'}^2} \left( \frac{1 - (-1)^{n+n'}}{2} \right) \left( \frac{\kappa_{n'}^2}{\kappa_{n'}^2 - \kappa_n^2} \frac{2}{k_\zeta L} - \frac{k_\zeta^2}{2k_n^2} F_n \right) \left( \frac{1}{\sqrt{(1 + \delta_{0n})(1 + \delta_{0n'})}} \right) \\
F_n &= \frac{2}{k_\zeta L} \left[ 1 - (-1)^n e^{-k_\zeta L} \right]
\end{aligned}$$

Further, for long wave approximation ( $k_\zeta L \ll 1$ ) and totally pinned or unpinned surfaces,

$P_{nn}$  has a simple form as

$$\left. \begin{aligned}
P_{nn} &\approx \frac{3(k_\zeta L)^2}{n^2 \pi^2} \quad n = 2,4,6,\dots \\
P_{nn} &\approx \frac{4k_\zeta L}{n^2 \pi^2} \quad n = 1,3,5,\dots
\end{aligned} \right\} \text{pinned}$$

$$\left. \begin{aligned}
P_{00} &\approx \frac{k_\zeta L}{2} \\
P_{nn} &\approx \left( \frac{k_\zeta L}{n\pi} \right)^2 \quad n = 1,2,3,\dots
\end{aligned} \right\} \text{unpinned}$$